Measurement and modeling of cloud condensation nuclei in continental air

Dissertation
zur Erlangung des Grades
"Doktor der Naturwissenschaften"

am Fachbereich Physik
der Johannes Gutenberg–Universität
in Mainz

Diana Rose

geboren in
Markranstädt

Mainz, 2010

1. Berichterstatter:

2. Berichterstatter:

Tag der mündlichen Prüfung: 14. September 2010

"A little gale will soon disperse that cloud
And blow it to the source from whence it came.
Thy very beams will dry those vapours up,
For every cloud engenders not a storm."

William Shakespeare, King Henry VI, Part 3, 1591

Abstract

Atmospheric aerosol particles serving as cloud condensation nuclei (CCN) are key elements of the hydrological cycle and climate. Knowledge of the spatial and temporal distribution of CCN in the atmosphere is essential to understand and describe the effects of aerosols in meteorological models. In this study, CCN properties were measured in polluted and pristine air of different continental regions, and the results were parameterized for efficient prediction of CCN concentrations.

The continuous-flow CCN counter used for size-resolved measurements of CCN efficiency spectra (activation curves) was calibrated with ammonium sulfate and sodium chloride aerosols for a wide range of water vapor supersaturations (S=0.068% to 1.27%). A comprehensive uncertainty analysis showed that the instrument calibration depends strongly on the applied particle generation techniques, Köhler model calculations, and water activity parameterizations (relative deviations in S up to 25%). Laboratory experiments and a comparison with other CCN instruments confirmed the high accuracy and precision of the calibration and measurement procedures developed and applied in this study.

The mean CCN number concentrations ($N_{\mathrm{CCN,S}}$) observed in polluted mega-city air and biomass burning smoke (Beijing and Pearl River Delta, China) ranged from $1000\,\mathrm{cm}^{-3}$ at S=0.068% to $16\,000\,\mathrm{cm}^{-3}$ at S=1.27%, which is about two orders of magnitude higher than in pristine air at remote continental sites (Swiss Alps, Amazonian rainforest).

Effective average hygroscopicity parameters, κ, describing the influence of chemical composition on the CCN activity of aerosol particles were derived from the measurement data. They varied in the range of 0.3±0.2, were size-dependent, and could be parameterized as a function of organic and inorganic aerosol mass fraction. At low S ($\leq$0.27%), substantial portions of externally mixed CCN-inactive particles with much lower hygroscopicity were observed in polluted air (fresh soot particles with $\kappa\approx$0.01). Thus, the aerosol particle mixing state needs to be known for highly accurate predictions of $N_{\mathrm{CCN,S}}$.

Nevertheless, the observed CCN number concentrations could be efficiently approximated using measured aerosol particle number size distributions and a simple κ-Köhler model with a single proxy for the effective average particle hygroscopicity. The relative deviations between observations and model predictions were on average less than 20% when a constant average value of κ=0.3 was used in conjunction with variable size distribution data. With a constant average size distribution, however, the deviations increased up to 100% and more. The measurement and model results demonstrate that the aerosol particle number and size are the major predictors for the variability of the CCN concentration in continental boundary layer air, followed by particle composition and hygroscopicity as relatively minor modulators.

Depending on the required and applicable level of detail, the measurement results and parameterizations presented in this study can be directly implemented in detailed process models as well as in large-scale atmospheric and climate models for efficient description of the CCN activity of atmospheric aerosols.

Zusammenfassung

Atmosphärische Aerosolpartikel, die als Wolkenkondensationskerne (CCN) dienen, sind von zentraler Bedeutung für den Wasserkreislauf und das Klima. Um die Effekte von Aerosolen in meteorologischen Modellen zu erfassen, sind Kenntnisse der räumlichen und zeitlichen Verteilung von CCN erforderlich. Im Rahmen dieser Studie wurden die CCN-Eigenschaften von verschmutzter und reiner Luft in verschiedenen kontinentalen Regionen untersucht. Die Messergebnisse wurden parametrisiert um eine einfache Vorhersage von CCN-Konzentrationen zu ermöglichen.

Für die größenaufgelösten Messungen von CCN-Effizienzspektren (Aktivierungskurven) wurde ein CCN-Zähler mit kontinuierlichem Durchfluss benutzt und mittels Ammoniumsulfat- und Natriumchloridaerosolen für einen weiten Wasserdampfübersättigungsbereich kalibriert (S=0.068% bis 1.27%). Eine umfassende Analyse der Messunsicherheiten zeigte, dass die Kalibrierergebnisse stark von der Methode der Partikelerzeugung sowie von den benutzten Köhlermodellen und Wasseraktivitätsparametrisierungen abhängen (relative Abweichungen in S bis zu 25%). Labormessungen und Vergleichsmessungen mit anderen CCN-Instrumenten bestätigten die hohe Genauigkeit der in dieser Studie entwickelten und angewandten Kalibrier- und Messmethoden.

Die CCN-Anzahlkonzentrationen in den verschmutzten Ballungsräumen (Peking und Perlflussdelta, China) reichten von $1000\,\mathrm{cm}^{-3}$ bei S=0.068% bis $16\,000\,\mathrm{cm}^{-3}$ bei S=1.27%. Diese Konzentrationen sind um etwa zwei Größenordnungen höher als in reiner Luft abgelegener kontinentaler Gebiete (Schweizer Alpen, Amazonas-Regenwald).

Aus den Messdaten konnten effektive Hygroskopizitätsparameter κ abgeleitet werden, die den Einfluss der chemischen Zusammensetzung auf die CCN-Aktivität der Partikel beschreiben. Diese Werte lagen im Mittel bei 0.3 ± 0.2 und konnten als Funktion der organischen und anorganischen Massenfraktion dargestellt werden.

In verschmutzter Luft wurde bei geringen Übersättigungen ($\leq$0.27%) ein erheblicher Anteil an extern gemischten CCN-inaktiven Partikeln mit viel geringerer Hygroskopizität beobachtet (frische Rußpartikel mit $\kappa\approx$0.01). Für sehr genaue Vorhersagen von $N_{\mathrm{CCN,S}}$ muss daher auch der Mischungszustand bekannt sein. Dennoch konnten die beobachteten CCN-Konzentrationen auch unter Verwendung der gemessenen Partikelgrößenverteilungen und eines einfachen κ-Köhlermodells, das die effektive mittlere Hygroskopizität mit einem einzelnen Parameter beschreibt, gut angenähert werden. Wenn ein konstanter Mittelwert von κ=0.3 in Verbindung mit variablen Größenverteilungen benutzt wurde, lagen die Unterschiede zwischen gemessen und modellierten Werten im Mittel unter 20%. Wurde dagegen eine konstante Größenverteilung angenommen, stiegen die Unterschiede auf 100% und mehr. Die Mess- und Modellergebnisse zeigen, dass die Aerosolpartikelanzahl und -größe den stärksten Einfluss auf die Variabilität der CCN-Konzentrationen in der kontinentalen Grenzschicht haben, während die Partikelzusammensetzung und Hygroskopizität eher eine untergeordnete Rolle spielen.

Die Ergebnisse und Parametrisierungen dieser Doktorarbeit können zur Beschreibung der CCN-Aktivität atmosphärischer Aerosole direkt in detaillierten Prozessmodellen sowie in großräumigen Atmosphären- und Klimamodellen eingesetzt werden.

Contents

1 Introduction

1.1 Motivation

Atmospheric aerosol particles serving as cloud condensation nuclei (CCN) play an important role in the formation of clouds and precipitation, and influence atmospheric chemistry and physics, the hydrological cycle and climate (Pruppacher and Klett, 1997; Seinfeld and Pandis, 2006; Lohmann and Feichter, 2005). The response of cloud characteristics and precipitation processes to increasing anthropogenic aerosol concentrations represents one of the largest uncertainties in the current understanding of climate change. One of the crucial challenges is to determine the ability of aerosol particles to act as CCN under relevant atmospheric conditions, an issue that has received increasing attention over the past years (McFiggans et al., 2006; IAPSAG, 2007; IPCC, 2007; Andreae and Rosenfeld, 2008; Pöschl et al., 2009, and references therein).

Substantial progress has been made in recent years in understanding the source processes that produce cloud-active aerosols, the properties that enable aerosols to act as CCN, the effects of aerosols on cloud physics and precipitation, and the consequences for the climate system (Andreae and Rosenfeld, 2008). In order to incorporate the effects of CCN in meteorological models at all scales, from large eddy simulation (LES) to global climate models (GCM), knowledge of the spatial and temporal distribution of CCN in the atmosphere is essential (Huang et al., 2007). Several studies reported CCN measurements from various regions around the world (e.g., Andreae, 2009; Andreae and Rosenfeld, 2008; Bougiatioti et al., 2009; Broekhuizen et al., 2006; Chang et al., 2010; Dusek et al., 2006, 2010; Ervens et al., 2010; Gunthe et al., 2009; Lance et al., 2009; Pöschl et al., 2009; Roberts et al., 2001, 2002, 2006; Shantz et al., 2010; Wang et al., 2008, and references therein). However, the actual influence and relative importance of aerosol size distribution, chemical composition, and mixing state on the variability and predictability of CCN concentrations remained a subject of continued discussion. Size-resolved measurements, long-term data sets, and uncertainty analyses of CCN modeling techniques are needed to resolve these issues.

1.2 Impact of aerosols on clouds and climate

Aerosol particles influence the Earth's climate directly by scattering and absorption of solar radiation and indirectly through their role as cloud condensation nuclei (CCN) and ice nuclei (IN) by determining cloud microphysics, the formation of precipitation and cloud radiative properties (cloud albedo). As shown in Fig. 1.1, the radiative forcing by anthropogenic aerosols is assumed to be negative and cools the Earth's surface. Compared to other large forcing terms like those of long-lived greenhouse gases, however, the magnitude of the aerosol effects is still highly uncertain. The indirect effect is particularly uncertain as indicated by an error bar larger than the best estimate.

In air with elevated concentrations of CCN, the clouds contain higher concentrations of smaller cloud droplets, because the same amount of liquid water is distributed between more droplets (Twomey, 1977). These clouds reflect more solar radiation and appear "whiter". Moreover, the resulting reduction in the size of the droplets slows their coalescence into raindrops, which can lead to suppression of precipitation in shallow and short-lived clouds, hence increasing the cloud lifetime. In deep convective clouds, however, higher CCN concentrations can lead to greater convective overturning and

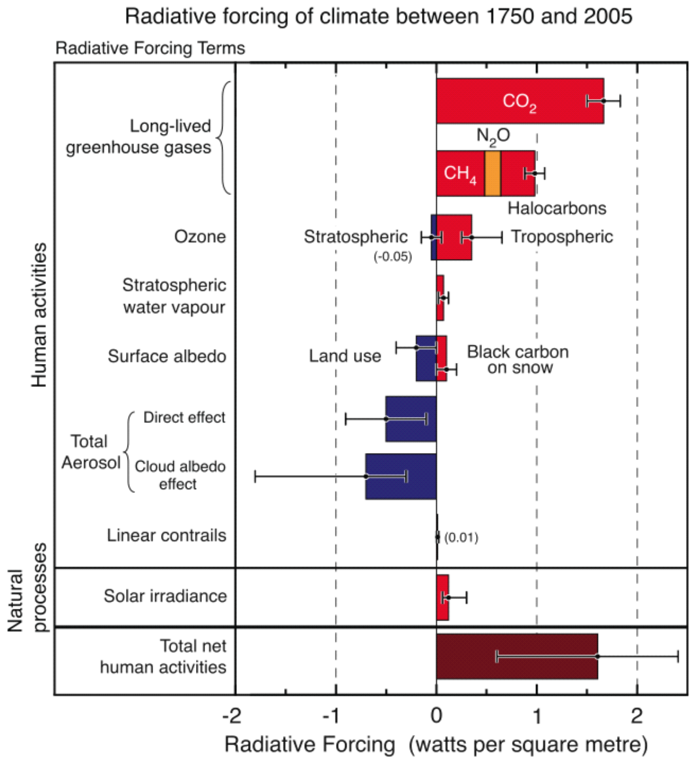

Figure 1.1: Summary of the principal components of the radiative forcing of climate change (from IPCC, 2007). All these radiative forcings result from one or more factors that affect climate and are associated with human activities or natural processes. The values represent the forcings in 2005 relative to the start of the industrial era (about 1750).

more precipitation (Fig. 1.2; Rosenfeld et al., 2008; Andreae and Rosenfeld, 2008).

1.3 Cloud droplet formation

In the Earth's atmosphere, cloud droplets generally do not form by homogeneous nucleation of supersaturated water vapor (i.e., condensation of water molecules from the gas phase in the absence of a preexisting condensation nucleus). This would require the initial formation of droplet embryos (clusters of water molecules) with a very small radius of curvature. Because of surface tension, however, the equilibrium vapor pressure over such a strongly curved surface is much greater than over a flat surface ("Kelvin effect" or "curvature effect"). Thus water vapor supersaturations of several hundred percent are needed for homogeneous nucleation of water droplets (Pruppacher and Klett, 1997; Andreae and Rosenfeld, 2008; Pöschl et al., 2009).

In the atmosphere, such high supersaturations are not reached, because aerosol particles facilitate the condensation of water vapor. This happens because the equilibrium water-vapor pressure over an aqueous solution is generally lower than over pure water ("Raoult effect" or "solute effect"; reduction of water activity), and thus water vapor can condense and form solution droplets on particles composed of soluble material (deliquescence and hygroscopic growth). Insoluble, but wettable particles can also facilitate droplet formation by decreasing the curvature effect for water adsorbed on the surface (depending on hydrophilicity and contact angle), and the uptake of water vapor on insoluble particles can be enhanced by soluble materials that are ubiquitous in the atmosphere (e.g., sulfuric acid).

By accounting for curvature and solute effects, the Köhler theory describes the hygroscopic

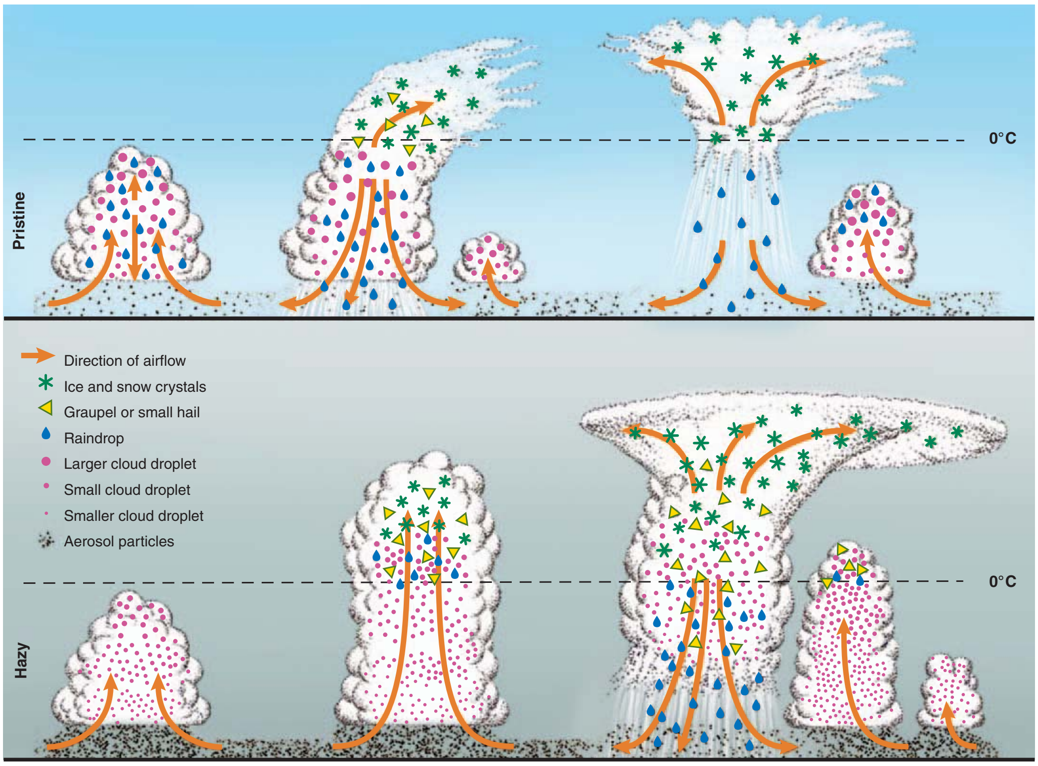

Figure 1.2: Evolution of deep convective clouds developing in the pristine (top) and polluted (bottom) atmosphere (from Rosenfeld et al., 2008).

growth and CCN activation of soluble aerosol particles as a function of relative humidity or water-vapor supersaturation, respectively (Seinfeld and Pandis, 2006; Pruppacher and Klett, 1997; McFiggans et al., 2006). The basic Köhler equation can be written as

$$s = a_\mathrm{w} \cdot Ke \tag{1.1}$$

The water vapor saturation ratio, s, is defined as the ratio of the actual partial pressure of water to the equilibrium vapor pressure over a flat surface of pure water at the same temperature. Expressed in percent, s is identical to the relative humidity (RH), which is typically used to describe the abundance of water vapor under sub-saturated conditions. Under supersaturated conditions (s>1, RH>100 %), it is customary to describe the abundance of water vapor by the so-called supersaturation S, which is expressed in percent and defined by:

$$S = (s - 1) \cdot 100\,\% \tag{1.2}$$

a_w is the activity of water in the aqueous solution (Raoult term), and Ke is the Kelvin term, which describes the enhancement of the equilibrium water vapor pressure due to surface curvature. The two terms can be described as follows:

$$a_\mathrm{w} \approx \exp\left(-\frac{B}{D_\mathrm{wet}^3}\right) \tag{1.3}$$

$$Ke \approx \exp\left(\frac{A}{D_\mathrm{wet}}\right) \tag{1.4}$$

The parameters A and B can be approximated by $A\approx(0.66\cdot 10^{-6}\,\mathrm{K\,m})\,/\,T$ and $B\approx\kappa\, D_\mathrm{s}^3$, respectively. D_wet is the droplet diameter, D_s is the dry solute mass equivalent diameter and κ is the effective

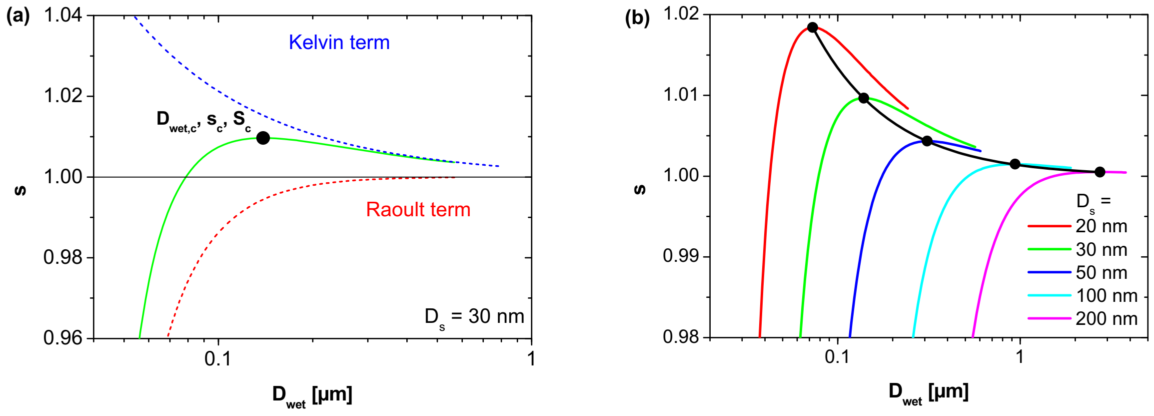

Figure 1.3: Köhler curves plotted for ammonium sulfate particles of **(a)** a dry diameter of 30 nm and **(b)** different dry sizes (colored lines). The dashed lines in panel (a) indicate the contribution of the Kelvin and the Raoult term to the Köhler equation. The black dots define the critical supersaturations (S_c), critical saturation ratios (S_c), and critical droplet diameters ($D_\mathrm{wet,c}$) (maxima of the Köhler curves). The black line in panel (b) is a curve for the approximation of S_c.

hygroscopicity parameter of the dry particle. For details and more precise modeling approaches see Sect. 2 and Appendix B.1.

Figure 1.3 a shows exemplary Köhler model calculations for an ammonium sulfate particle with a dry diameter of 30 nm ($\kappa \approx 0.6$, T=298 K). The Köhler curve (green line) represents the equilibrium between droplet size and water vapor supersaturation. Due to the different diameter dependences of the Kelvin term (blue line) and the Raoult term (red line), the Köhler curve exhibits a maximum, which is characterized by the critical droplet diameter ($D_\mathrm{wet,c}$) and the critical saturation ratio (s_c) or critical supersaturation (S_c). At D_wet<$D_\mathrm{wet,c}$ the shape of the Köhler curve is dominated by the Raoult term and the droplet is in stable equilibrium. At D_wet>$D_\mathrm{wet,c}$ the Kelvin term dominates, and the Köhler curve represents unstable equilibrium states (Seinfeld and Pandis, 2006). The hygroscopic growth of a 30 nm ammonium sulfate particle follows the ascending branch of the Köhler curve. When the saturation ratio and droplet size surpass the critical point (S_c, $D_\mathrm{wet,c}$) the droplet can form a cloud droplet and freely grow by further condensation as long as the saturation ratio remains above the Köhler curve. When the saturation ratio drops below the curve, the droplet shrinks until it reaches a stable equilibrium state on the ascending branch.

In Fig. 1.3 b the Köhler curves for ammonium sulfate particles with different dry diameters are illustrated (differently colored lines). Increasing dry particle size leads to lower S_c and larger $D_\mathrm{wet,c}$ values. The black line connecting the maxima of the different Köhler curves can be described by an exponential function as follows (Appendix B.6; Seinfeld and Pandis, 2006):

$$s_\mathrm{c} \approx \exp\left(\sqrt{\frac{4\,A^3}{27\,\kappa\,D_\mathrm{s}^3}}\right) \tag{1.5}$$

$$D_\mathrm{wet,c} \approx \frac{2\,A}{3\,s_\mathrm{c}} \tag{1.6}$$

The effective hygroscopicity parameter κ of an aerosol particle consisting of a mixture of solutes can be approximated by linear combination of the effective hygroscopicity parameters of the individual chemical components (κ_j) weighted by their volume fraction (ϵ_j) in the dry particle (Petters and

Kreidenweis, 2007).

$$\kappa \approx \sum_j \epsilon_j \, \kappa_j \tag{1.7}$$

Insoluble components can be described by κ_j=0, and limited solubility can be taken into account as described by Petters and Kreidenweis (2008) and Kreidenweis et al. (2009). For fully soluble components, κ_j is directly related to the molar mass (M_j), density (ρ_j), and van't Hoff factor (i_j) or stoichiometric dissociation number and osmotic coefficient ($\nu_j \, \Phi_j$) of the solute and of water (subscript w), respectively (Appendix B):

$$\kappa_j = i_j \frac{\rho_j \, M_\mathrm{w}}{\rho_\mathrm{w} \, M_j} \approx \nu_j \, \Phi_j \frac{\rho_j \, M_\mathrm{w}}{\rho_\mathrm{w} \, M_j} \tag{1.8}$$

Accordingly, κ_j can be regarded as an effective or equivalent molar density of soluble ions or molecules in the dry solute, normalized by the molar density of water molecules in liquid water ($\sim$55 mol L^{-1}). For compounds with low molecular mass (including most inorganic salts like sulfates, nitrates, chlorides as well as mono- or dicarboxylic acids, monosaccharides, etc.), the effective molar density of ions or molecules is usually close to the actual molar density of ions/molecules (i.e., the osmotic coefficients are close to unity).

Characteristic values of κ_j are in the range of $\sim$1.3 for NaCl, $\sim$0.6 for $(NH_4)_2SO_4$, $\sim$0.2 for levoglucosan, and $\sim$0.1 for secondary organic aerosols (Petters and Kreidenweis, 2007; Mikhailov et al., 2009; King et al., 2010). Laboratory experiments with biomass burning aerosols yielded κ values ranging from 0.02 to 0.8 (Petters et al., 2009). The available data suggest that after short aging on a timescale of hours, most pyrogenic aerosols are expected to have κ values in the range of 0.1 to 0.3 (Andreae and Rosenfeld, 2008; Kreidenweis et al., 2009; Pöschl et al., 2009). Prior to this study, however, field measurement data on the variability and size-dependence of the effective hygroscopicity of CCN were scarce.

1.4 Aims and objectives

The major aims of this study include the development and validation of reliable methods for size-resolved CCN measurements; the acquisition of high-quality field measurement data in continental regions with different levels of anthropogenic pollution; and the development and application of formalisms for efficient description and prediction of CCN properties and concentrations. The specific objectives and activities of the PhD work can be summarized as follows:

1. The reliability of CCN measurements results has been a subject of continuing debate. At the beginning of this study, an instrument promising enhanced robustness and high time resolution became commercially available: The continuous-flow CCN counter by Droplet Measurement Technologies (DMT-CCNC), which is applied in this study and has become widely used over the past years. Although the DMT-CCNC may appear as a "plug and play instrument", it needs to be carefully calibrated and operated in order to provide reliable data. In the course of this study robust calibration and measurement procedures have been developed and optimized. The uncertainties have been characterized in extensive calibration and test experiments during laboratory and field campaigns using well-defined model aerosols as well as complex mixtures (ammonium sulfate, sodium chloride, levoglucosan, spark-discharge soot) (Sect. 2). Moreover, the

uncertainties of the various Köhler models and thermodynamic parameterizations commonly used in CCN studies have been assessed, and suitable approaches for accurate calibration have been identified (Appendix B and Sect. 2.3.7 and 2.3.8).

2. CCN measurements in polluted mega-city air and biomass burning smoke were performed during a one month field campaign in the Pearl River Delta, China (PRIDE-PRD2006, 1–30 July 2006, Sect. 3). The measurement results (hygroscopicity parameters, CCN number concentrations and size distributions) and implications for the modeling of CCN concentrations are presented and discussed in Sect. 3.3. The effects of chemical composition and mixing state on the CCN activity of aerosol particles are investigated in Sect. 3.4. Additional measurements in polluted air were performed near the city of Beijing, China, in the course of a campaign aimed at the improvement of air quality for the Olympic Summer Games 2008 (CAREBeijing-2006, 11 August to 9 September 2006). CCN measurements at a remote continental location were performed during field campaigns at the Jungfraujoch observatory in the Swiss Alps (CLACE-5 and -6; 22 February to 21 March 2006 and 17 February to 14 March 2007, respectively). Moreover, the research work performed within the PhD studies underlying this thesis also contributed to the investigation of CCN in pristine Amazonian rainforest air (AMAZE-08, 7 February to 14 March). An overview of measurement data acquired at these locations is given in Appendix C.

3. Different approaches for efficient description and parameterization of the measurement results have been developed and applied for predicting CCN number concentrations. The atmospheric implications of the results have been investigated in cloud model studies as discussed in the conclusions section and related publications.

2 Calibration and measurement uncertainties of the CCN counter[1]

2.1 Introduction

The activation of cloud condensation nuclei (CCN), i.e., the formation of cloud droplets by the condensation of water vapor on aerosol particles, is determined by particle size and composition as well as water vapor supersaturation (Charlson et al., 2001; Segal et al., 2004; Andreae et al., 2005; McFiggans et al., 2006; Andreae et al., 2007).

Reliable measurement data of atmospheric CCN concentration and size distribution as a function of water vapor supersaturation are required for the quantitative description, understanding, and assessment of the effects of natural background aerosols and anthropogenic pollution on the atmosphere and climate. Therefore, CCN measurements have been performed in laboratory and field experiments around the globe, and more are under way (e.g., Gras, 1995; Hudson and Xie, 1999; Delene and Deshler, 2001; Giebl et al., 2002; Hudson and Yum, 2002; Raymond and Pandis, 2003; Bilde and Svenningsson, 2004; Broekhuizen et al., 2004; Henning et al., 2005; Dusek et al., 2006; Reade et al., 2006; Roberts et al., 2006; Broekhuizen et al., 2006; Dinar et al., 2006; Wex et al., 2006; Ervens et al., 2007; Rissman et al., 2007).

Instruments that measure CCN concentrations at prescribed water vapor supersaturations have been available and in use for decades, but the reliability of the measurement results has been a subject of continuing debate (e.g., Hudson, 1989, 1993; Chuang et al., 2000; Delene and Deshler, 2000; Snider et al., 2003; Chan and Chan, 2005; Wex et al., 2005; McFiggans et al., 2006; Snider et al., 2006).

Only a few years ago has an instrument promising enhanced robustness and reliability become commercially available: the continuous-flow streamwise thermal-gradient cloud condensation nuclei counter (CCNC) from Droplet Measurement Technologies (DMT). The design and operating principles of the instrument are based on Roberts and Nenes (2005) as detailed below. Numerous atmospheric research groups around the world have recently begun to use instruments of this type for CCN field and laboratory studies (e.g., Kuwata et al., 2007, 2008; Padró et al., 2007; Petters et al., 2007; Yum et al., 2007; Shilling et al., 2007; Engelhart et al., 2008).

In this chapter, it is described how the DMT-CCNC can be efficiently calibrated by experiments using salt aerosol particles of known size and composition, and the corresponding Köhler model calculations (Sect. 2.2, Appendix B). The variability and uncertainty of measurements and data analysis are investigated and quantified, and the applicability of a CCNC flow model by Lance et al. (2006) for extrapolating DMT-CCNC calibration results to different measurement conditions (temperature, pressure, flow rate) is tested. Moreover, the deviations between different Köhler modeling approaches are characterized, and the experimental and model results for ammonium sulfate and sodium chloride, addressing the influence of aerosol generation and particle shape are compared.

---

[1] This chapter is based on the manuscript "Calibration and measurement of a continuous-flow cloud condensation nuclei counter (DMT-CCNC): CCN activation of ammonium sulfate and sodium chloride aerosol particles in theory and experiment" by D. Rose, S. S. Gunthe, E. Mikhailov, G. P. Frank, U. Dusek, M. O. Andreae, and U. Pöschl, published in Atmos. Chem. Phys. (Rose et al., 2008).

2.2 Methods

2.2.1 Cloud condensation nuclei counter (CCNC)

The CCNC used and characterized in this PhD work is a continuous-flow streamwise thermal-gradient CCN counter, commercially available from Droplet Measurement Technologies, Inc. (DMT, model No. CCN-2, serial number 02/05/0011). The design and operating principles of the instrument are based on Roberts and Nenes (2005). The core of the DMT-CCNC is a vertical flow tube of cylindrical shape (inner diameter 2.3 cm, length 50 cm), in which the aerosol sample, surrounded by filtered sheath air (total flow rate Q=0.5–1 L min^{-1}, sheath-to-aerosol flow ratio 10), flows from top to bottom under laminar conditions and near-ambient pressure p. The porous inner surface of the flow tube is continuously wetted with liquid water from a peristaltic pump. In this study, the pump was generally operated at a water drip rate of 4 mL h^{-1} corresponding to the CCNC software setting of “low” liquid flow. In the CCNC, a near-linear positive temperature gradient along the flow direction is established and controlled by thermal electric coolers (TEC) and thermocouples, which are mounted at the beginning, middle, and end of the outer wall of the tube (temperatures T_1, T_2, and T_3, respectively). As the laminar flow passes through the column, heat and water vapor are transported from the inner surface towards the center of the tube. Because water molecules diffuse more quickly than heat, a constant water vapor supersaturation is established along the centerline of the column.

The aerosol sample enters the column at the top center of the column, and particles with a critical supersaturation less than the centerline supersaturation are activated as CCN (for definitions of supersaturation and critical supersaturation see Sect. 2.2.3). The residence time in the column ($\sim$6–12 s, depending on flow rate) enables the activated particles to grow into droplets that are sufficiently large ($>$1 $\mu\mathrm{m}$) to be detected separately from unactivated particles (usually $\ll$1 $\mu\mathrm{m}$). An optical particle counter (OPC) at the exit of the column determines the concentration and size distribution of droplets in the size range of 0.75–10 $\mu\mathrm{m}$. Droplets larger than 1 $\mu\mathrm{m}$ are considered to be activated CCN.

The effective water vapor supersaturation (S_{eff}) in the CCNC is determined by flow rate, pressure, sample temperature and temperature gradient. The temperature gradient is controlled by the temperature difference (ΔT=T_3–T_1) between the top (T_1, set $\sim$3 K higher than the sample temperature) and the heated bottom of the column (T_3, maximum $\sim$325 K, limited by OPC operating conditions). The CCNC operating software automatically keeps T_2 slightly higher than it would have to be for a perfectly linear gradient ($\sim$1 %). This results in a slightly higher temperature gradient in the first half and smaller temperature gradient in the second half of the flow column, which helps to restrict the actual CCN activation of aerosol particles to the first half of the column and to ensure sufficient time for droplet growth in the second half of the column. In this study, ΔT and S_{eff} have been varied in the range of 2–17 K (corresponding to gradients of 4–34 K m^{-1}) and 0.05–1.3%, respectively. Shifting from one supersaturation level to another requires approximately 0.5–3.5 min, depending on the size of the step, and whether it is from lower to higher supersaturations (shorter time) or vice versa (longer time).

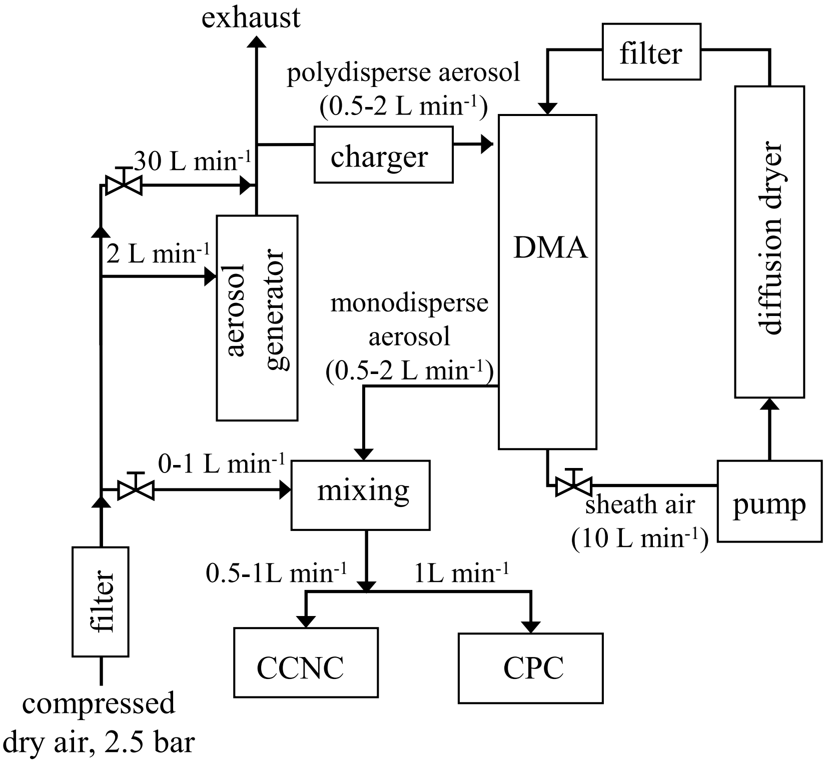

Figure 2.1: Experimental setup: DMA – differential mobility analyzer, CCNC – cloud condensation nuclei counter, CPC – condensation particle counter.

2.2.2 Experimental setup and aerosol generation

The calibration setup used in this PhD work was similar to the one described by Frank et al. (2007), and is illustrated in Fig. 2.1. Calibration aerosol was generated by nebulization of an aqueous salt solution (solute mass concentration ~0.01%) of ammonium sulfate ($(NH_4)_2SO_4$, purity >99.5%, supplier: E. Merck, Darmstadt) or sodium chloride (NaCl, purity >99.99%, supplier: Alfa Aesar GmbH & Co KG), using a TSI 3076 Constant Output Atomizer operated with particle-free pressurized air (2.5 bar, $2\,\mathrm{L\,min^{-1}}$). The polydisperse aerosol was dried to a relative humidity of <15% by dilution with particle-free dry air ($\sim30\,\mathrm{L\,min^{-1}}$). The excess flow was vented through a filter (HEPA) or into a fume hood/exhaust line, where care was taken to keep overpressure in the system as low as possible (mostly <20 Pa). The dry aerosol (0.5–$2\,\mathrm{L\,min^{-1}}$) was passed through a bipolar charger/radioactive neutralizer (Ni-63, 555 MBq) to establish charge equilibrium, and a differential mobility analyzer (DMA; TSI 3071 Electrostatic Classifier) with closed loop sheath air flow ($10\,\mathrm{L\,min^{-1}}$) was used to select monodisperse particles. To adjust the particle number concentration, the monodisperse aerosol was diluted with particle free air (0–$1\,\mathrm{L\,min^{-1}}$) in a small mixing chamber (glass, $\sim10\,\mathrm{cm^3}$, built in-house) at the DMA outlet. After dilution, the monodisperse aerosol flow was split into two parallel lines and fed into a condensation particle counter (CPC; TSI 3762; $1\,\mathrm{L\,min^{-1}}$) and into the CCNC (0.5–$1\,\mathrm{L\,min^{-1}}$). For the calibration experiments, the number concentration of monodisperse aerosol particles was kept below $\sim3\times10^3\,\mathrm{cm^{-3}}$ to avoid counting errors caused by coincidence.

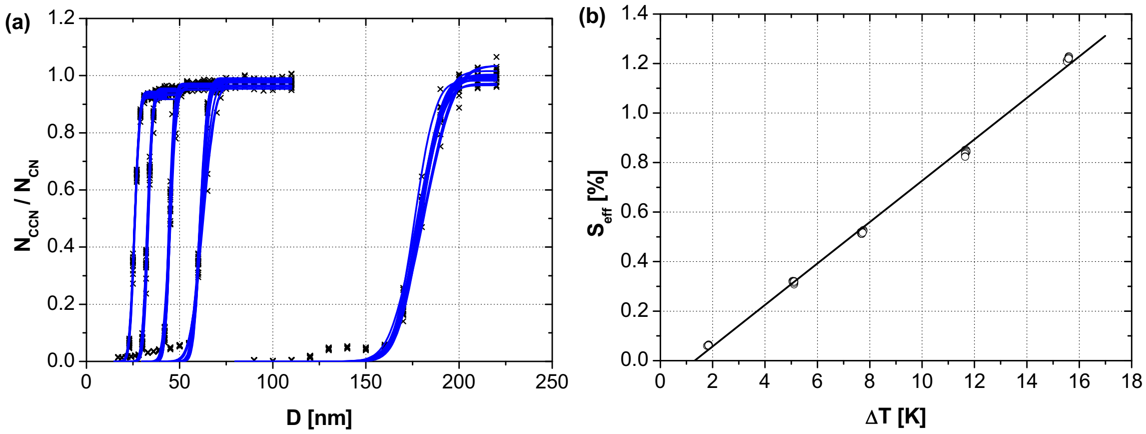

Figure 2.2: Exemplary results of a laboratory calibration experiment with ammonium sulfate aerosol (Mainz, 21 December 2005, Q=0.5 L min^{-1}, p=1026 hPa, T_1=298.5 K): **(a)** CCN efficiency spectra measured at 5 different ΔT values and **(b)** the corresponding calibration line. The symbols are measurement data points and the solid lines are the (a) cumulative Gaussian distribution and (b) linear fit curves.

2.2.3 Calibration experiments and data analysis

2.2.3.1 Measurement and fitting procedure

In every calibration experiment, the CCNC was operated at five different ΔT values in the range of 2–17 K. For each ΔT, the diameter of the dry salt aerosol particles selected by the DMA (D) was set to 15 different values in the range of 18–220 nm. At each D, the number concentration of total aerosol particles (condensation nuclei, CN), N_{CN}, was measured with the CPC, and the number concentration of CCN, N_{CCN}, was measured with the CCNC (~60 s waiting time to adjust to the new particle concentration plus 20–30 s averaging time). The activated particle fraction, or CCN efficiency ($N_{\mathrm{CCN}}/N_{\mathrm{CN}}$), was calculated from the averaged concentrations of CN and CCN, and a CCN efficiency spectrum of $N_{\mathrm{CCN}}/N_{\mathrm{CN}}$ over D was obtained from every scan of particle diameters at constant ΔT. In each calibration experiment, multiple scans over ΔT and D were performed, and multiple CCN efficiency spectra (at least 2, up to 20) were recorded for each ΔT (Fig. 2.2 a).

Each CCN efficiency spectrum was fitted with a cumulative Gaussian (normal) distribution function (CDF) using a nonlinear least-squares fitting routine (Gauss-Newton method, Matlab, MathWorks, Inc.):

$$f_{N_{\mathrm{CCN}}/N_{\mathrm{CN}}} = a\left(1+\mathrm{erf}\left(\frac{D-D_{\mathrm{a}}}{\sigma\sqrt{2}}\right)\right) \tag{2.1}$$

where erf is the error function, a is half the maximum value of $f_{N_{\mathrm{CCN}}/N_{\mathrm{CN}}}$, D_{a} is the particle diameter at $f_{N_{\mathrm{CCN}}/N_{\mathrm{CN}}} = a$, and σ is the standard deviation of the CDF. Ideally, a should equal 0.5 for internally mixed aerosols. As can be seen from exemplary CCN efficiency spectra illustrated in Fig. 2.2 a, however, deviations from this value can occur due to different particle losses and counting efficiencies of the CPC and CCNC. These deviations can be corrected by normalizing the maximum value of the CCN efficiency spectrum to unity, i.e., by multiplying the observed values of $N_{\mathrm{CCN}}/N_{\mathrm{CN}}$ with $0.5/a$. Since the normalization is symmetric with regard to the midpoint of the CCN efficiency spectrum, however, it does not affect the value of D_{a} (Rose et al., 2007).

2.2.3.2 Correction for doubly charged particles

When the DMA selects particles of a given electrical mobility, the particles are not all singly charged. There are also multiply (mostly doubly) charged particles that have the same electrical mobility, but which are larger in diameter. Since the probability of three charges or more is rather low, only doubly charged particles will be mentioned here. Because of their larger diameter, the doubly charged particles activate at a lower supersaturation than the singly charged particles of the same electrical mobility. Therefore, doubly charged particles appear in the CCN efficiency spectrum ($N_{\mathrm{CCN}}/N_{\mathrm{CN}}$ vs. D) of a chemically homogeneous aerosol as a plateau at smaller diameters (see Fig. 2.2 a). The height of this plateau corresponds to the number fraction of doubly charged particles. It usually increases for larger particle sizes (smaller supersaturations), because the probability of double charging increases (Wiedensohler, 1988). Furthermore, the height of this plateau depends on the shape of the number size distribution of the polydisperse calibration aerosol. The broader the size distribution is, the higher is the concentration of large particles, and the higher is the fraction of doubly charged particles selected by the DMA. High fractions of activated doubly charged particles can distort the CCN efficiency spectra and the derived D_{a} values. This effect can be corrected by calculating the abundance of doubly charged particles from the number size distribution of the polydisperse calibration aerosol assuming a bipolar equilibrium charge distribution and then subtracting them from $N_{\mathrm{CCN}}/N_{\mathrm{CN}}$ as described in Frank et al. (2006).

An alternative method is to fit the sum of two cumulative Gaussian distribution functions to the measured CCN efficiency spectrum. This method yields 6 fit parameters defined in analogy to Eq. (2.1) (a_1, a_2, σ_1, σ_2, $D_{\mathrm{a},1}$, $D_{\mathrm{a},2}$). The midpoint of the first, lower distribution function ($D_{\mathrm{a},2}$) can be regarded as the diameter at which half of the doubly charged particles are activated; the midpoint of the second, upper distribution function ($D_{\mathrm{a},1}$) is taken as the diameter at which half of the singly charged particles are activated (D_{a}). However, this technique is only applicable when there are enough data points at the plateau of the doubly charged particles to be fitted. Moreover, it assumes that the fraction of doubly charged particles is constant over the whole size range.

A simpler method to correct the CCN efficiency spectra for doubly charged particles, is to determine the fraction of activated doubly charged particles from the level of the smaller plateau in the spectrum, $(N_{\mathrm{CCN}}/N_{\mathrm{CN}})_2$. Assuming that this fraction is constant over the whole particle size range, the activated fraction of singly charged particles, $(N_{\mathrm{CCN}}/N_{\mathrm{CN}})_1$, can be calculated from the measured number concentrations as follows:

$$(N_{\mathrm{CCN}}/N_{\mathrm{CN}})_1 = \frac{N_{\mathrm{CCN}} - N_{\mathrm{CN}} \cdot (N_{\mathrm{CCN}}/N_{\mathrm{CN}})_2}{N_{\mathrm{CN}} - N_{\mathrm{CN}} \cdot (N_{\mathrm{CCN}}/N_{\mathrm{CN}})_2} \tag{2.2}$$

The function given in Eq. (2.1) is then fitted to the corrected CCN efficiency spectrum ($(N_{\mathrm{CCN}}/N_{\mathrm{CN}})_1$ vs. D) to obtain D_{a}.

The effects of doubly charged particles on the CCNC calibration results will be discussed in Sect. 2.3.1. In the calibration experiments performed during the course of this PhD work, corrections for doubly charged particles have been applied only in the data processing of experiments where the fraction of activated doubly charged particles, $(N_{\mathrm{CCN}}/N_{\mathrm{CN}})_2$, exceeded the value of 0.1, unless mentioned otherwise.

2.2.3.3 Correction for DMA transfer function

Ideally, the CCN efficiency spectra of internally mixed aerosols should have the shape of a step function, where all particles larger than the critical dry diameter (D_c) are activated ($N_\mathrm{CCN}/N_\mathrm{CN}=1$) and all smaller particles are non-activated ($N_\mathrm{CCN}/N_\mathrm{CN}=0$). The particle size resolution that can be achieved upon selection of a monodisperse aerosol with a DMA, however, is limited by the transfer function of the DMA. Thus the selected monodisperse aerosol consists not only of particles with the selected nominal mobility equivalent diameter, but it also contains smaller and larger particles. The activation of these particles results in a widening of the observed CCN efficiency spectrum, i.e., to a gradual rather than stepwise increase of $N_\mathrm{CCN}/N_\mathrm{CN}$ with D (see Fig. 2.4). Due to the asymmetry of the DMA transfer function, the widening does not only increase the standard deviation of the CDF fit (σ), but it can also shift the midpoint of the CCN efficiency spectrum (D_a). The transfer function effect can be corrected by transforming each of the experimentally selected nominal mobility equivalent diameters (D_nom) into an effective diameter (D_eff). D_eff is the diameter for which the fraction of selected particles with diameters $\geq D_\mathrm{eff}$ ($N_{\mathrm{CN,D}\geq\mathrm{D_{eff}}}/N_\mathrm{CN}$) equals the observed fraction of activated particles ($N_\mathrm{CCN}/N_\mathrm{CN}$).

To correct for the transfer function effect, the following procedure can be applied to each data point in the CCN efficiency spectrum:

1. The nominal electrical mobility, Z_nom, which corresponds to the selected nominal electrical mobility diameter D_nom is calculated according to standard DMA equations, inserting the operating conditions and dimensions of the DMA (Willeke and Baron, 2001).

2. The half-width of the transfer function is calculated from the relation $\Delta Z_\mathrm{nom}=Z_\mathrm{nom}\,Q_\mathrm{ae}/Q_\mathrm{sh}$, where Q_ae is the aerosol flow and Q_sh is the sheath air flow through the DMA (Knutson and Whitby, 1975).

3. The lower and upper boundaries of the transfer function on the scale of electrical mobility are calculated as $Z_l=Z_\mathrm{nom}+\Delta Z_\mathrm{nom}$ and $Z_u=Z_\mathrm{nom}-\Delta Z_\mathrm{nom}$, respectively. The corresponding lower and upper boundaries of the transfer function on the scale of particle diameter, D_l, D_u, are calculated according to standard DMA equations (Willeke and Baron, 2001). The theoretical transfer function of the DMA at the selected particle size, P_nom, is given as a piecewise linear probability function of triangular shape which is 0 for $D\leq D_l$, 1 at D_nom, and again 0 for $D\geq D_u$ (Willeke and Baron, 2001).

4. The number size distribution function of the monodisperse aerosol at the selected particle size, ψ_m, is calculated by multiplying P_nom with the size distribution function of polydisperse calibration aerosol, ψ_p, which was measured in parallel to the CCN efficiency measurements. Note that P_nom can be used instead of ψ_m if the investigated polydisperse aerosol has a broad size distribution that does not vary strongly over the width of the transfer function (this is typically the case for ambient aerosols).

5. The corrected (effective) diameter (D_{eff}) is calculated by numerical iteration to reproduce the CCN efficiency observed at the selected diameter with the following relation:

$$N_{\text{CCN}}/N_{\text{CN}} = \frac{\int_{D_{\text{eff}}}^{D_u} \psi_m \, \mathrm{d}D}{\int_{D_l}^{D_u} \psi_m \, \mathrm{d}D} \tag{2.3}$$

The application of the transfer function correction requires that the maximum value of the CCN efficiency spectrum equals the true maximum CCN efficiency of the investigated aerosol particles passing through the DMA, i.e. unity for our salt calibration aerosols (normalization of the observed values of $N_{\text{CCN}}/N_{\text{CN}}$ with $0.5/a$ if $a{\neq}0.5$). Otherwise the correction would refer to an unrealistic CCN efficiency that is caused by different particle losses and counting efficiencies of the CPC and CCNC, and it would lead to a distorted CCN efficiency spectrum and D_{a}.

Moreover, the above correction is based on the assumption that the particles are internally mixed and exhibit no significant differences in composition over the size range of the transfer function and monodisperse aerosol, respectively. Under this assumption, it can also be applied to CCN efficiency spectra of atmospheric aerosols.

Note that both the width of the transfer function and the width of the CCN spectrum increase with increasing aerosol to sheath flow ratio in the DMA. D_{a} can shift to larger or smaller sizes (i.e., $D_{\text{eff}}{>}D_{\text{nom}}$ or $D_{\text{eff}}{<}D_{\text{nom}}$, respectively), depending on the shape of the particle size distribution. The effects of the DMA transfer function on the CCNC calibration results will be discussed in Sect. 2.3.2. In this study, corrections for the DMA transfer function have been applied only where explicitly mentioned.

2.2.3.4 Correction for particle shape

In a DMA, the particle size is selected according to the electrical mobility equivalent diameter, which assumes a spherical shape of the particles. In the case of non-spherical particles, the mobility equivalent diameter (D_B) selected by the DMA is generally larger than the mass equivalent diameter (D_m). Thus the application of mobility equivalent diameters for Köhler model calculations can lead to an underestimation of the effective supersaturation in the CCNC. Sodium chloride particles generated by nebulization of a NaCl solution and subsequent drying are usually of cubic shape (Scheibel and Porstendörfer, 1983; Krämer et al., 2000; Mikhailov et al., 2004). Also ammonium sulfate particles generated by nebulization and drying may not be fully spherical and compact (Biskos et al., 2006a). The effects of particle shape and porosity can be described with the dynamic shape factor χ, which is defined as the ratio of the drag force experienced by the particle in question to that of a sphere of equivalent mass (Krämer et al., 2000):

$$\chi = \frac{D_B \, C(D_m)}{D_m \, C(D_B)} \tag{2.4}$$

in which $C(D_B)$ and $C(D_m)$ are the slip correction factors for the respective diameters D_B and D_m. $C(D)$ can be approximated by the empirical relation (Willeke and Baron, 2001):

$$C(D) = 1 + \frac{2\,\lambda}{D}\left(1.142 + 0.558 \, \exp\left(-0.999\frac{D}{2\,\lambda}\right)\right) \tag{2.5}$$

in which λ is the mean free path of the gas molecules (λ=68 nm in air at 298 K and standard atmospheric pressure).

When applying a shape correction, the particle diameters selected by the DMA (D=D_B) have to be transformed into mass equivalent diameters D_m by iteratively solving Eq. (2.4) with Eq. (2.5). Upon CCNC calibration, the transformation of D=D_B into D_m can be performed for the complete CCN efficiency spectrum prior to fitting, or just for the activation diameter obtained from a fit to the uncorrected spectrum. Both approaches lead to the same value of a shape-corrected activation diameter D_a, which can then be taken as the critical dry particle diameter for Köhler model calculations to determine the effective supersaturation in the CCNC as described below.

For ammonium sulfate particles generated by nebulization, a shape factor of χ=1.02 has been recommended (Biskos et al., 2006a). For sodium chloride particles, different shape factors have been used: a constant value of $\chi = 1.08$ (Krämer et al., 2000; Mikhailov et al., 2004, e.g.,) or size-dependent values in the range of 1.08-1.24 (Biskos et al., 2006b; DeCarlo et al., 2004).

The effects of different shape corrections on the calibration results will be discussed in Sect. 2.3.8. In this study, corrections for particle shape have been applied only where explicitly mentioned.

2.2.3.5 Determination of effective supersaturation (S_eff)

The diameter at which the CCN efficiency spectrum reaches half its maximum, i.e., the activation diameter D_a as obtained from the fit to the experimental data (with or without corrections for doubly charged particles, DMA transfer function, and particle shape), can be regarded as the critical dry particle diameter for CCN activation, D_c, i.e., the diameter that is required for particles of the given composition to be activated as CCN at the given supersaturation.

For soluble materials, D_c can be taken as the mass equivalent diameter of the dry solute particle, D_s, and through Köhler theory it can be related to the critical supersaturation, which is the minimum supersaturation required to activate particles of the given size and composition as CCN. S_c in turn can be regarded as the effective water vapor supersaturation in the CCNC (S_eff) at the given operating conditions (ΔT, p, T_1, Q). Thus Köhler model calculations as detailed in Appendix B.4 were performed to determine S_eff (=S_c) from D_a (=D_s), using the Köhler model VH4 and inserting T_1 for T unless mentioned otherwise.

From each of the multiple CCN efficiency spectra recorded at each of the temperature differences investigated within a calibration experiment, one data point was obtained in a calibration diagram of S_eff vs. ΔT. A linear calibration function, f_s=$k_s\,\Delta T$+S_0, was obtained by a linear least-squares fit to these data points. One exemplary calibration line is illustrated in Fig. 2.2 b. The fit parameters of the calibration function (k_s, S_0) can be used in the CCNC software to calculate and set appropriate temperature differences, ΔT, for CCN measurements at desired water vapor supersaturations, S_eff.

2.2.4 CCNC flow model

Roberts and Nenes (2005) introduced a model that describes the relationship between the temperature difference and S_eff in the DMT-CCNC column under certain operating conditions. Input variables to the model are the volumetric flow rate, the sheath-to-aerosol flow ratio, the pressure, and the inner wall streamwise temperature difference (ΔT_{inner}) between the exit and the entrance of the column. Lance et al. (2006) compared the simulated instrument responses for calibration aerosol against actual measurements. They indicated that the supersaturation strongly depends on ΔT_{inner} which may be only a fraction of the temperature difference imposed by the TECs at the outer wall of the column (ΔT=T_3-T_1). It is assumed that the inner temperature at the entrance of the column ($T_{1,\text{inner}}$) equals the entrance temperature measured outside the column, i.e., T_1. The temperature drop across the wall – the quotient of ΔT_{inner} to ΔT – is called the thermal efficiency η ($\eta \leq 1$) and varies with the operating conditions. η has to be determined to predict the S_{eff} of the instrument and can be calculated if the thermal resistance (R_T) of the column is known.

Following the procedure suggested by Lance et al. (2006), the thermal resistance of the used instrument was calibrated before estimating the thermal efficiency and the supersaturation in the CCNC under different operating conditions. The supersaturation was first determined experimentally by calibrating the CCN counter with ammonium sulfate particles of known size at different ΔT values and inferring S_{eff} by converting the critical diameter into S_{c} via Köhler model calculations. The calibration line (S_{eff} vs. ΔT) did not go through the origin of the coordinate system, but intercepted the x-axis at a certain ΔT_0 (cf. Fig. 2.2 b). Since the model assumes that S=0 if ΔT_{inner}=0 and thus ΔT=0, the calibration line was shifted to the left by subtracting its ΔT_0 from each ΔT, which led to a new calibration line of S_{eff} vs. ΔT* (ΔT*=ΔT–ΔT_0). Each pair of ΔT* and S_{eff} was taken to determine ΔT_{inner} by solving Eq. (16) in Lance et al. (2006) iteratively. The corresponding thermal efficiency η was calculated dividing ΔT_{inner} by ΔT*, and the corresponding thermal resistance R_{T} was calculated by solving Eq. (15) of Lance et al. (2006).

An average value of R_{T} was taken as the effective thermal resistance of the CCNC and used to model the effective supersaturation for various operating conditions (T_1, p, Q) as follows: For a given ΔT, ΔT* was calculated by subtracting a standard offset value of ΔT_0=1 K (or ΔT_0=2 K for Q=1 L min^{-1}) and inserted into Eq. (15) of Lance et al. (2006) to calculate η. The inner wall temperature difference, ΔT_{inner}, was determined by multiplication of η with ΔT*, and finally, S_{eff} was calculated using Eq. (16) of Lance et al. (2006).

2.3 Results and discussion

2.3.1 Effect of doubly charged particles on CCN efficiency spectra

Figure 2.3 shows exemplary CCN efficiency spectra and fit curves used to determine the dry particle activation diameter, D_{a}, which is the basis for calculating the effective water vapor supersaturation in the CCN counter, S_{eff} (Sect. 2.2.3.5). As outlined in Sect. 2.2.3.2, CCN efficiency spectra recorded by particle size selection with a differential mobility analyzer can be influenced by doubly charged particles (Fig. 2.3) which interfere with the determination of D_{a}.

The measured spectrum in Fig. 2.3 a exhibits a high fraction of activated doubly charged particles (plateau level $\sim$0.17). The fit with a single cumulative Gaussian distribution function (Eq. 2.1) strongly deviated from the measured data points and gave a D_{a} value $\sim$2% smaller than the value obtained by fitting with two distribution functions. After correcting the measured spectrum with Eq. (2.2), the fit of Eq. (2.1) to the corrected spectrum gave the same D_{a} value as the fit of two distri-

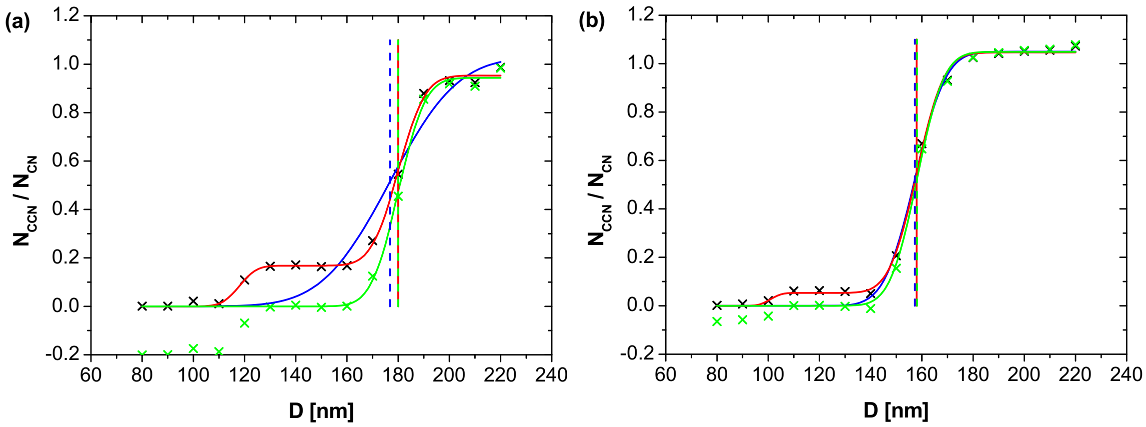

Figure 2.3: Alternative fitting methods and dry particle activation diameters (D_a) for exemplary CCN efficiency spectra of ammonium sulfate with **(a)** high and **(b)** low fractions of doubly charged particles. The black crosses are measured data points. The green crosses are data points obtained by correction with Eq. (2.2). The solid blue line is the fit of a cumulative Gaussian distribution function (Eq. 2.1) to the measured spectrum, and the solid green line is the fit of Eq. (2.1) to the corrected spectrum. The solid red line is the fit of two distribution functions to the measured spectrum. The vertical dashed lines are the D_a values obtained from the fit curves with the same color.

bution functions to the uncorrected spectrum, which can be regarded as the actual activation diameter. The ~2% increase of D_a led to a ~3% relative decrease of the effective supersaturation determined by Köhler model calculations.

The measured spectrum in Fig. 2.3 b exhibits a low fraction of activated doubly charged particles (plateau level ~0.06), and the fit with a single cumulative Gaussian distribution function (Eq. 2.1) agrees well with all data points at N_{CCN}/N_{CN} >0.1. Therefore, the D_a value obtained from this fit was only ~0.5% smaller than the values obtained after correcting the spectrum with Eq. (2.2), or fitting with two distribution functions. The corresponding relative change of S_{eff} was only 0.7%.

In this study, the observed fraction of activated doubly charged particles was generally in the range of 0–0.25. In most cases the fraction was <0.1 and a single cumulative Gaussian distribution (Eq. 2.1) fitted to the data points was used to determine D_a (relative deviations of D_a and $S_{eff} \leq 1\%$). For plateau levels >0.1, two cumulative Gaussian distributions were used.

2.3.2 Effect of DMA transfer function on CCN efficiency spectra

Figure 2.4 shows exemplary CCN efficiency spectra with and without correction for the DMA transfer function as described in Sect. 2.2.3.2. The correction leads to narrower CCN efficiency spectra with steeper slopes and smaller standard deviations of the fit function (uncorrected $\sigma/D_a \approx 10\%$, corrected $\sigma/D_a \approx 4\%$). The small residual values of σ obtained after correction (< 1–5 nm) indicate high precision of the experiments; they can be attributed to small heterogeneities of the supersaturation profile in the CCNC or other non-idealities such as particle shape effects. Depending on the size distribution of the polydisperse calibration aerosol and of the monodisperse aerosol selected by the DMA, the correction can shift D_a either towards smaller or towards larger diameters. In the above example and other tests, however, the influence on D_a and S_{eff} was very small (relative changes < 1%), and thus the calibration results were generally not corrected for the DMA transfer function unless mentioned

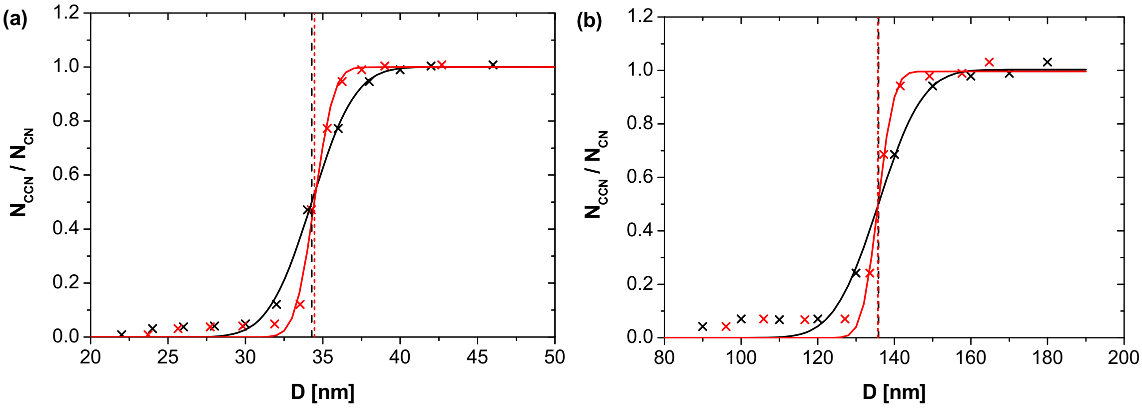

Figure 2.4: Correction for DMA transfer function in exemplary CCN efficiency spectra of ammonium sulfate with **(a)** small and **(b)** large dry particle activation diameter (D_{a}). The black crosses are measured data points. The red crosses are data points obtained by correction according to Sect. 2.2.3.2. The solid lines are fits of a cumulative Gaussian distribution function (Eq. 2.1) to the measured and corrected spectra, respectively. The vertical dashed lines are the D_{a} values obtained from the fit curves with the same color.

otherwise.

2.3.3 Measurement precision within a laboratory experiment

Figure 2.2 a shows the CCN efficiency spectra of an exemplary calibration experiment with ammonium sulfate particles. This experiment lasted for 26 h and was performed in the laboratory under stable conditions: sample temperature 296.3±0.2 K, CCNC column top temperature T_1=298.5 ± 0.2 K, pressure p=1026 ± 2 hPa (mean value ± standard deviation). The measurement data have been processed without applying any corrections for doubly charged particles, DMA transfer function, or particle shape.

Table 2.1 summarizes characteristic measurement parameters and results of the exemplary calibration experiment. For each of the 5 different ΔT values in the range of 2 – 16 K, 15 CCN efficiency spectra were recorded, and dry particle activation diameters D_{a} in the range of 26 – 178 nm were obtained by fitting with a cumulative Gaussian distribution function (Eq. 2.1). The 95% confidence interval for D_{a} was, on average, less than 2 nm, which confirms the skill of the fit function used. The relative standard deviations of D_{a} were only 0.3 – 1.4 %, indicating high instrument stability and measurement precision under constant surrounding conditions.

Using the D_{a} values obtained from the individual CCN efficiency spectra, critical supersaturations S_{c} were calculated as described in Sect. 2.2.3.5 and Appendix B.4 (Köhler model VH4), and these were taken as the effective supersaturations of water vapor in the CCNC, S_{eff}. As detailed in Tab. 2.1, the mean values of S_{eff} for the selected temperature differences were in the range of 0.06 – 1.22 %, and the relative standard deviations were 0.5 – 2.2 %, increasing with decreasing supersaturation.

As illustrated in Fig. 2.2 a, the upper limit values of the CCN efficiency spectra of the calibration aerosols (maximum activated fraction of particles) deviated hardly more than 5% from the ideally expected value of 1, indicating that the uncertainty of CCN efficiencies measured with the calibrated CCNC was on the order of ±5%. The accuracy of CCN concentration and efficiency measurements

Table 2.1: Measured and calculated parameters (arithmetic means and standard deviations) for the experiment shown in Fig. 2.2.

mean ΔT [K]	stdev. ΔT [K]	mean D_a [nm]	rel. stdev. D_a [%]	mean conf. interv. of D_a [nm]	mean S_eff [%]	rel. stdev. S_eff [%]	S_eff from calbr. line fit [%]	rel. dev. of S_eff from fit [%]
1.84	0.02	178.3	1.4	1.7	0.062	2.2	0.044	38.5
5.10	0.03	61.3	0.9	0.6	0.318	1.3	0.317	0.2
7.71	0.03	44.7	0.6	0.3	0.519	0.9	0.536	3.2
11.66	0.02	32.8	0.6	0.2	0.840	1.0	0.867	3.1
15.59	0.02	25.8	0.3	0.6	1.223	0.5	1.197	2.2

depends critically on particle losses in the experimental setup and on the counting efficiencies of the OPC used for the detection of activated particles/droplets (CCN) and of the CPC used for the measurement of total number concentration of size-selected aerosol particles (CN). For the determination of D_a and S_eff, however, in a series of test experiments performed upon instrument maintenance it was found that even strong variations of counting efficiency with particle size and concentration (deviations by up to 20%) had no strong effect on the determination of D_a and S_eff (relative variations <0.5 %).

Figure 2.2 b shows the calibration line of S_eff vs. ΔT, which is a linear fit to the data points obtained from each of the recorded CCN efficiency spectra (Sect. 2.2.3.5). The corresponding calibration function is S_eff=$0.0838\,\Delta T-0.1097$ with R^2=0.9974 (n=75). As detailed in Tab. 2.1, the fit line agrees well with the experimentally determined data points at $S_\mathrm{eff}>0.1\,\%$: the relative deviations hardly exceed 3 %. In spite of the high R^2 value, however, the relative deviation between fit line and data points at the lowest supersaturation ($S_\mathrm{eff}\approx0.06\,\%$) is as high as 38%. Apparently the dependence of S_eff on ΔT is not linear in this range, which is also indicated by the non-zero intercept of the calibration line with the x-axis (as discussed below) and needs to be taken into account for CCN measurements at low supersaturation. For studies aiming at high accuracy of S_eff, a second or third order polynomial may in fact be more appropriate than the linear calibration function.

2.3.4 Variability within and between different measurement campaigns

During the course of this PhD work, the DMT-CCNC has been operated and calibrated at a variety of locations and elevations: during two one-month field campaigns in Guangzhou and Beijing, China (close to sea level); at the home laboratory in Mainz and another laboratory in Leipzig, Germany (close to sea level); and at the mountain stations Hohenpeissenberg, Germany (900 m a.s.l.), and Jungfraujoch, Switzerland (3570 m a.s.l.). An overview of the calibration results is given in Fig. 2.5.

During the field campaign in Guangzhou (Fig. 2.5 a), the CCNC was operated with a flow rate of $0.5\,\mathrm{L\,min^{-1}}$ at a pressure of $\sim$1020 hPa, and the column top temperature T_1 varied between 298 and 303 K. An average calibration line of S_eff vs. ΔT for the whole campaign was obtained by a fit to all data points, excluding the experiment with T_1=303.2 K, which was not representative for the rest of the campaign. Apart from this exceptional experiment, the deviations between individual calibration lines and the average line were at most 5–7% (relative) with regard to S_eff. As will be discussed in

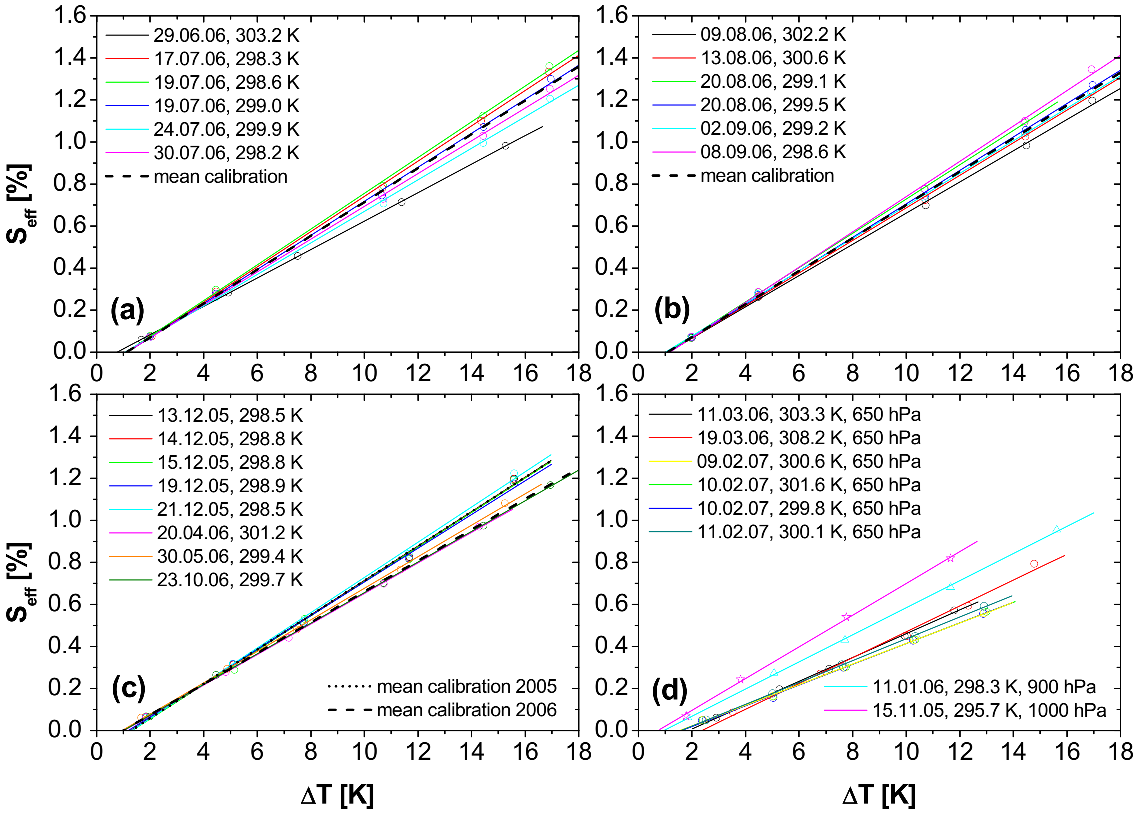

Figure 2.5: Measured (symbols) and fitted (solid lines) calibration lines obtained from field and laboratory experiments with ammonium sulfate aerosol at different CCNC column top temperatures (T_1) and different locations: **(a)** field campaign in Guangzhou, China; **(b)** field campaign in Beijing, China; **(c)** laboratory measurements in Mainz, Germany; **(d)** field campaigns at the mountain stations Hohenpeissenberg, Germany (900 hPa) and Jungfraujoch, Switzerland (650 hPa) and laboratory measurement in Leipzig, Germany (1000 hPa). The CCNC was operated at Q=0.5 L min^{-1} and p≈1020 hPa unless mentioned otherwise. The dotted and dashed black lines are mean calibration lines (see text).

more detail below (Sect. 2.3.6), S_{eff} and the slope of the calibration lines decreased with increasing T_1.

The calibration lines from the field campaign in Beijing (Q=0.5 L min^{-1}, p≈1020 hPa; Fig. 2.5 b) exhibited a similar pattern and influence of T_1, and the maximum deviations between individual lines and the average line were again in the range of 5–7% (relative).

Before and after the field campaigns, the CCNC was calibrated in the home laboratory (Mainz, p≈1020 hPa). In December 2005, a series of five calibration experiments extending over several days without changing the experimental setup were performed. The instrument was stopped in between measurement runs only to test the influence of small variations in the experimental conditions (changes of liquid water flow in the CCNC, dilution flow in aerosol generation, etc.). The resulting calibration lines are shown in Fig. 2.5c; the deviations between individual lines and the average were at most 2% (relative).

In 2006, three more laboratory calibration experiments were performed, where the time between each experiment was over one month and the experimental setup was newly arranged every time. The resulting three calibration lines also deviated not more than 2–3% from the corresponding average. As illustrated in Fig. 2.5c, the slope of the average calibration line from the series of experiments

Table 2.2: Calibration experiments used to test the CCNC flow model: experimental conditions and parameters of the linear calibration function.

name	date	location	p [hPa]	Q [L min^{-1}]	T$_1$ [K]	slope k_s [% K^{-1}]	intercept S_0 [%]
MZ05	19.12.2005	Mainz, lab	1023	0.5	298.9	0.0802	–0.0945
MZ10	23.12.2005	Mainz, lab	1021	1.0	298.4	0.1608	–0.3515
JF08	08.02.2007	Jungfraujoch, field	650	0.8	299.3	0.0804	–0.1111
JF05	10.02.2007	Jungfraujoch, field	650	0.5	301.6	0.0490	–0.0760
HP05	11.01.2006	Hohenpeissenberg, field	902	0.5	298.3	0.0645	–0.0604

in 2006 was considerably smaller (10% relative) than the slope of the average line obtained from the experiments in 2005. Only about half the difference can be attributed to higher temperatures during the 2006 experiments. The remaining difference is most likely due to usage- and aging-related changes of instrument properties (e.g., porosity and thermal resistance of the CCNC column; A. Nenes, personal communication, 2007).

Figure 2.5d shows the calibration lines measured during field campaigns at mountain stations (Hohenpeissenberg, 900 m a.s.l.; Mt. Jungfraujoch, 3570 m a.s.l.) and in a laboratory near sea level (Leipzig, 100 m a.s.l.). It illustrates that the supersaturation obtained at a given ΔT decreases significantly with pressure, which will be discussed in more detail in Sect. 2.3.6. For the two field campaigns on Mt. Jungfraujoch a similar long-term trend as for the lab experiments was found: the slopes of the calibration lines recorded in 2007 were about 10% smaller than those recorded one year before.

2.3.5 Application of the CCNC flow model

Lance et al. (2006) have presented a flow model describing the dependence of S_{eff} on temperature, pressure, and flow rate in the CCN counter. According to this model, the water vapor supersaturation in the CCNC increases linearly with the temperature gradient and equals zero at ΔT=0. As shown in Fig. 2.5, however, the experimentally determined calibration lines of S_{eff} vs. ΔT generally do not intercept the x-axis at ΔT=0. Instead, the calibration lines obtained at Q=0.5 L min^{-1} and 900–1020 hPa intercepted the x-axis at an offset around 1 K, and those obtained at 650 hPa at 1.5–2.3 K. The ΔT offset values of calibration lines determined under other conditions (not included in Fig. 2.5) were: 1.3–1.5 at Q=0.8 L min^{-1} and 650 hPa; 1.9–2.2 K at 1.0 L min^{-1} and $\sim$1000 hPa. To make the model applicable to the experimental results, the offset values (ΔT_0) have been subtracted as detailed in Sect. 2.2.4.

Four calibration experiments performed at different locations, altitudes and flow rates (cf. Tab. 2.2; MZ05, MZ10, JF05, JF08) were selected to determine the thermal resistance (R_T) of the CCN instrument as suggested by Lance et al. (2006) but using the Köhler model VH4 rather than the Köhler model VH4.b, which had been used by Lance et al. (2006) (Sect. 2.2.4). Figure 2.6 shows the calculated values of R_T plotted against ΔT. The R_T values exhibit substantial deviations between different calibration experiments and operating conditions. Especially at low ΔT, also strongly negative values of R_T were obtained, which are physically not realistic because they would correspond

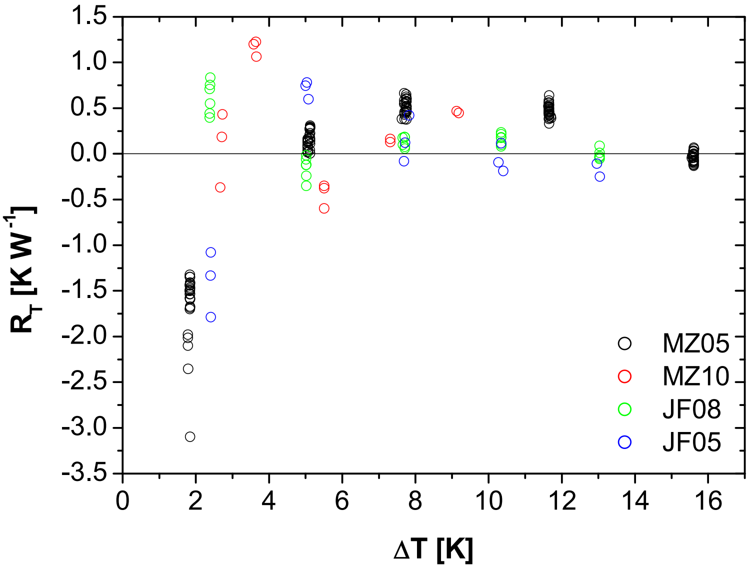

Figure 2.6: Thermal resistance derived from four CCNC calibration experiments with ammonium sulfate aerosol at different pressures and flow rates (MZ05, MZ10, JF08, JF05, cf. Tab. 2.2) by fitting the CCNC flow model of Lance et al. (2006)

to thermal efficiencies $>100\%$ (indicating that the temperature gradient inside the column would be larger than outside). Most likely, these R_T values were affected by non-idealities, which also caused the non-linear dependence of S_{eff} on ΔT observed at low ΔT. Thus only the R_T values determined at $\Delta T \geq 3$ K were used to calculate an arithmetic mean of 0.24 K W^{-1}, which can be taken as the effective thermal resistance of the CCNC unit used in this study. Note, however, that the effective thermal resistance determined as suggested by Lance et al. (2006) and outlined above depends on the applied Köhler model. Using the VH4.b Köhler model as applied by Lance et al. (2006), an average R_T value of 1.78 K W^{-1} was obtained for this CCNC column, which is still lower than but closer to the value reported by Lance et al. (2006) for their instrument (3.4 ± 0.5 K W^{-1}). As discussed below (Sect. 2.3.7), different Köhler models can yield substantially different results, and the S_{eff} values predicted with CCNC flow models using effective thermal resistances that have been determined with different Köhler models can vary accordingly.

Using the flow model with R_T=0.24 K W^{-1} and with a standard temperature offset of ΔT_0=1 K as described in Sect. 2.2.4, model calibration lines have been calculated for the exemplary flow conditions listed in Tab. 2.2 and compared to the experimental calibration data obtained with the Köhler model VH4. As illustrated in Fig. 2.7, the model lines agree fairly well with the experimentally determined data – also for the experiment HP05, which had not been included in the determination of R_T. The relatively high uncertainty of R_T (Fig. 2.6: variability $\gg$ 100 %) appears to have only a relatively weak influence on the performance of the flow model.

At high supersaturation, the relative deviations between the flow model and measurement data of S_{eff} were on average +2 % for MZ05, +3 % for JF08, +6 % for JF05, and +8 % for HP05. At low supersaturation (<0.1 %), however, the deviations increased up to 42 % (relative). Obviously, the non-idealities and non-linear dependence of S_{eff} on ΔT experimentally observed at low ΔT cannot be captured with the flow model that predicts a linear dependence.

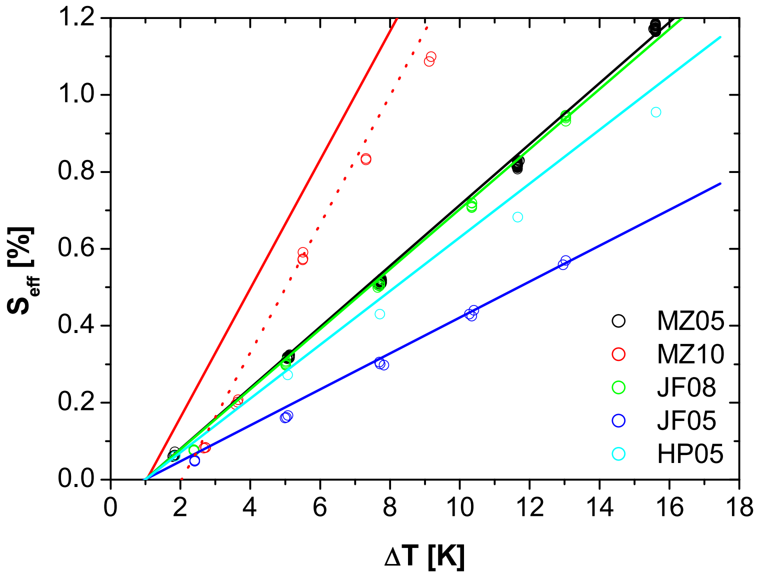

Figure 2.7: Measured and modeled CCNC calibration lines obtained with ammonium sulfate aerosol under different operating conditions as detailed in Tab. 2.2. The circles are the effective supersaturation values calculated from measured dry particle activation diameters, and the lines are the corresponding flow model results (solid lines with ΔT_0=1 K, dotted line with ΔT_0=2 K).

For the MZ10 experiment performed at Q=1.0 L min^{-1}, the modeled S_{eff} values were on average by a factor of ~2 too high when using ΔT_0=1 K, but the relative deviations decreased to ~20 % when a more realistic offset of ΔT_0=2 K was used instead. The strong influence of ΔT_0 severely limits the applicability of the flow model for the extrapolation of experimental calibration results to different operating conditions. As outlined above, ΔT_0 has to be determined empirically and can vary substantially between different CCNC operating conditions, especially at high flow rates and low pressures (see Fig. 2.5d).

2.3.6 Dependence of supersaturation on temperature, pressure, and flow rate

As shown above, the relation between S_{eff} and ΔT depends on T_1, p, and Q. These dependences as observed in calibration experiments at different temperatures, flow rates, and pressures were characterized and compared with the results of CCNC flow model calculations (cf. Sects. 2.2.4 and 2.3.5). To investigate the dependence of S_{eff} on T_1, all calibration lines measured at a flow rate of 0.5 L min^{-1} and ~1000 hPa were used to calculate S_{eff} at ΔT=5 K, which corresponds to an inner-column temperature gradient of ~8 K m^{-1} (subtraction of ΔT_0≈1 K and division of ΔT^*≈4 K by the column length of 0.5 m; cf. Sect. 2.2.4). When plotted against T_1 (Fig. 2.8 a), the experimentally determined S_{eff} values exhibit a near linear decreasing trend with an average slope of $\Delta S_{\text{eff}}/\Delta T_1$=–0.0057% K^{-1}. The observed dependence agrees fairly well with flow model calculations for the same conditions (Q=0.5 L min^{-1}, p=1020 hPa, and ΔT=5 K) yielding a slope of $\Delta S_{\text{eff}}/\Delta T_1$=–0.0048% K^{-1}. Both values are of similar magnitude but somewhat higher than the –0.0034% K^{-1} calculated by Roberts and Nenes (2005) for an inner-column temperature gradient of 8.3 K m^{-1}. Note, however, that the observed variability of S_{eff} at T_1≈299 K was of similar magnitude as the observed and modeled differences between 296 K and 303 K.

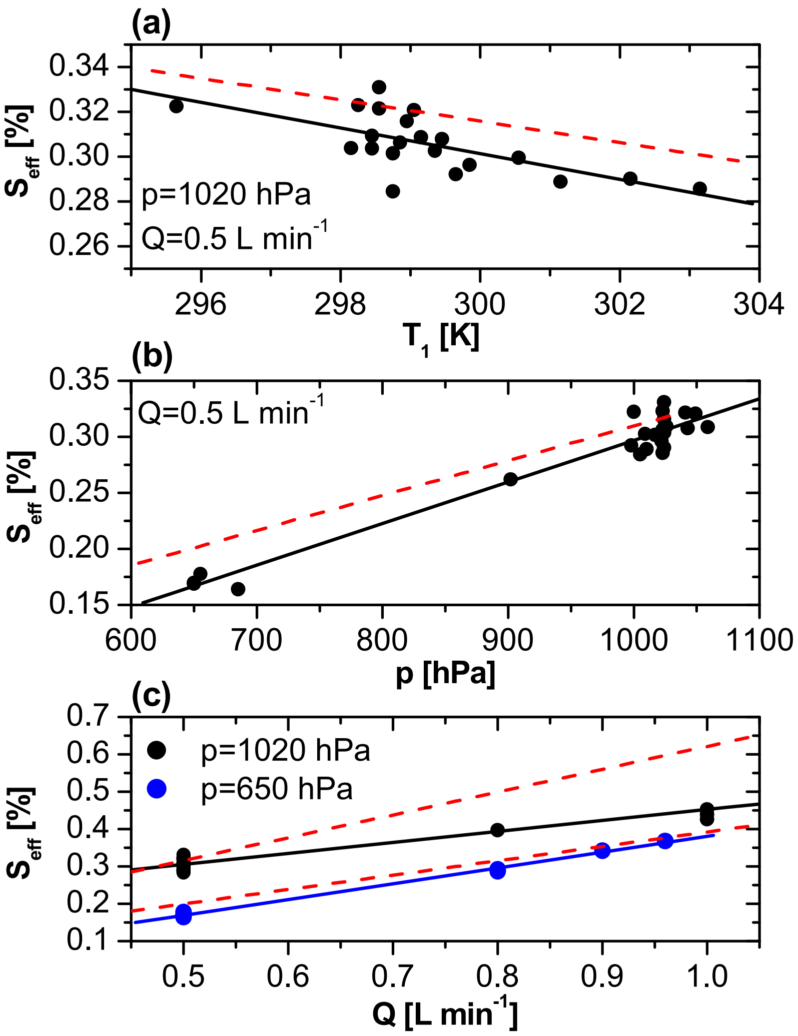

Figure 2.8: Dependence of the effective supersaturation in the CCNC on **(a)** T_1, **(b)** pressure (p), and **(c)** flow rate (Q). The data points are $S_{\rm eff}$ values calculated from all recorded ammonium sulfate calibration lines (cf. Fig. 2.5) at ΔT=5 K. The solid lines are linear fits to the data points and the dashed lines are the $S_{\rm eff}$ values predicted by the CCNC flow model with $R_{\rm T}$=0.24 K W^{-1}.

Figure 2.8 b illustrates the dependence of $S_{\rm eff}$ on pressure. All calibration lines presented in Fig. 2.5 were used to calculate the effective supersaturation at ΔT=5 K, and the obtained values were plotted against pressure. The observed near-linear increase of $S_{\rm eff}$ with p was 0.037% per 100 hPa at Q=0.5 L min^{-1}, which is of similar magnitude as the flow model result (0.031% per 100 hPa) and the value reported by Roberts and Nenes (2005) ($\Delta S_{\rm eff}/\Delta p$=+0.03% per 100 hPa for 0.5 L min^{-1} and 8.3 K m^{-1}).

Figure 2.8c shows the dependence of $S_{\rm eff}$ on the flow rate of the CCNC. All calibration lines measured at ~1020 hPa and ~650 hPa were used to calculate $S_{\rm eff}$ at ΔT=5 K, and the obtained values were plotted against Q. The observed increase of $S_{\rm eff}$ with Q was 0.029% per 0.1 L min^{-1} at sea level, and 0.042% per 0.1 L min^{-1} at high altitude. The model slopes were $\Delta S_{\rm eff}/\Delta Q$=+0.061% per 0.1 L min^{-1} at 1020 hPa and $\Delta S_{\rm eff}/\Delta Q$=+0.038% per 0.1 L min^{-1} at 650 hPa, respectively. The corresponding value reported by Roberts and Nenes (2005) was $\Delta S_{\rm eff}/\Delta Q$=0.06 % per 0.1 L min^{-1} for 1000 hPa and 8.3 K m^{-1}, which is the same as obtained with the CCN flow model, but significantly

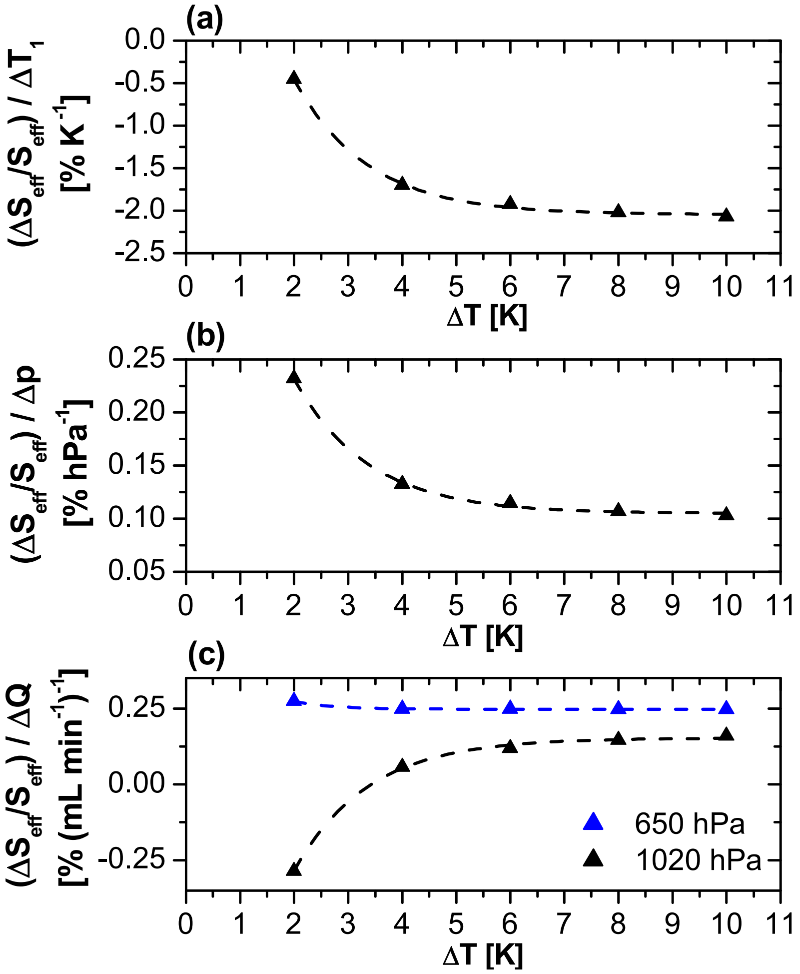

Figure 2.9: Dependence of effective supersaturation on temperature (T_1), pressure (p), and flow rate (Q) in the CCNC averaged over all calibration experiments with ammonium sulfate aerosol. Every data point corresponds to the slope of a linear fit to all values of $\Delta S_\mathrm{eff}/S_\mathrm{eff}$ at a given ΔT plotted against T_1, p, or Q, respectively. $\Delta S_\mathrm{eff}/S_\mathrm{eff}$ is the relative deviation between S_eff from an individual calibration line and the mean value of S_eff for all calibrations performed at Q=0.5 L min^{-1} and $p\approx$1020 hPa (black triangles) or 650 hPa (blue triangles), respectively. The dashed lines are first-order exponential decay fit functions.

higher than what was determined experimentally.

Figure 2.9 illustrates the observed average relative change of supersaturation ($\Delta S_\mathrm{eff}/S_\mathrm{eff}$) caused by changes of column top temperature, pressure, and flow rate as a function of ΔT.

The relative decrease of S_eff with increasing T_1 was ~2% K^{-1} at high ΔT and decayed near-exponentially to ~0.5% K^{-1} at ΔT=2 K (Fig. 2.9 a). The relative increase of S_eff with increasing p was ~1% per 10 hPa at high ΔT and grew near-exponentially to ~2.3% per 10 hPa at ΔT=2 K (Fig. 2.9 b). At high ΔT the relative increase of S_eff with increasing Q was ~15% per 0.1 L min^{-1} for the measurements at $p\approx$1020 hPa and ~25% per 0.1 L min^{-1} at $p\approx$650 hPa (Fig. 2.9c). For the 650 hPa measurements, the deviation increased with decreasing ΔT to up to ~30% per 0.1 L min^{-1} at ΔT=2 K, but for the measurements at ~1020 hPa it decreased to almost –30% per 0.1 L min^{-1} at ΔT=2 K. This divergence confirms that CCN measurements at low ΔT and S_eff, respectively, require careful experimental calibration, and that the possibilities for extrapolation to different operating

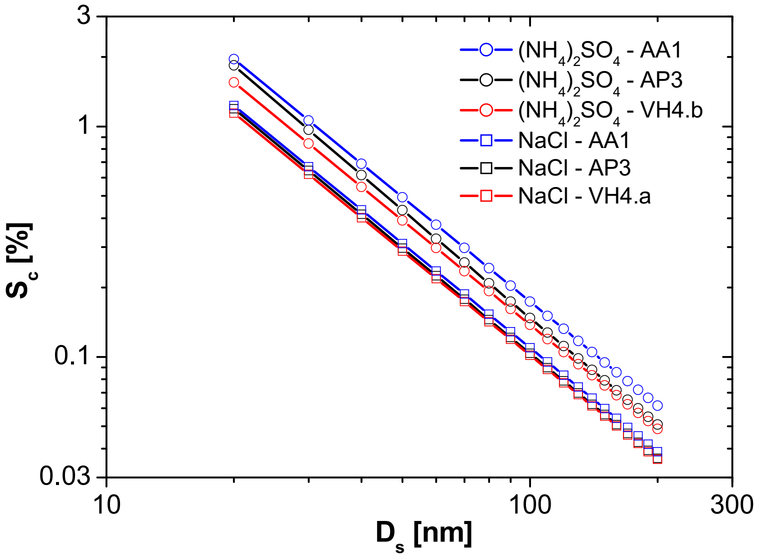

Figure 2.10: Critical supersaturations (S_c) calculated for ammonium sulfate and sodium chloride particles with dry particle mass equivalent diameters (D_s) in the range of 20–200 nm using selected Köhler models from Tab. 2.3 with high (blue), intermediate (black), and low (red) S_c (298.15 K).

conditions are limited.

2.3.7 Deviations between different Köhler models

To characterize the influence of different Köhler modeling approaches on the CCNC calibration and measurement data analysis, critical supersaturations (S_c) have been calculated for ammonium sulfate and sodium chloride particles in the size range of 20–200 nm with a range of Köhler models and parameterizations/approximations of aqueous solution properties that are frequently used in CCN studies.

According to different mathematical formalisms, which are mostly determined by the underlying representation of water activity, it is distinguished between activity parameterization (AP), osmotic coefficient (OS), van't Hoff factor (VH), effective hygroscopicity parameter (EH), and analytical approximation (AA) models. Detailed information about the used Köhler models can be found in Appendix B. An overview of the tested models and parameterizations is given in Tab. 2.3, and the results are summarized in Figs. 2.10 and 2.11.

2.3.7.1 Effects of solution density and surface tension

For the CCN activation of the salt particles investigated in this study, different parameterizations and approximations of aqueous solution density (ρ_sol) and surface tension (σ_sol) had only a small influence on the critical supersaturation.

In the AP3 model for ammonium sulfate, S_c decreased by less than 0.3 % (relative) when volume additivity was assumed to calculate ρ_sol (AP3.a) instead of using the experimental parameterization of Tang and Munkelwitz (1994). Using the density of pure water to approximate ρ_sol (AP3.b) lowered the supersaturation by up to $\sim$1 % (relative). Approximating σ_sol by a temperature-dependent parameterization for pure water (AP3.c) or by a constant value of 0.072 N m^{-1} (AP3.d) reduced S_c

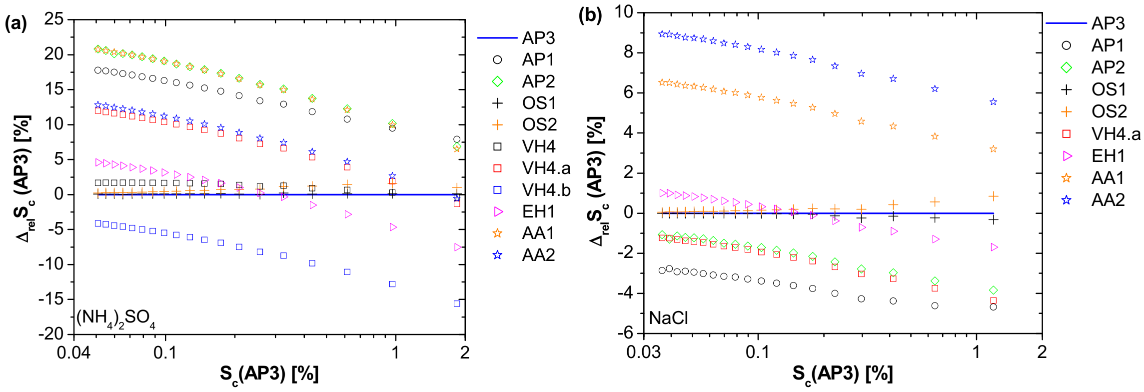

Figure 2.11: Deviations of S_c values calculated with different Köhler models as listed in Tab. 2.3 relative to the AP3 model for **(a)** ammonium sulfate and **(b)** sodium chloride (298.15 K).

by up to 1.3 % or 1.8 % (relative), respectively.

The influence of ρ_{sol} and σ_{sol} on S_c was most pronounced for small particle diameters (high solute molalities). For large particles, the approximations of ρ_{sol} and σ_{sol} had no significant influence on S_c. Similar results were obtained when using different parameterizations of solution density and surface tension in other types of Köhler models (OS, VH, EH) for ammonium sulfate.

For sodium chloride, the relative deviations in S_c caused by different parameterizations of solution density and surface tension were even smaller than for ammonium sulfate. The maximum deviations relative to AP3 were –0.1 % for AP3.a, –0.4 % for AP3.b, –0.6 % for AP3.c, and –1 % for AP3.d.

Overall, the model deviations caused by different parameterizations and approximations for solution density and surface tension were smaller than the characteristic statistical uncertainties of field measurements (±5–7 %). Nevertheless, they can exceed the statistical uncertainty of laboratory experiments (±1 %, see Tab. 2.4) and should not be neglected in studies aiming at high accuracy.

2.3.7.2 Effects of water activity representation

According to Clegg and Wexler (2007), the uncertainty of water activity calculations with the Aerosol Inorganics Model (AIM, http://www.aim.env.uea.ac.uk/aim/aim.html; Clegg et al., 1998a,b) for dilute aqueous solutions of ammonium sulfate and sodium chloride is only 10^{-6}–10^{-5}, and the AIM can be regarded as an accurate reference for the parameterization of water activity in Köhler model calculations.

Figure 2.11 a shows the relative deviations of S_c for ammonium sulfate particles calculated with different Köhler models relative to the AIM-based activity parameterization model AP3.

As expected, the results of the osmotic coefficient model OS1 were nearly identical to AP3 (relative deviations <0.2 %), because both models are based on similar ion-interaction approaches. The results of the OS2 model, which is based on a simplified ion-interaction approach, were also near-identical at low S_c but deviated by up to +3 % at high S_c, i.e., for small particles and high solute molality in the droplet with the critical wet particle diameter ($D_s \approx 20$ nm, $\mu_s \approx 0.3$ mol kg^{-1}, $D_{\text{wet,c}} \approx 75$ nm).

The results of the van't Hoff factor model VH4 were nearly identical to AP3 at high S_c, but ~2 % higher at low S_c, i.e., for large particles and low solute molality in the droplet with the critical wet

Table 2.3: Overview of the Köhler models described in Appendix B and compared in Sects. 2.3.7 and 2.3.8 (AS=ammonium sulfate; SC=sodium chloride).

model	Köhler equation	solution density	surface tension	water activity representation
Activity parameterization (AP) models				
AP1	Eq. (B.14)	Eq. (B.9)	Eq. (B.12)	Eq. (B.7)[a,b]
AP2	Eq. (B.14)	Eq. (B.10)	Eq. (B.12)	Eq. (B.8)[c]
AP3	Eq. (B.14)	Eq. (B.9)	Eq. (B.12)	AIM[d]
AP3.a	Eq. (B.14)	Eq. (B.10)	Eq. (B.12)	AIM[d]
AP3.b	Eq. (B.14)	ρ_w	Eq. (B.12)	AIM[d]
AP3.c	Eq. (B.14)	Eq. (B.9)	σ_w	AIM[d]
AP3.d	Eq. (B.14)	Eq. (B.9)	0.072 N m^{-1}	AIM[d]
Osmotic coefficient (OS) models				
OS1	Eq. (B.14)	Eq. (B.9)	Eq. (B.12)	Eq. (B.15),(B.16)[e]
OS2	Eq. (B.14)	Eq. (B.9)	Eq. (B.12)	Eq. (B.15),(B.17)[f]
Van't Hoff factor (VH) models				
VH1	Eq. (B.14)	Eq. (B.9)	Eq. (B.12)	Eqs. (B.18), (B.25)[g], (B.26)[h]
VH2	Eq. (B.20)	Eq. (B.9)	Eq. (B.12)	Eqs. (B.25)[g], (B.26)[h]
VH3	Eq. (B.21)	Eq. (B.9)	Eq. (B.12)	Eqs. (B.25)[g], (B.26)[h]
VH4	Eq. (B.22)	ρ_w	σ_w	Eqs. (B.25)[g], (B.26)[h]
VH4.a	Eq. (B.22)	ρ_w	σ_w	AS: i_s=2.2, SC: i_s=2
VH4.b	Eq. (B.22)	ρ_w	σ_w	AS: i_s=3
Effective hygrosocopicity parameter (EH) model				
EH1	Eq. (B.30)	Eq. (B.9)	Eq. (B.12)	AS: κ=0.61[i], SC: κ=1.28[i]
Analytical approximation (AA) models				
AA1	Eq. (B.31)	ρ_w	σ_w	AS: i_s=2.2, SC: i_s=2
AA1.a	Eq. (B.31)	ρ_w	σ_w	AS: i_s=3
AA2	Eq. (B.32)	ρ_w	σ_w	AS: κ=0.61[i], SC: κ=1.28[i]

[a] Tang and Munkelwitz (1994), [b] Tang (1996), [c] Kreidenweis et al. (2005), [d] Clegg et al. (1998a,b), [e] Pitzer and Mayorga (1973), [f] Brechtel and Kreidenweis (2000), [g] Low (1969), [h] Young and Warren (1992), [i] Petters and Kreidenweis (2007)

particle diameter (D_s=200 nm, $\mu_\mathrm{s}\approx 0.006\,\mathrm{mol\,kg^{-1}}$, $D_\mathrm{wet,c}\approx 2.7\,\mu\mathrm{m}$).

The results of VH1 and VH2 were near-identical to VH4 (rel. dev. <1 %), but VH3 was about 2.5 % higher at high S_c (not shown in Fig. 2.11). This deviation of VH3 is due to the simplifying assumption that the contribution of the solute to the total mass of the droplet is negligibly small, which is not really the case for small D_s and $D_\mathrm{wet,c}$. This simplifying assumption is also made in VH4, but there it is compensated by approximating the density of the ammonium sulfate solution with the density of water.

The results of the VH4.a model assuming a constant van't Hoff factor i_s=2.2 were similar to AP3 at high S_c, but they deviated by up to +12 % at low S_c. Model VH4.b assuming i_s=3 deviated by –4 % at low S_c and by –16 % at high S_c.

The effective hygroscopicity parameter model (EH) deviated from AP3 by +5 % at low S_c and by –8 % at high S_c. Note that the constant κ-value of 0.61 assumed in EH1 is equivalent to a constant van't Hoff factor of 2.52.

The water activity parameterization models AP1 and AP2 yielded much higher S_c values than AP3. The relative deviations ranged from +18 % and +21 %, respectively, at low S_c to +8 % at high S_c.

The analytical approximation model (AA) with i_s=2.2 (AA1) was nearly identical to the AP2 model, deviating by +7 % to +21 % from AP3. The deviations of AA1.a with i_s=3 were smaller but still substantial (–9 % to +4 % relative from AP3).

Overall, only the models OS1, OS2 and VH1 to VH4 exhibited deviations from AP3 that were smaller than the statistical measurement uncertainty ($\sim$2 %, Tab. 2.4), and the deviations of the EH1 model were of similar magnitude as the variability of calibrations in field measurement campaigns (up to $\sim$10 %, Tab. 2.4).

Figure 2.11 b shows the relative deviations of S_c for sodium chloride particles calculated with different Köhler models relative to the AIM-based activity parameterization model AP3.

Again, the results of the osmotic coefficient model OS1 were nearly identical to AP3 (relative deviations <0.3 %), and the OS2 model exhibited substantial deviations only at high S_c (up to +1 % relative). The deviations of the EH1 model did also not exceed the statistical measurement uncertainty of $\sim$2 %. The relative deviations of the other tested models ranged from –5 % for AP1 at high S_c to +7 % for AA1 at low S_c, which is still less pronounced than the deviations found for AS (–16 % to +21 % rel.).

In any case, the model deviations caused by different parameterizations and approximations of water activity were much larger than the deviations related to solution density and surface tension. Test calculations with the AP3 model showed that deviations of water activity by 10^{-5} (10^{-4}) correspond to relative changes of critical supersaturation on the order of 0.06–2 % (0.6–20 %) for the investigated dry particle diameter range of 20–200 nm (largest deviations at large D_s and $D_\mathrm{wet,c}$ corresponding to low μ_s).

Provided that the relative uncertainty of water activities calculated with the AIM is indeed as low as 10^{-6}–10^{-5}, only Köhler models that are based on the AIM (such as AP3) or that yield very similar results (such as OS1, OS2, VH4) should be used for CCNC calibration and other investigations involving the CCN activation of $(\mathrm{NH_4})_2\mathrm{SO_4}$ and NaCl.

2.3.7.3 Temperature effects

To test the influence of temperature, S_c was calculated for ammonium sulfate particles with the AP3 model not only at 298.15 K but also at 303.15 K (and 308.15 K). The temperature change had hardly any influence on the AIM-based parameterization of water activity (rel. change of $a_\mathrm{w}<10^{-5}$), but the Kelvin term and S_c changed by about –4 % (relative) for all investigated particle sizes (–8 % at 308.15 K). Similar results were obtained with the other Köhler models.

The effect of temperature on Köhler model calculations of S_c (relative change approx. –1 % K^{-1}) is of similar magnitude as the experimentally observed and CCNC flow model-derived dependences of S_eff on T_1 (–0.5% to –2% K^{-1}; Sect. 2.3.6, Figs. 2.8 a and 2.9 a).

Clearly, the temperature is one of the most important influencing factors not only for the experimental performance of the CCNC (reproducibility of CCN efficiency spectra), but also for the Köhler model calculations used to convert the measured activation diameters into effective water vapor supersaturations.

As outlined in Sect. 2.2.1, CCN activation is assumed to occur in the first half of the CCNC flow column, where the column temperature increases from T_1 to T_2 ($T_2{\approx}T_1{+}\Delta T/2$). Neither the instrument manual nor Roberts and Nenes (2005) or Lance et al. (2006), however, have specified explicitly which temperature should be regarded as the effective temperature to be inserted in Köhler model calculations for instrument calibration. In this study T_1 was taken, which represents a lower limit for the effective temperature in the CCNC column.

According to the instrument's operating principles, the actual temperature increase along the centerline of the aerosol flow is smaller than the increase of column temperature. Nevertheless, $\Delta T/2$ can be regarded as an upper limit for deviations of the effective temperature in the CCNC from T_1. In this study the maximum values of ΔT and $\Delta T/2$ were 17 K and 8.5 K, respectively, which corresponds to a maximum relative deviation (bias) of S_eff by about –7 %. In practice and at lower ΔT, the deviations should be smaller.

2.3.8 CCN activation of ammonium sulfate and sodium chloride particles: consistency of experimental results and model calculations

To test the consistency of experimental results and model calculations for the CCN activation of different substances, calibration experiments have been performed with $(\mathrm{NH_4})_2\mathrm{SO_4}$ and with NaCl under near-identical laboratory conditions. Exemplary calibration lines (S_eff vs. ΔT) obtained with the different aerosols and with different Köhler models are shown in Fig. 2.12.

The $(\mathrm{NH_4})_2\mathrm{SO_4}$ and NaCl calibration lines obtained with the AP3 model ($(\mathrm{NH_4})_2\mathrm{SO_4}$-AP3, NaCl-AP3) and with models yielding similar results for both salts (OS1, OS2, VH4) were in good agreement when no shape correction was applied to the measured NaCl activation diameters (Fig. 2.12 a; relative deviations 1–3 % at $S_\mathrm{eff}>0.3$ %).

If, however, a dynamic shape factor of 1.08, which is widely used to account for cubic shape of NaCl particles (e.g., Krämer et al., 2000; Gysel et al., 2002; Mikhailov et al., 2004), was applied to correct the measured NaCl activation diameters, the S_eff values of NaCl-AP3 were 7–23 % (relative) higher than those of $(\mathrm{NH_4})_2\mathrm{SO_4}$-AP3 (Fig. 2.12 b).

When the shape factors proposed by Biskos et al. (2006a,b) were applied (1.02 for $(\mathrm{NH_4})_2\mathrm{SO_4}$,

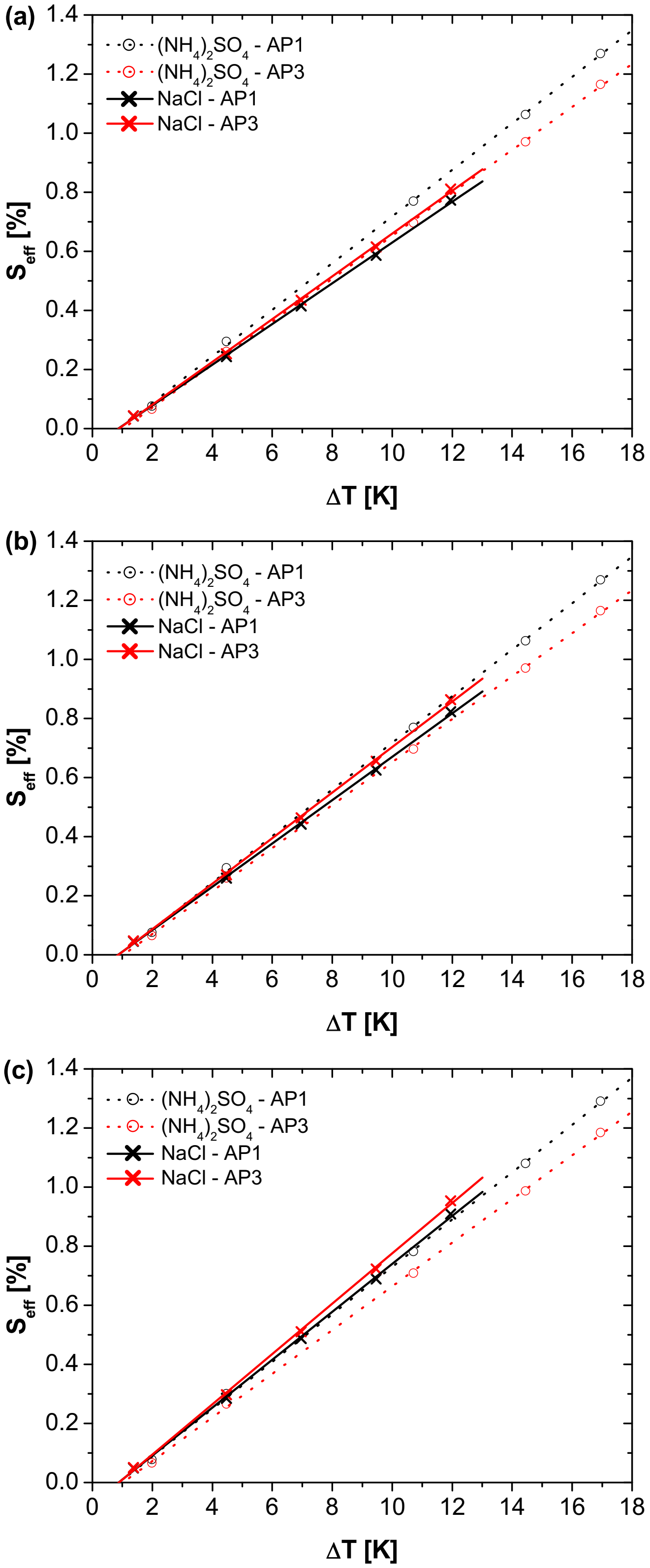

Figure 2.12: Calibration lines of effective supersaturation (S_eff) vs. temperature difference (ΔT) obtained from experiments with ammonium sulfate and sodium chloride particles under equal conditions (Q=(0.5±0.001) L min^{-1}, p=(999±6) hPa, T_1=(299.6±0.05) K): **(a)** without particle shape correction (χ=1.0), **(b)** with χ=1.0 for $(NH_4)_2SO_4$ and χ=1.08 for NaCl, and **(c)** with χ=1.02 for $(NH_4)_2SO_4$ and size dependent χ for NaCl (Biskos et al., 2006a,b). The data points were calculated from measured dry particle activation diameters using different Köhler models (AP1, AP3; Tab. 2.3); the lines are linear fits.

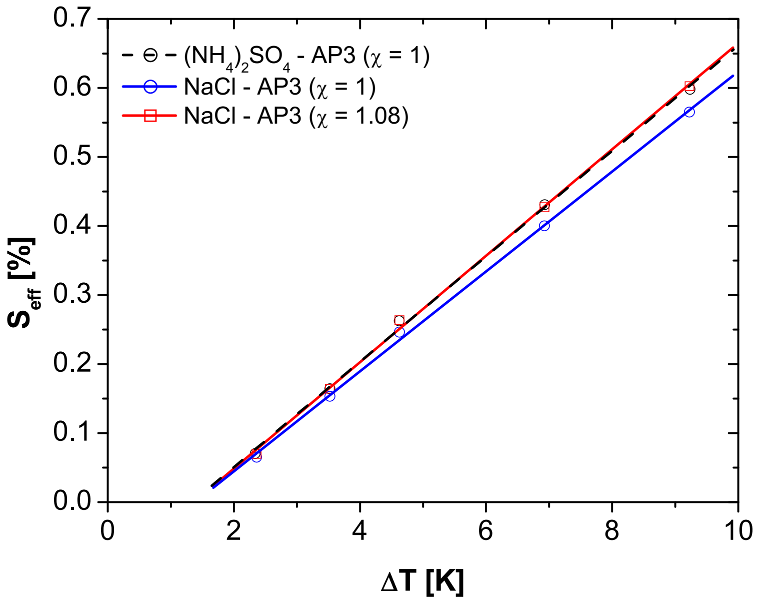

Figure 2.13: Calibration lines of effective supersaturation (S_{eff}) vs. temperature difference (ΔT) obtained from experiments with ammonium sulfate and sodium chloride particles under equal conditions (Q=(0.5±0.001) L min^{-1}, p=(998±3) hPa, T_1=(297.9±0.5) K). In these experiments the particles were generated with an alternative method (diffusion drying instead mixing with dry air). The data points were calculated from measured dry particle activation diameters using different Köhler models; the lines are linear fits.

size-dependent factor between 1.08 and 1.24 for NaCl), the S_{eff} values of NaCl-AP3 were 17–30 % higher than those of $(\mathrm{NH_4})_2\mathrm{SO_4}$-AP3 (Fig. 2.12c). In this case, however, the $(\mathrm{NH_4})_2\mathrm{SO_4}$ and NaCl calibration lines obtained with the AP1 model were in good agreement (relative deviations $\sim$2 % at S_{eff}>0.15 %). Similar results were obtained with AP2.

The changes of S_{eff} caused by NaCl particle shape correction (6–18 %) clearly exceeded the statistical measurement uncertainties of 1–2 %. They indicate that the shape and microstructure of calibration aerosol particles can strongly influence the calibration of a CCNC.

Under the assumption that the AIM-based Köhler model AP3 can be regarded as accurate and that there is no artificial bias between the calibration experiments with $(\mathrm{NH_4})_2\mathrm{SO_4}$ and with NaCl, the above results indicate that both the $(\mathrm{NH_4})_2\mathrm{SO_4}$ and NaCl particles were more or less compact spheres ($\chi\approx1$) or had at least very similar dynamic shape factors. Alternatively, the results would indicate an inconsistency between the AIM-based water activity parameterizations for $(\mathrm{NH_4})_2\mathrm{SO_4}$ and NaCl.

These results support the consistency of the AIM-based water activity parameterizations for dilute aqueous solutions of $(\mathrm{NH_4})_2\mathrm{SO_4}$ and NaCl, and they indicate inconsistencies between the widely used parameterizations applied in the Köhler models AP1 and AP2, which are based on the extrapolation of electrodynamic balance (EDB) and hygroscopicity tandem differential mobility analyzer (HT-DMA) measurement data (Tang, 1996; Tang and Munkelwitz, 1994; Kreidenweis et al., 2005). In any case, they demonstrate that the conditions of particle generation and the shape and microstructure of NaCl particles are critical for their application in CCN activation and CCNC calibration experiments. Further systematic investigations of the dependence of NaCl aerosol particle shape and microstructure on particle generation and conditioning are under way and will be presented and discussed in detail elsewhere.

Usually, NaCl aerosol particles generated by nebulization of an aqueous solution are assumed to be of near-cubic shape. Earlier investigations based on HTDMA experiments and electron microscopy, however, had already shown that the shape and microstructure of NaCl particles depend strongly on the drying conditions and relative humidity to which they are exposed (Mikhailov et al., 2004). NaCl particles generated by nebulization were found to be near-spherical after conditioning at relative humidities close to but below the deliquescence threshold ($\sim$75 % RH).

Additional test experiments have been performed in which the conditions of aerosol generation were systematically varied. As described in Sect. 2.2.2, the salt particles for all calibration experiments reported above had been generated by the mixing of nebulized salt solution droplets with an excess of dry air (rapid quenching to $<$15 % RH). In the additional test experiments, the nebulized salt solution droplets were instead dried with a silica gel diffusion drier (gradual drying to $<$5 % RH). Under these conditions, the S_{eff} values obtained from the NaCl activation diameters with the NaCl-AP3 model were 6–7 % lower than those obtained from the $\mathrm{(NH_4)_2SO_4}$ activation diameters with the $\mathrm{(NH_4)_2SO_4}$-AP3 model. After correction of the NaCl activation diameters with a shape factor of 1.08, however, the $\mathrm{(NH_4)_2SO_4}$ and NaCl calibration lines obtained with the AP3 model were in good agreement (Fig. 2.13; relative deviations $<$1 % at $S_{\mathrm{eff}}>$0.1 %).

2.3.9 Comparison with other CCN and hygroscopicity instruments

Four CCN instruments were used to measure the critical supersaturation of size-selected particles prepared at the Leipzig Aerosol Cloud Interaction Simulator (LACIS) facility during the LExNo laboratory measurement campaign (14 November to 2 December 2005; Stratmann et al., 2010). In addition to the DMT-CCNC used in this PhD work, two Wyoming static diffusion CCN counters and the continuous flow LACIS instrument were included. Moreover, a high humidity tandem differential mobility analyzer (HH-TDMA) was used to measure the hygroscopic growth factor at 98% relative humidity (Snider et al., 2010). The tested aerosols were composed of ammonium sulfate, levoglucosan, levoglucosan and soot, and ammonium hydrogen sulfate and soot, which were synthesized to mimic the particles of an atmospheric aerosol originating from biomass combustion. The comparison of critical supersaturations for droplet activation measured with the four different CCN instruments showed an excellent agreement within the measurement uncertainty. This is remarkable considering that the instruments are based on different designs and operating principles. Such a successful, comprehensive inter-comparison of CCN instruments under controlled conditions was not reported in the literature before.

The relationship between hygroscopicity and CCN-activation was described via two slightly different one-parameter approaches, which avoid unknown properties in Köhler theory (e.g., density, molar mass of mixture). The resulting closure was also excellent for all particle types. This suggests the validity of the same theory for both processes and allows for predicting the critical supersaturation of coated soot particles based on hygroscopic growth measurements.

More information on the performance and results of these experiments can be found in Henning et al. (2010); Snider et al. (2010); Stratmann et al. (2010); Wex et al. (2008) and references therein.

Table 2.4: Overview of characteristic calibration and measurement uncertainties affecting the effective supersaturation in the CCNC (for S_{eff}>0.1 %): statistical uncertainties are characterized by observed relative standard deviations (preceded by "±"); systematic errors are characterized by observed/calculated maximum relative deviations (preceded by a sign indicating the direction of bias, if known).

source of uncertainty/bias	characteristic relative deviation of S_{eff} (%)
measurement precision in single experiment (hours)	±1
variability of conditions in single field campaign (weeks)	±5
long-term changes of instrument properties (months)	–10
CCNC flow model extrapolations (T_1, p)	10
doubly charged particles	+3
DMA transfer function	<1
effective temperature of CCN activation (T_1, T_2)	–5
solution density approximation	–1
surface tension approximation	–2
water activity representation for $(NH_4)_2SO_4$	–16 to +21
water activity representation for NaCl	–5 to +7
particle shape correction for NaCl	up to –15

2.4 Conclusions

Table 2.4 summarizes the CCNC calibration and measurement uncertainties determined in this study. Under stable operating conditions, the effective water vapor supersaturation (S_{eff}) in the DMT-CCNC can be adjusted with high precision. The relative standard deviations of repeated measurements in laboratory experiments were as low as ±1 % for S_{eff}>0.1 %. During field measurements, however, the relative variability increased to about ±5 %, which is mostly due to variations of the CCNC column top temperature (T_1) with ambient temperature.

According to the instrument operating principles, S_{eff} is controlled not only by the temperature difference between the top and bottom of the flow column (ΔT), but also by the absolute temperature, pressure (p), and aerosol flow rate (Q). The observed dependence can be described by the following gradients: (ΔS_{eff} /S_{eff})/ΔT_1 ≈–2 % K^{-1} at p≈1020 hPa and Q=0.5 L min^{-1}; (ΔS_{eff} /S_{eff})/Δp≈+0.1 % hPa^{-1} at Q=0.5 L min^{-1} and T_1≈299 K; and (ΔS_{eff} /S_{eff})/ΔQ≈+0.15 % (mL $\mathrm{min}^{-1})^{-1}$ at p≈1020 hPa and T_1≈299 K.

At high supersaturations (S_{eff}>0.1 %), the experimental data points agreed well with a linear calibration function of S_{eff} vs. ΔT (relative deviations ≤3 %). At S_{eff}<0.1 %, however, the calibration line deviated by up to ~40 % from experimental data points, indicating that in this range S_{eff} does not linearly depend on ΔT and special care has to be taken to obtain reliable measurements. Besides careful calibration, it may be beneficial to operate the CCNC at particularly low flow rates

(<0.5 L min^{-1}) to achieve high precision at low S_{eff}.

After the subtraction of a constant temperature offset and the derivation of an instrument-specific thermal resistance parameter (R_T≈0.24 K W^{-1}), the experimental calibration results could be fairly well reproduced by the CCNC flow model of Lance et al. (2006). At $S_{\mathrm{eff}}>0.1$ % the relative deviations between flow model and experimental results were mostly less than 10 %. At $S_{\mathrm{eff}}\leq 0.1$ %, however, the deviations exceeded 40 %, which can be attributed to non-idealities which also cause the near-constant temperature offset. Therefore, it is suggested that the CCNC flow model can be used for extrapolating the results of experimental calibrations to different operating conditions, but should generally be complemented by calibration experiments performed under the relevant conditions – especially at low S_{eff}.

In the course of several field and laboratory measurement campaigns extending over a period of about one year, a systematic decrease of the slope of the calibration line by about 10 % was found, which could not be reversed by standard cleaning procedures and may require a full refurbishing of the instrument to be reversed. In any case, it is recommended to perform careful and repeated calibration experiments during every field campaign to ensure reliable operation and to obtain representative uncertainty estimates for the CCN measurement data.

Besides experimental variabilities, Tab. 2.4 also summarizes calibration and measurement uncertainties related to data analysis and Köhler model calculations.

If the influence of doubly charged particles is not taken into account in the fitting of CCN efficiency spectra, the dry particle activation diameter can be underestimated, and the effective supersaturation can be overestimated by up to ∼3 %. The transfer function of the differential mobility analyzer used to generate monodisperse calibration aerosols affected S_{eff} by less than 1 % (relative). Moreover, the effective temperature of CCN activation in the instrument may be higher than the column top temperature (T_1), which was used for Köhler model calculations. This can lead to a bias in S_{eff} of up to about –5 %. Note that the above percentages refer to the range of operating conditions tested in this study; the uncertainties may change under different experimental conditions.

Different ways of calculating or approximating solution density and surface tension in the Köhler models can lead to relative underestimations of S_{eff} which are small (up to –1 % and –2 %, respectively), but not negligible with regard to measurement precision under stable operating conditions.

Large deviations were caused by the different parameterizations for the activity of water in dilute aqueous solutions of the two salts (Appendix B), with water activity differences on the order of $\sim 10^{-4}$ corresponding to supersaturation differences on the order of ∼10 % (relative). For the relevant range of water vapor supersaturation (0.05–2 %) and solute molality (∼0.003–0.3 mol kg^{-1}), the relative deviations from a reference model based on the Aerosol Inorganics Model (AIM) were in the range of –16 % to +21 % for $(\mathrm{NH_4})_2\mathrm{SO_4}$ and –5 % to +9 % for NaCl.

Provided that the AIM can be regarded as an accurate source of water activity data for highly dilute solutions of $(\mathrm{NH_4})_2\mathrm{SO_4}$ and NaCl, only Köhler models that are based on the AIM or yield similar results should be used in CCN studies involving these salts and aiming at high accuracy (Tab. 2.3). Concentration-dependent osmotic coefficient models (OS1, OS2) and van't Hoff factor models (VH1–VH4) were found to agree well with the AIM-based model (AP3); models based on widely used water activity parameterizations derived from electrodynamic balance and hygroscopicity tandem differential mobility analyzer measurement data (AP1, AP2), however, deviated strongly.

Concentration-independent van't Hoff factor models (VH4.a, VH4.b), effective hygroscopicity parameter models (EH1), and analytical approximation models (AA1, AA2) generally exhibited a trend from positive deviations at low S_{eff} to negative deviations at high S_{eff} (Fig.2.11).

In any case, it is suggested that CCN studies should always report exactly which Köhler model equations and parameters were used, in order to ensure that the results can be properly compared.

Experiments with $(\mathrm{NH_4})_2\mathrm{SO_4}$ and NaCl aerosols showed that the conditions of particle generation and the shape and microstructure of NaCl particles are critical for their application in CCN activation and CCNC calibration experiments (relative deviations up to 18 %). The measurement and model results indicate that NaCl particles generated by nebulization of an aqueous salt solution can change from near-spherical to cubic shape, depending on the drying processes.

The comparison with other CCN instruments confirmed the high accuracy and precision of the instrument and the measurement procedures developed and applied in this thesis. Laboratory experiments with test aerosols of complex chemical composition confirmed the consistency of observations and multicomponent Köhler modeling.

3 CCN in polluted air and biomass burning smoke near the mega-city Guangzhou, China[2]

3.1 Introduction

In order to incorporate the effects of CCN in meteorological models at all scales, from large eddy simulation (LES) to global climate models (GCM), knowledge of the spatial and temporal distribution of CCN in the atmosphere is essential (Huang et al., 2007). In recent years, anthropogenic emissions of aerosol particles and precursors from Asia have increased significantly (Streets et al., 2000, 2008; Richter et al., 2005; Shao et al., 2006), and numerous studies indicate that anthropogenic aerosol particles have changed cloud microphysical and radiative properties (Xu, 2001; Liu et al., 2004; Massie et al., 2004; Zhang et al., 2004; Wang et al., 2005; Qian et al., 2006; Zhao et al., 2006; Li et al., 2007; Rosenfeld et al., 2007; Deng et al., 2008). Thus, CCN data are required for assessing the impact of anthropogenic aerosol on regional and global climate. Several earlier and recent studies have reported CCN measurements from various regions around the world (e.g. Andreae, 2009; Andreae and Rosenfeld, 2008; Bougiatioti et al., 2009; Broekhuizen et al., 2006; Chang et al., 2010; Dusek et al., 2006, 2010; Ervens et al., 2010; Gunthe et al., 2009; Lance et al., 2009; Pöschl et al., 2009; Roberts et al., 2001, 2002, 2006; Shantz et al., 2010; Wang et al., 2008, and references therein). However, only few CCN measurements have been performed in Asia and in the vicinity of mega-cities and city-clusters, which are major source regions of air particulate matter (e.g. Matsumoto et al., 1997; Yum et al., 2005, 2007; Kuwata et al., 2007, 2008, 2009; Wiedensohler et al., 2009).

The Pearl River Delta (PRD) in southeastern China is one of the main centers of economic activity and growth in Asia. Due to strong anthropogenic emissions, the PRD region is often plagued with high aerosol concentrations that not only lead to low visibility, but can also impact the regional radiative balance, precipitation patterns and hydrological cycles (Hagler et al., 2006; Andreae et al., 2008; Fan et al., 2008; Wendisch et al., 2008; Zhang et al., 2008).

Within the "Program of Regional Integrated Experiments of Air Quality over the Pearl River Delta" intensive campaign in July 2006 (PRIDE-PRD2006), the CCN properties of aerosol particles in polluted air and biomass burning smoke near the mega-city Guangzhou were measured and characterized as a function of particle diameter (20–290 nm) and water vapor supersaturation (0.068–1.27%). This chapter focuses on the results of the size-resolved CCN measurements, on the implications for different approaches of approximating and predicting CCN number concentrations, and on the relationships between aerosol chemical composition and CCN activity.

3.2 Methods

3.2.1 Measurement location, meteorological conditions and supporting data

The measurements were performed during the period of 1–30 July 2006 in Backgarden (23.548056° N, 113.066389° E), a small village ~60 km northwest of Guangzhou on the outskirts of the densely pop-

---

[2] This chapter is partly based on the manuscript "Cloud condensation nuclei in polluted air and biomass burning smoke near the mega-city Guangzhou, China – Part 1: Size-resolved measurements and implications for the modeling of aerosol particle hygroscopicity and CCN activity" by D. Rose, A. Nowak, P. Achtert, A. Wiedensohler, M. Hu, M. Shao, Y. Zhang, M. O. Andreae, and U. Pöschl, published in Atmos. Chem. Phys. (Rose et al., 2010a).

ulated center of the PRD. Due to the prevailing southeast monsoon circulation at this time of year, the air masses came mainly from the south/southeast, making this site a rural receptor site for the regional pollution resulting from the outflow of the city cluster around Guangzhou. The average meteorological conditions (arithmetic mean ± standard deviation) for the campaign were: 28.9±3.2 °C ambient temperature, 78.0±13.7% ambient Relative Humidity (RH), 997±4 hPa ambient pressure, 1.8±1.2 $\mathrm{m\,s^{-1}}$ local wind speed, 143±53° local wind direction. For more information about the measurement location and meteorological conditions see Garland et al. (2008).

A two-story building was used exclusively to house the measurement campaign, with most of the instruments placed in air conditioned rooms on the top floor and sample inlets mounted on the rooftop. The main aerosol inlet used in this study was equipped with a Rupprecht and Patashnick $\mathrm{PM_{10}}$ inlet (flow rate 16.7 $\mathrm{L\,min^{-1}}$). The sample flow passed through stainless steel tubing (1.9 cm i.d., 5.1 m length) and a diffusion dryer with silica gel/molecular sieve cartridges (alternating regeneration with dry pressurized air, regeneration cycles 15–50 min, average RH=33±7%). After drying, the sample flow was split into separate lines. One led to the CCN measurement setup described below (0.9 cm i.d. stainless steel, ∼4 m length, flow rate 1.5 $\mathrm{L\,min^{-1}}$), one to the setup measuring aerosol optical properties, and another one was used for aerosol particle size distribution measurements (3–900 nm) with a Twin Differential Mobility Particle Sizer (TDMPS), and volatility measurements with a Volatility Tandem Differential Mobility Analyzer (VTDMA). The inlet, dryer, size distribution measurements, and volatility measurements were operated by the Leibniz Institute for Tropospheric Research (IfT).

The aerosol mass spectrometry (AMS) measurements employed in this study were performed using a separate aerosol inlet system. The sample air for the AMS was aspirated from the rooftop of the building using a stainless steel tube of ∼6 m with an inner diameter of 10.0 mm. A $\mathrm{PM_{2.5}}$ cyclone (flow rate 10 $\mathrm{L\,min^{-1}}$; URG Corp., USA) was used for the inlet to remove coarse particles, although the actual size-cut of the AMS is determined by the more restrictive transmission characteristics of its aerodynamic lens (approximately $\mathrm{PM_1}$). The 10.0 mm tube was reduced to a tube with an i.d. of 4.4 mm and subsequently to a tube with an i.d. of 2.0 mm (∼0.49 m length) using two isokinetic manifolds in order to match the AMS sample flow and orifice assembly. The temperature of the tube and the AMS orifice was controlled at a constant value (40 °C or 42 °C, depending on ambient dew point) in order to dry the particles in the sample air. The relative humidity in the sample air was calculated to be within the range of 30–45% for the entire period of the campaign.

3.2.2 CCN measurement and data analysis

3.2.2.1 Instrumentation and measurement procedure

Size-resolved CCN efficiency spectra (CCN activation curves) were measured with a Droplet Measurement Technologies continuous-flow CCN counter (DMT-CCNC Roberts and Nenes, 2005; Lance et al., 2006) coupled to a Differential Mobility Analyzer (DMA; TSI 3071) and a condensation particle counter (CPC; TSI 3762; Frank et al., 2006; Rose et al., 2008).

The CCN Counter (CCNC) was operated at a total flow rate of 0.5 $\mathrm{L\,min^{-1}}$ with a sheath-to-aerosol flow ratio of 10. For the campaign, the average sampling temperature and pressure as measured by the CCNC sensors were (23.7±1.4) °C and (1006±6) hPa (posititve deviation from ambient

Table 3.1: Characteristic parameters from the 5 calibration experiments performed during the campaign (arithmetic mean ± standard deviation). The last column shows the maximum relative deviation of individual calibration data points from the average calibration line (S vs. ΔT), indicating maximum relative uncertainties in S.

ΔT [K]	D_a [nm]	S [%]	$\Delta S/S$ [%]
1.99±0.02	158.8±5.2	0.072±0.004	6.9
4.46±0.01	66.7±1.9	0.28±0.01	5.8
10.70±0.02	35.3±1.0	0.75±0.04	5.9
14.44±0.01	28.2±0.8	1.06±0.05	6.7
16.95±0.02	24.9±0.7	1.29±0.06	6.7

pressure due to measurement uncertainties; Rose et al., 2010b). The effective water vapor supersaturation (S) was regulated by the temperature difference between the upper and lower end of the CCNC flow column (ΔT) and calibrated as described below and in Sect. 2.2.3.

For each CCN measurement cycle, ΔT was set to 5 different levels in the range of 1.98–16.9 K corresponding to S values of 0.068% to 1.27%. For each ΔT and S, respectively, the diameter of the dry aerosol particles selected by the DMA (D) was set to 9 different values in the range of 20–290 nm. At each D, the number concentration of total aerosol particles (condensation nuclei, CN), N_CN, was measured with the CPC, and the number concentration of CCN, N_CCN, was measured with the CCNC. The integration time for each measurement data point was 30 s, the recording of a CCN efficiency spectrum ($N_\mathrm{CCN}/N_\mathrm{CN}$ vs. D) took ~16 min (including 50 s adjustment time for each new particle size and 4 min for adjustment to the next supersaturation level), and the completion of a full measurement cycle comprising CCN efficiency spectra at 5 different supersaturation levels took ~85 min (including 5 min for adjustment between the highest and lowest level of S).

3.2.2.2 Calibration of CCN counter

With respect to the effective water vapor supersaturation S, the CCNC was calibrated with ammonium sulfate aerosol as described in Sect. 2.2.3. During the campaign, five representative calibration experiments were performed, and in each of these experiments multiple CCN efficiency spectra were recorded for 5 different ΔT values. The midpoint activation diameter of each CCN efficiency spectrum was taken as the critical dry diameter for the CCN activation of ammonium sulfate particles, and the corresponding critical supersaturation was calculated with an activity parameterization Köhler model (AP3; Sect. B.2) that can be regarded as the most accurate reference available. The calculated critical supersaturation was taken as the effective supersaturation at the given ΔT value.

Figure 3.1 shows the average CCN efficiency spectra obtained from the 5 calibration experiments with ammonium sulfate aerosol, and the corresponding average calibration parameters are given in Table 3.1. A linear least-squares fit to the data pairs of S and ΔT was taken as the CCNC calibration line for the entire campaign: $S = k_\mathrm{s}\Delta T + S_0$ with k_s=0.08041% K^{-1} and S_0=−0.09109%, R^2=0.9929. It was applied to calculate S from the average value of ΔT recorded during each measurement of a CCN efficiency spectrum of atmospheric aerosol (cf. Fig. 2.5). As detailed in Sect. 2.3.6, variations

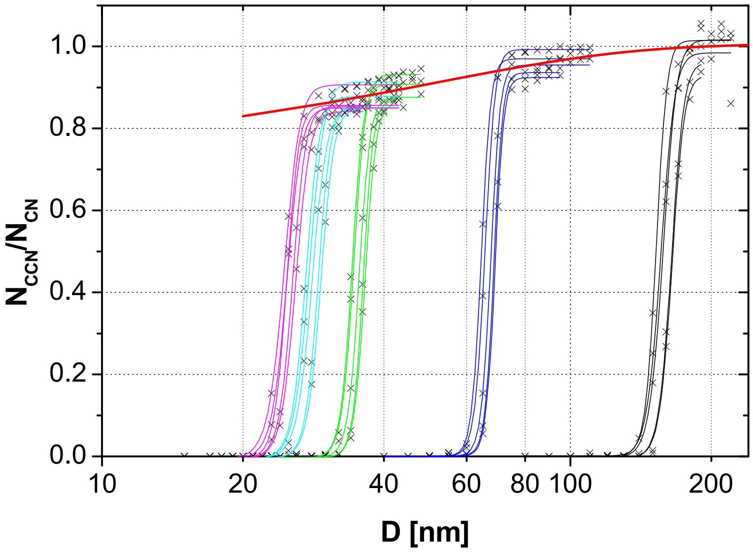

Figure 3.1: CCN efficiency spectra obtained from 5 calibration experiments with ammonium sulfate aerosol performed during the campaign (data points and CDF fits). Different colors indicate the different supersaturation levels. The red line is the asymptotic function that was used to correct for different counting efficiencies of the CPC and the CCNC (f_{corr}).

in S are mostly due to variations of the CCNC inlet temperature. The standard deviations of the calibration data points and their maximum deviations from the calibration line ($\Delta S/S$) as listed in Table 3.1 indicate a relative uncertainty of less than ~7% for S in the CCN measurements reported in this study.

3.2.2.3 Correction of measured CCN efficiency spectra

The measured atmospheric CCN efficiency spectra were corrected for multiply charged particles as described by Frank et al. (2006) and for the DMA transfer function as described in Sect. 2.2.3.3. For the multiple charge correction the total aerosol particle number size distributions measured in parallel with the TDMPS was used. For several days TDMPS data were not available, and no charge correction was performed. Nevertheless, the CCN data from these days remained comparable with the others, because the effects of the charge correction were generally small (<5% change in activation diameters and other parameters used for further analysis).

The CCN efficiency spectra were also corrected for the differences in the counting efficiencies of the CCNC and the CPC. If the CCNC and CPC counting efficiencies were the same, a maximum activated fraction of $N_{\mathrm{CCN}}/N_{\mathrm{CN}}\approx 1$ would be expected for ammonium sulfate calibration aerosol particles at all supersaturation levels. As illustrated in Fig. 3.1, however, the measured maximum value of $N_{\mathrm{CCN}}/N_{\mathrm{CN}}$ was close to one only for larger particles. For smaller particles the measured maximum levels of $N_{\mathrm{CCN}}/N_{\mathrm{CN}}$ decreased with decreasing particle size, which can be attributed to a decrease in the counting efficiency of the CCNC (most likely due to wall losses in the tubing inside the instrument). To correct for this bias, an asymptotic function has been fitted to those data points of the calibration efficiency spectra that reached at least 95% of their respective maximum values (red line in Fig. 3.1): $f_{\mathrm{corr}}=x_1-x_2\cdot x_3^D$ with x_1=1.00547, x_2=0.26208, x_3=0.98024, R^2=0.70881. The inverse of this correction function was multiplied with all the atmospheric $N_{\mathrm{CCN}}/N_{\mathrm{CN}}$ data points after the charge and before the transfer function corrections. In the following, for simplicity, the

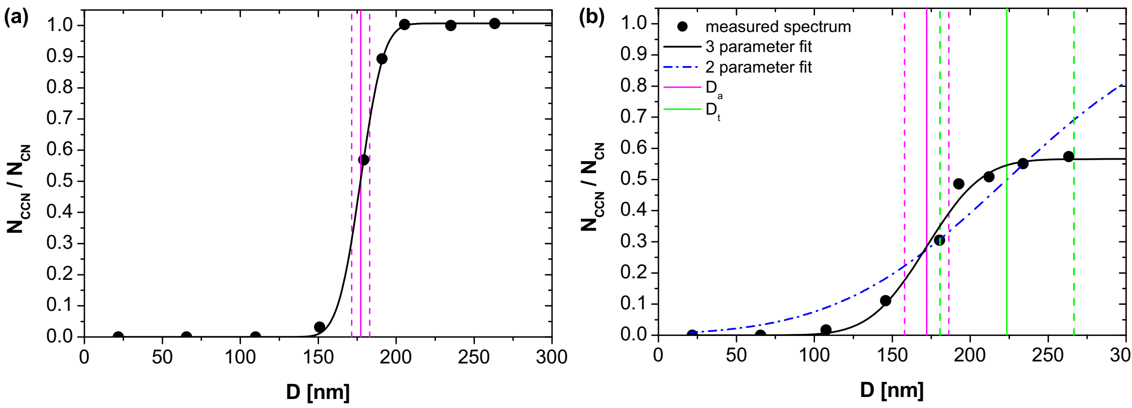

Figure 3.2: Exemplary CCN efficiency spectra **(a)** with "ideal" shape (12 July 2006, 18:55–19:06), and **(b)** with low maximum fraction of activated particles (9 July 2006, 03:23–03:34): measurement data points (corrected according to Sect. 3.2.2.3; black dots); 3-parameter CDF fit (black solid line) with fit parameters D_a (pink line), and σ_a (distance between pink dashed lines); 2-parameter CDF fit (blue dash-dotted line) with fit parameters D_t (green line) and σ_t (distance between green dashed lines).

corrected CCN efficiency spectra are referred to as the "measured" CCN efficiency spectra. Note that all CCN efficiency spectra presented in the figures of this chapter show the corrected ones.

The scattering of the highest $N_\mathrm{CCN}/N_\mathrm{CN}$ measurement values around the counting efficiency correction function determined in the calibration experiments (f_corr, Fig. 3.1) indicate a relative uncertainty of $\sim$5% for the CCN efficiencies determined for atmospheric aerosols (corrected CCN efficiency spectra). For the period after 20 July the relative uncertainty increased to $\sim$10%, as indicated by a decrease in the observed maximum CCN efficiencies (offset in the CCNC flow rate).

3.2.2.4 Parameters derived from the CCN efficiency spectra

Basic spectral parameters

The measured CCN efficiency spectra were fitted with a cumulative Gaussian distribution function (CDF; Eq. (2.1); Sect. 2.2.3.1). The following best-fit parameters were determined for each spectrum: the maximum activated fraction $\mathrm{MAF_f}=2a$, the midpoint activation diameter D_a, and the CDF standard deviation σ_a. In addition to the 3-parameter CDF fits with varying a, D_a, and σ_a, 2-parameter CDF fits were also performed, which were forced to $\mathrm{MAF_f}=1$ by fixing the parameter a at 0.5 and varying only D_a and σ_a. For the midpoint activation diameters and CDF standard deviations obtained from these fits, the symbols D_t and σ_t are used. In addition to the above CDF fit-based parameters, the CCN efficiency measured at the largest diameter of each spectrum (D_max) was also taken for further analysis and discussion: $\mathrm{MAF_m}=N_\mathrm{CCN}/N_\mathrm{CN}$ at $D_\mathrm{max}\approx270\,\mathrm{nm}$.

Characteristic examples of atmospheric CCN efficiency spectra of atmospheric aerosols and the corresponding CDF fits and parameters are illustrated in Fig. 3.2. Figure 3.2a shows an "ideal" spectrum that is characteristic for internally mixed aerosols with homogeneous composition and hygroscopicity of the particles (similar to ammonium sulfate calibration aerosol). In this case, the observed CCN efficiencies reach up to one ($\mathrm{MAF_f}\approx\mathrm{MAF_m}\approx1$), and the activation diameters and standard deviations derived from the 3-parameter and 2-parameter CDF fits are essentially the same ($D_\mathrm{a}\approx D_\mathrm{t}$; $\sigma_\mathrm{a}\approx\sigma_\mathrm{t}$).

At medium and high supersaturation (S=0.47–1.27%), most CCN efficiency spectra were qualitatively similar to the one in Fig. 3.2a. At low supersaturation (S=0.068–0.27%), however, most CCN efficiency spectra deviated from the ideal shape of a completely internally mixed aerosol and looked like the exemplary spectrum displayed in Fig. 3.2 b, which is characteristic for externally mixed aerosols.

In these cases, the highest observed CCN efficiencies remain well below one (MAF<1), which indicates an external mixture of CCN-active particles with CCN-inactive particles, whereby the difference in CCN activity is due to chemical composition and hygroscopicity (not particle size). Test experiments with different CCNC flow rates yielded the same result, indicating that the observed deviations of MAF from unity were not governed by potential kinetic limitations of water uptake in the CCNC.

For CCN efficiency spectra with MAF<1 the activation diameters and standard deviations derived from the 3-parameter and 2-parameter CDF fits are not the same: the 3-parameter fit results represent the average properties of the CCN active aerosol particle fraction, whereas the 2-parameter fit results approximate the overall properties of the external mixture of CCN-active and CCN-inactive particles.

The difference between unity and the maximum observed CCN efficiency (1–$\mathrm{MAF_m}$ or 1–$\mathrm{MAF_f}$, respectively) represents the fraction of externally mixed CCN-inactive particles at D_max or averaged over the diameter range of D_a to D_max, respectively. The CDF standard deviations are general indicators for the extent of external mixing and heterogeneity of particle composition in the investigated aerosol: σ_a characterizes the CCN-active particles in the size range around D_a, and σ_t characterizes the overall heterogeneity of CCN-active and -inactive particles in the size range around D_t. Under ideal conditions, the CDF standard deviations should be zero for an internally mixed, fully monodisperse aerosol with particles of homogeneous chemical composition. Even after correcting for the DMA transfer function, however, calibration aerosols composed of high-purity ammonium sulfate exhibit small non-zero σ_a values that correspond to $\sim$3% of D_a and can be attributed to heterogeneities of the water vapor supersaturation profile in the CCNC or other non-idealities such as DMA transfer function and particle shape effects (Sect. 2.3.2). Thus, normalized CDF standard deviations or "heterogeneity parameter" values of $\sigma_\mathrm{a}/D_\mathrm{a}\approx3\%$ indicate internally mixed CCN, whereas higher values indicate external mixtures of particles with varying chemical composition and hygroscopicity.

In addition to the activation diameters derived from the CCN efficiency spectra, an apparent cut-off diameter of CCN activation, D_cut, was also determined. It is the diameter above which the integral CN number concentration equals the observed CCN concentration ($N_\mathrm{CCN,S}$ as detailed below). Note that unlike D_a and D_t, the determination of D_cut requires knowledge of the CN size distribution and the assumption of a sharp cut-off (corresponding to σ_t=0).

Effective hygroscopicity parameters

As proposed by Petters and Kreidenweis (2007), an effective hygroscopicity parameter κ can be used to describe the influence of chemical composition on the CCN activity of aerosol particles, i.e. on their ability to absorb water vapor and act as CCN. Based on Köhler theory, κ relates the dry diameter of aerosol particles to the critical water vapor supersaturation, i.e. the minimum supersaturation required for cloud droplet formation. For a given supersaturation, κ allows calculating the critical dry particle diameter, i.e. the minimum diameter required for the particle to be CCN-active. According to measurements and thermodynamic models, κ is zero for insoluble materials like soot or mineral dust, $\sim$0.1 for secondary organic aerosols, $\sim$0.6 for ammonium sulfate and nitrate, $\sim$0.95–1 for sea salt (obtained from ρ_{ion} values in Niedermeier et al., 2008), and 1.28 for sodium chloride aerosols. The effective hygroscopicity of mixed aerosols can be approximated by a linear combination of the κ-values of the individual chemical components weighted by the volume or mass fractions, respectively (Kreidenweis et al., 2008; Gunthe et al., 2009; Dusek et al., 2010). On average, continental and marine aerosols tend to cluster around κ=0.3 and κ=0.7, respectively (Andreae and Rosenfeld, 2008; Kreidenweis et al., 2009; Pöschl et al., 2009). Laboratory experiments with biomass burning aerosols yielded κ values ranging from 0.02 to 0.8 (Petters et al., 2009).

For all data pairs of supersaturation and activation diameter derived from the CCN efficiency spectra measured in this study, κ parameters were calculated from the following Köhler model equation (equivalent to Eq. (B.30)):

$$s = \frac{D_{\mathrm{wet}}^3 - D^3}{D_{\mathrm{wet}}^3 - D^3(1-\kappa)} \exp\left(\frac{4\,\sigma_{\mathrm{sol}}\,M_{\mathrm{w}}}{R\,T\,\rho_{\mathrm{w}}\,D_{\mathrm{wet}}}\right) \tag{3.1}$$

κ was determined by inserting the observed activation diameter (D_{a}, D_{t}, or D_{cut}) for D and varying both κ and the droplet diameter D_{wet} until the saturation ratio s was equivalent at the same time to the prescribed supersaturation S and to the maximum of a Köhler model curve of CCN activation (numerical minimum search for $-s$ and for $|s-(1+S/100\%)|$ with Matlab "fminsearch" and start values of κ=0.2 and $D_{\mathrm{wet}}=D$).

For the temperature T=298.15 K was inserted, the droplet surface tension was approximated by that of water (σ_{sol}=0.072 J m^{-2}), and the other parameters were set to R=8.315 J K^{-1} mol^{-1} (gas constant), ρ_{w}=997.1 kg m^{-3} and M_{w}=0.018015 kg mol^{-1} (density and molar mass of water). Note that κ values derived from CCN measurement data through Köhler model calculations assuming the surface tension of pure water have to be regarded as "effective hygroscopicity parameters" that account not only for the reduction of water activity by the solute ("effective Raoult parameters") but also for surface tension effects. For more information see Petters and Kreidenweis (2007); Gunthe et al. (2009); Mikhailov et al. (2009); Pöschl et al. (2009). The parameter κ_{a} calculated from the data pairs of S and D_{a} characterizes the average hygroscopicity of CCN-active particles in the size range around D_{a}. κ_{t} calculated from D_{t} is an approximate measure (proxy) for the effective hygroscopicity of CCN-active and -inactive particles in the size range around D_{t}. Accordingly, κ_{t} is better suited for comparison with average κ values calculated from H-TDMA data and for the calculation of CCN number concentrations when CCN-active particles are externally mixed with CCN-inactive particles. On the other hand, κ_{a} is better suited for comparison with κ values predicted from AMS measurements, because κ_{a} is not influenced by CCN-inactive particles consisting mostly of insoluble and refractory materials like mineral dust and soot (or biopolymers that tend to char upon heating), which are not (or less efficiently) detected by AMS. The parameter κ_{cut} calculated from the data pairs of S and D_{cut} characterizes the effective average hygroscopicity of CCN-active particles in the size range above D_{cut}. D_{cut} and κ_{cut} can also be determined from the results of integrated CCN concentration measurements of polydisperse aerosols, and may thus be useful for comparison with studies lacking size-resolved CCN data.

CCN size distributions and number concentrations

CCN size distributions ($\mathrm{d}N_{\mathrm{CCN}}/\mathrm{dlog}D$) were calculated by multiplying the CCN efficiency spectra (3-parameter CDF fits of $N_{\mathrm{CCN}}/N_{\mathrm{CN}}$) with the total aerosol particle (CN) number size distributions measured in parallel ($\mathrm{d}N_{\mathrm{CN}}/\mathrm{dlog}D$). In these calculations, the fit parameter a was limited to a maximum value of 0.5 ($\mathrm{MAF_f}$=1), because CCN concentrations exceeding CN concentrations are physically not realistic. Additional test calculations with a not limited to 0.5 led to total CCN concentrations that were on average less than 1% higher.

Near the activation diameter, the size resolution of the CCN efficiency spectra was generally higher than that of the CN size distribution measurement data from the TDMPS ($\mathrm{dlog}D$=0.083). Thus the CN size distributions were linearly interpolated on a grid with ten-fold smaller size steps.

Total CCN concentrations ($N_{\mathrm{CCN,S}}$) were calculated by stepwise integration of the CCN size distributions with $\mathrm{dlog}D$=0.0083 from 3 to 900 nm. Note that insufficient size-resolution near the activation diameter can lead to substantial deviations in the calculation of total CCN number concentrations (up to ∼10% at low S, up to ∼5% at high S with $\mathrm{dlog}D$=0.083 vs. $\mathrm{dlog}D$=0.0083 in this study).

3.2.3 Aerosol mass spectrometry (AMS) measurement and data analysis

An Aerodyne quadrupole aerosol mass spectrometer (Q-AMS, referred to as "AMS" for brevity) was used to measure size-resolved chemical composition of non-refractory (∼600° C) submicron aerosol particles (Jayne et al., 2000). Performance of the AMS during the PRIDE-PRD2006 campaign is described in detail by Takegawa et al. (2009). The AMS data used in this study comprise a time series of mass size distributions ($\mathrm{d}M/\mathrm{d}\log D_{\mathrm{va}}$, ∼10 min time resolution) where D_{va} is the vacuum aerodynamic diameter (DeCarlo et al., 2004). The mass size distributions were calculated for inorganic ions ($\mathrm{SO_4^{2-}}$, $\mathrm{NH_4^+}$, $\mathrm{NO_3^-}$, $\mathrm{Cl^-}$) and organic matter (Org) in the size range between 45 nm and 1.4 μm.

The accuracy for major inorganic compounds ($\mathrm{SO_4^{2-}}$ and $\mathrm{NO_3^-}$) was estimated to be 14% based on routine calibrations. The limit of detection (LOD) was estimated by placing a particle filter in the sampling line. The estimated LODs (at 10 min) were 0.09, 0.5, 0.03, 0.03, and 0.4 $\mu\mathrm{g\,m^{-3}}$ for $\mathrm{SO_4^{2-}}$, $\mathrm{NH_4^+}$, $\mathrm{NO_3^-}$, $\mathrm{Cl^-}$, and Org, respectively.

An AMS particle collection efficiency (CE) of 0.5 was assumed. Overall reliability of the AMS measurements was evaluated based on intercomparison with other, collocated measurements including a PILS-IC and a Sunset Laboratory OC analyzer. As for the inorganic compounds ($\mathrm{SO_4^{2-}}$, $\mathrm{NH_4^+}$, $\mathrm{NO_3^-}$, $\mathrm{Cl^-}$), good agreement (regression slopes ranging from 0.87 to 1.20) was found between the AMS and the PILS-IC. The regression slope of AMS organic mass versus Sunset OC was 1.88, which is within the range of OM/OC ratios given by Turpin and Lim (2001).

The mass concentration data of every size bin were averaged with the two adjacent size bins to minimize the influence of noise. To make the size-resolved AMS results directly comparable with the CCN and VTDMA measurement results, all calculations and plots in this chapter using AMS data were based on approximate mobility equivalent diameters that have been calculated by division of the AMS vacuum aerodynamic diameter through a density scaling factor of 1.7. The scaling factor is based on the effective particle density of 1.7 $\mathrm{g\,cm^{-3}}$. It can be assumed to be the average value for this campaign since it has been found also for other similar locations (Cheng et al., 2006; Garland et al., 2008; Zhang et al., 2009). Accordingly, the AMS mass size distributions recorded in this campaign span a mobility size range of 27 nm to 850 nm.

For further analysis only the mass concentrations measured at particle sizes > 50 nm are used. Below this size, the AMS data are unreliable due to the low collection efficiency of the instrument. Size-resolved mass fractions were calculated diameter-wise from the size distributions of mass concentration. The mass fraction of one chemical component is its mass concentration divided by the sum of the masses of all components at this diameter.

In order to describe the chemical composition of the particles activated at the midpoint of the CCN efficiency spectrum, the AMS mass concentrations were integrated over the size interval of $D_{\mathrm{a}}-\sigma_{\mathrm{a}}$ to $D_{\mathrm{a}}+\sigma_{\mathrm{a}}$. The mass concentrations within these intervals (m_{D}) were used to calculate mass fractions of inorganic and organic compounds (f_{inorg}, f_{org}) for further calculations (e.g. correlation analysis). Note, that hence all CCN efficiency spectra with $D_{\mathrm{a}}-\sigma_{\mathrm{a}}<50$ nm (50 nm is the size below the AMS data are not used) were excluded from further analysis. This means that all CCN efficiency spectra measured at S=0.87% and a part of those at S=0.47% were excluded in the correlation analysis between CCN and AMS data.

3.2.4 Volatility measurement and data analysis

A Volatility Tandem Differential Mobility Analyzer (VTDMA; Philippin et al., 2004) was used to measure the number size distributions of the non-volatile residuals of monodisperse particles that were heated at 300°C (7 selected diameters in the range of 30–220 nm; time resolution of 1 hour for a complete cycle of 7 diameters). The material of continental submicrometer particles that is non-volatile at this temperature is considered to consist mainly of soot (Smith and O'Dowd, 1996; Burtscher et al., 2001; Kondo et al., 2006; Rose et al., 2006; Frey et al., 2008; Wehner et al., 2009).

Using a VTDMA, a clear distinction between fresh and aged soot particles can be made since the measured size distribution of non-volatile residuals usually separates in at least two modes. The mode which appears in the size range of the initially selected monodisperse particles represents the particles of low volatility. Their number concentration divided by the concentration of unconditioned particles yields the number fraction of particles of low volatility (ϕ_{lv}), i.e., of externally mixed fresh soot particles. Aged soot particles, however, have significantly smaller residuals due to the evaporated volatile coating and appear in another mode.

The number fraction of particles with low volatility, ϕ_{lv}, was measured by the VTDMA for 7 selected particle sizes (D_{VT}) per measurement cycle. A number size distribution of externally mixed fresh soot particles (soot size distribution for brevity) was calculated for every cycle by multiplying ϕ_{lv} with the particle number (CN) size distribution as measured by the TDMPS. The resulting data points were fitted with a lognormal distribution for inter- and extrapolation.

3.2.5 Optical measurement and data analysis

Total aerosol particle scattering coefficients at three different wavelengths (λ=450 nm, 550 nm, and 700 nm) were measured with an integrating nephelometer (Model 3563, TSI) and the aerosol particle absorption coefficient at 532 nm was determined with a photoacoustic spectrometer (PAS; Desert Research Institute); time resolution of 2 min. The single scattering albedo at λ=532 nm (ω_{532}) was

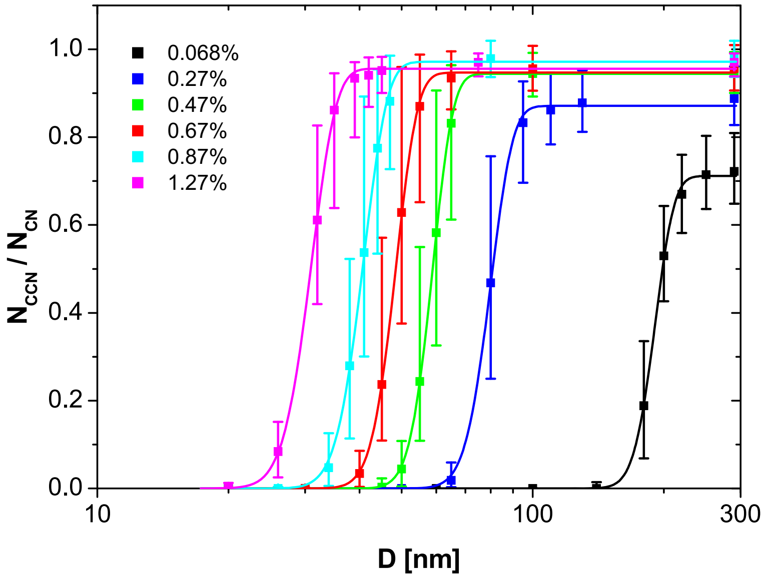

Figure 3.3: CCN efficiency spectra at S=0.068%–1.27% averaged over the entire campaign. The data points are median values calculated from the CDF fits to all measured spectra at the particle diameters initially selected with the DMA (20–290 nm). The error bars extend from the lower to the upper quartile, and the lines are 3-parameter CDF fits to the data points (Sect. 3.2.2.4).

calculated from these parameters as described by Garland et al. (2008) and was used to correlate with the CCN properties. For more information on the aerosol optical properties during this campaign see Garland et al. (2008).

3.3 CCN measurement results, hygroscopicity, and parameterizations

3.3.1 CCN efficiency spectra and related parameters

During the 30 day campaign period of PRIDE-PRD2006, ∼2200 size-resolved CCN efficiency spectra (activation curves) were measured for atmospheric aerosols at water vapor supersaturations in the range of 0.068% to 1.27%. Exemplary spectra are shown in Fig. 3.3, and the derivation and interpretation of characteristic parameters is explained in Sect. 3.2.2.4.

3.3.1.1 Campaign averages

Figure 3.3 shows campaign averages of the atmospheric CCN efficiency spectra at the six investigated supersaturation levels. The average parameters derived from the CCN efficiency spectra are summarized in Table 3.2.

As expected, the midpoint activation diameters D_a increased with S and were larger than the critical dry diameters for CCN activation of pure ammonium sulfate particles at the same supersaturation levels. At medium and high supersaturation (S=0.47–1.27%), the CCN efficiency spectra generally reached up to one ($\mathrm{MAF_f}\approx1$) and the relative standard deviations of the 3-parameter CDF fits were small ($\sigma_\mathrm{a}/D_\mathrm{a}\approx10\%$), which implies that nearly all aerosol particles larger than the midpoint activation diameter ($D>D_\mathrm{a}$) were CCN-active. At low supersaturation (S=0.068–0.27%), however, the maximum activated fractions remained on average well below one, which indicates a substantial

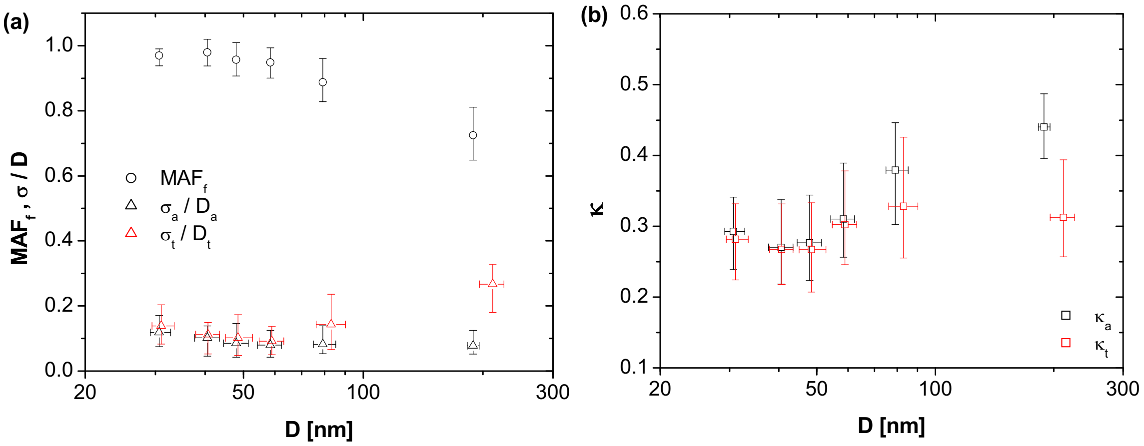

Figure 3.4: Characteristic parameters derived from the CCN efficiency spectra averaged over the entire campaign: **(a)** maximum activated fractions (MAF$_f$) and heterogeneity parameters (σ_a/D_a, σ_t/D_t); **(b)** hygroscopicity parameters (κ_a, κ_t) plotted against the midpoint activation diameter (D_a or D_t, respectively). The data points are median values corresponding to a given level of supersaturation, and the error bars extend to lower and upper quartiles.

portion (1−MAF$_f$) of externally mixed CCN-inactive particles with much lower hygroscopicity. At S=0.068%, the average MAF$_f$ was only ∼0.75 with minimum values as low as ∼0.4, i.e., even at diameters as large as ∼250 nm an average of ∼25% and up to ∼60% of the aerosol particles were not CCN-active. So far such high portions of externally mixed CCN-inactive particles have not been observed before in atmospheric aerosols.

Sensitivity tests with the κ-Köhler model described in Sect. 3.2.2.4 (Petters and Kreidenweis, 2007) indicate that particles as large as ∼300 nm must have an effective hygroscopicity parameter $\kappa<0.1$ to not be activated at S=0.068%. On the other hand, $S\approx0.7\%$ would be required to activate 300 nm particles that are wettable but completely insoluble and non-hygroscopic (κ=0). Most likely the CCN-inactive particles were freshly emitted (non-aged/non-coated) soot particles with $\kappa\approx0.01$, which will be discussed further Sect. 3.4.2. Other recent studies from PRIDE-PRD2006 (Garland et al., 2008) and a similar field campaign in the vicinity of Beijing (Cheng et al., 2009; Garland et al., 2009; Wehner et al., 2009; Wiedensohler et al., 2009) also indicate strong regional pollution with large proportions of externally mixed soot particles in the atmospheric aerosol near Chinese mega-cities and city-clusters.

Figure 3.4 a gives an overview of the maximum activated fractions (MAF$_f$) and normalized standard deviations (σ_a/D_a) of the 3-parameter CDF fits as well as the normalized standard deviations of the 2-parameter CDF fits (σ_t/D_t) to the measured CCN efficiency spectra. The average parameter values are plotted against the corresponding average midpoint activation diameters (D_a, D_t) that have been observed at the six prescribed levels of water vapor supersaturation (S=0.068–1.27%).

As detailed in Sect. 3.2.2.4, σ_a/D_a characterizes the heterogeneity of CCN-active particles in the size range around D_a, whereas σ_t/D_t characterizes the overall heterogeneity of aerosol particles in the size range around D_t.

For small particles in the nucleation or Aitken size range (∼30–70 nm), the heterogeneity parameters σ_a/D_a and σ_t/D_t were nearly identical and close to ∼10%. This is clearly higher than the

Table 3.2: Characteristic average CCN parameters (arithmetic mean values ± standard deviation) for the entire campaign, for the biomass burning event (BBE, 23–26 July) and for the campaign excluding the BBE for different S. Quantities are midpoint activation diameters (D_a, D_t, D_cut), maximum activated fractions (MAF$_\mathrm{f}$, MAF$_\mathrm{m}$), CDF standard deviations (σ_a, σ_t), heterogeneity parameters ($\sigma_\mathrm{a}/D_\mathrm{a}$, $\sigma_\mathrm{t}/D_\mathrm{t}$), hygroscopicity parameters (κ_a, κ_t, κ_cut), number concentrations of total aerosol particles (3–900 nm, $N_\mathrm{CN,tot}$) and of cloud condensation nuclei ($N_\mathrm{CCN,S}$), and ratio of $N_\mathrm{CN,tot}$ to $N_\mathrm{CCN,S}$ as defined in Sect. 3.2.2.4. n_ES and n_SD are the numbers of averaged CCN efficiency spectra and size distributions, respectively.

S [%]	D_a [nm]	D_t [nm]	D_cut [nm]	MAF$_\mathrm{f}$	MAF$_\mathrm{m}$	σ_a [nm]	σ_t [nm]	$\sigma_\mathrm{a}/D_\mathrm{a}$	$\sigma_\mathrm{t}/D_\mathrm{t}$
Entire campaign									
0.068	189.5±11.3	213.1±21.8	216.8±19.2	0.73±0.12	0.73±0.13	17.3±10.0	55.3±26.3	0.09±0.05	0.25±0.10
0.27	81.4±9.0	85.0±11.2	89.8±13.3	0.89±0.09	0.93±0.10	8.8±6.9	13.8±10.1	0.10±0.07	0.15±0.10
0.47	59.4±7.0	60.5±8.1	64.4±9.3	0.95±0.07	0.98±0.08	5.7±4.8	6.7±5.8	0.09±0.06	0.10±0.07
0.67	48.9±6.0	49.7±6.8	52.8±8.5	0.95±0.07	0.99±0.08	5.2±4.4	6.3±5.3	0.10±0.07	0.12±0.08
0.87	40.9±4.4	41.3±5.1	44.5±7.3	0.98±0.06	1.00±0.08	4.2±2.9	4.7±3.4	0.10±0.06	0.11±0.07
1.27	31.5±3.5	31.9±3.5	39.2±10.3	0.96±0.05	1.02±0.06	4.2±2.7	4.8±2.9	0.13±0.07	0.15±0.08
BBE									
0.068	204.8±12.2	222.3±21.4	234.8±21.3	0.75±0.09	0.76±0.10	17.8±9.9	43.4±19.2	0.09±0.05	0.19±0.08
0.27	93.3±11.9	98.9±13.2	107.3±15.6	0.87±0.10	0.92±0.10	17.6±9.1	23.7±9.4	0.18±0.09	0.23±0.08
0.47	68.7±9.2	71.4±10.3	77.9±9.4	0.92±0.05	0.96±0.05	11.8±6.3	14.2±7.3	0.16±0.07	0.19±0.08
0.67	59.3±7.1	62.8±8.0	69.4±8.0	0.91±0.06	0.94±0.06	12.0±4.6	15.8±7.0	0.20±0.06	0.24±0.08
0.87	46.5±5.4	48.2±7.1	55.5±8.2	0.94±0.05	0.98±0.06	7.3±3.8	8.8±4.8	0.15±0.08	0.18±0.09
1.27	33.9±4.9	35.0±4.6	51.3±13.4	0.92±0.07	0.99±0.03	5.6±3.7	7.3±3.4	0.16±0.09	0.20±0.09
Entire campaign excluding BBE									
0.068	187.4±9.4	211.8±21.5	213.6±17.1	0.73±0.13	0.73±0.14	17.3±10.1	56.9±26.7	0.09±0.05	0.26±0.11
0.27	79.8±7.2	83.1±9.5	86.8±10.2	0.89±0.09	0.93±0.10	7.7±5.6	12.5±9.5	0.09±0.06	0.14±0.10
0.47	58.3±5.8	59.1±6.6	62.2±7.3	0.95±0.07	0.98±0.08	4.9±4.0	5.7±4.9	0.08±0.06	0.09±0.06
0.67	48.0±5.0	48.6±5.3	51.1±6.4	0.96±0.07	0.99±0.08	4.6±3.8	5.4±4.2	0.09±0.07	0.11±0.08
0.87	40.2±3.7	40.4±4.0	42.7±5.3	0.98±0.06	1.01±0.08	3.9±2.5	4.2±2.8	0.09±0.06	0.10±0.06
1.27	31.0±2.9	31.2±2.9	35.6±5.5	0.97±0.04	1.03±0.06	3.9±2.3	4.3±2.5	0.12±0.06	0.13±0.07

S [%]	κ_a	κ_t	κ_cut	$N_\mathrm{CN,tot}$ [cm^{-3}]	$N_\mathrm{CCN,S}$ [cm^{-3}]	$N_\mathrm{CCN,S}/N_\mathrm{CN,tot}$	n_ES	n_SD
Entire campaign								
0.068	0.44±0.08	0.33±0.10	0.30±0.08		995±745	0.06±0.05	429	331
0.27	0.37±0.10	0.33±0.11	0.29±0.11		6531±3974	0.36±0.16	428	331
0.47	0.32±0.09	0.30±0.09	0.26±0.10		9649±5214	0.53±0.19	433	337
0.67	0.28±0.09	0.27±0.09	0.24±0.10		10 731±5991	0.59±0.20	299	230
0.87	0.28±0.08	0.28±0.09	0.23±0.09		12 967±6385	0.71±0.18	421	327
1.27	0.29±0.09	0.28±0.08	0.18±0.09		15 839±5602	0.85±0.10	123	97
all	0.34±0.11	0.30±0.10	0.26±0.10	18 150±7991			2133	1653
BBE								
0.068	0.35±0.06	0.28±0.07	0.24±0.06		1899±1157	0.14±0.06	51	49
0.27	0.25±0.09	0.21±0.09	0.17±0.07		7041±3753	0.46±0.16	50	49
0.47	0.21±0.08	0.19±0.08	0.14±0.05		8977±4448	0.59±0.16	48	46
0.67	0.16±0.06	0.13±0.06	0.10±0.04		8170±5648	0.54±0.12	24	22
0.87	0.19±0.07	0.18±0.07	0.12±0.06		11 565±5793	0.73±0.15	47	45
1.27	0.25±0.13	0.22±0.11	0.08±0.06		13 486±4171	0.85±0.07	22	22
all	0.24±0.10	0.21±0.09	0.15±0.08	15 178±6479			242	233
Entire campaign excluding BBE								
0.068	0.46±0.07	0.33±0.10	0.32±0.08		838±506	0.05±0.03	378	282
0.27	0.39±0.09	0.35±0.11	0.31±0.10		6442±4011	0.34±0.16	378	282
0.47	0.33±0.08	0.32±0.09	0.28±0.09		9755±5324	0.52±0.19	385	291
0.67	0.29±0.08	0.28±0.08	0.25±0.09		11 002±5975	0.60±0.21	275	208
0.87	0.29±0.08	0.29±0.08	0.25±0.09		13 191±6456	0.70±0.19	374	282
1.27	0.30±0.07	0.29±0.07	0.21±0.08		16 529±5801	0.85±0.10	101	75
all	0.35±0.10	0.31±0.09	0.28±0.10	18 638±8111			1891	1420

$\sim$3% observed for aerosols of homogeneous chemical composition (e.g. pure ammonium sulfate), indicating that the particles in this size range were not fully internally mixed with respect to their solute content. For larger particles in the accumulation size range ($\sim$70–200 nm), $\sigma_{\rm a}/D_{\rm a}$ remained at $\sim$10% whereas $\sigma_{\rm t}/D_{\rm t}$ increased strongly up to $\sim$25% at $\sim$200 nm. This confirms that the CCN-active particles in the accumulation size range had fairly homogeneous properties but were externally mixed with CCN-inactive particles.

Figure 3.4 b gives an overview of the effective hygroscopicity parameters ($\kappa_{\rm a}$, $\kappa_{\rm t}$) that have been derived from the midpoint activation diameters ($D_{\rm a}$, $D_{\rm t}$) of the 3-parameter and 2-parameter CDF fits, respectively. As detailed in Sect. 3.2.2.4, $\kappa_{\rm a}$ calculated from S and $D_{\rm a}$ characterizes the average hygroscopicity of CCN-active particles in the size range around $D_{\rm a}$, whereas $\kappa_{\rm t}$ calculated from S and $D_{\rm t}$ is a proxy for the effective hygroscopicity of mixtures of CCN-active and -inactive particles in the size range around $D_{\rm t}$.

For small particles in the nucleation or Aitken size range ($\sim$30–70 nm), $\kappa_{\rm a}$ and $\kappa_{\rm t}$ were nearly identical and close to $\sim$0.3. For larger particles in the accumulation size range ($\sim$70–200 nm), however, $\kappa_{\rm a}$ increased substantially to $\sim$0.4–0.5, whereas $\kappa_{\rm t}$ increased only slightly to $\sim$0.33.

Overall, larger particles were on average more hygroscopic but also more heterogeneous than smaller particles. The observed values of $\kappa_{\rm a}$, $\kappa_{\rm t}$, $\sigma_{\rm a}/D_{\rm a}$, $\sigma_{\rm t}/D_{\rm t}$, and MAF$_{\rm f}$ suggest that the particles in the nucleation or Aitken size range were composed mostly of organics and sulfate and were largely but not fully internally mixed, whereas the particles in the accumulation size range consisted mostly of an external mixture of soot particles (κ<0.1; $\sim$25% at $\sim$200 nm) and sulfate-rich particles ($\kappa\approx$0.4–0.5; $\sim$75% at $\sim$200 nm). Note that the properties of large accumulation mode particles are not only important for cloud formation at low and medium supersaturation (low and moderate updraft velocities; Segal and Khain, 2006; Reutter et al., 2009) but also for aerosol optical properties and direct radiative effects on climate (Garland et al., 2008). These and other aspects of aerosol chemical composition and mixing state will be explored further and discussed in more detail in Sect. 3.4.1. Averaged over all diameters, the mean hygroscopicity parameter values for the entire campaign were $\kappa_{\rm a}$=0.34 and $\kappa_{\rm t}$=0.30 (Table 3.2). The hygroscopicity parameter related to the cut-off diameter $D_{\rm cut}$ ($\kappa_{\rm cut}$) was on average 10% smaller than $\kappa_{\rm t}$ and had an arithmetic mean value of 0.26.

3.3.1.2 Time series and biomass burning event

Figure 3.5 shows the time series of characteristic parameters ($D_{\rm a}$, $D_{\rm t}$, $\kappa_{\rm a}$, $\kappa_{\rm t}$, $\sigma_{\rm a}$, $\sigma_{\rm t}$, $\sigma_{\rm a}/D_{\rm a}$, $\sigma_{\rm t}/D_{\rm t}$, MAF$_{\rm f}$, MAF$_{\rm m}$) derived from the atmospheric CCN efficiency spectra measured throughout the campaign. For clarity, the parameters in Fig. 3.5 c–j are shown only for the smallest and largest supersaturations that were measured during the entire campaign (S=0.068%, S=0.87%). The temporal evolution of most parameters at S=0.068% was qualitatively similar to S=0.27%, and that at S=0.87% was representative for S=0.47–1.27%.

Most parameters exhibited pronounced diurnal cycles which are consistent with the results of other recent studies from PRIDE-PRD2006 (Garland et al., 2008; Hua et al., 2008). The diurnal cycles in CCN properties will be described and discussed together with the variability of other aerosol properties in Sect. 3.4. As illustrated in Fig. 3.5 i and j, both the fitted and the measured maximum activated fractions (MAF$_{\rm f}$, MAF$_{\rm m}$) dropped by $\sim$10% after 20 July, which is most likely due to a measurement artifact (offset in the flow rate of the CCNC).

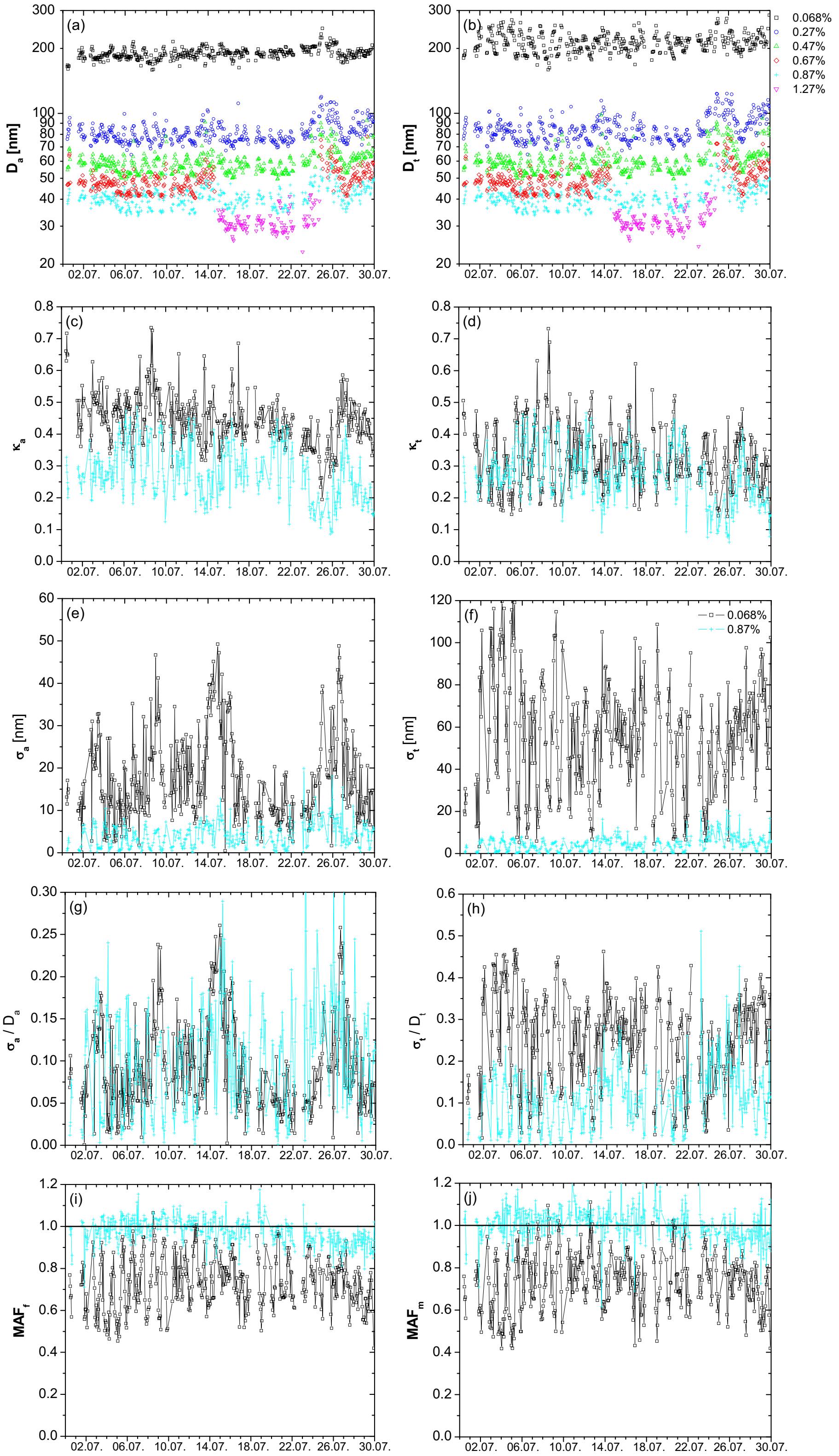

Figure 3.5: Time series of the characteristic parameters derived from the CCN efficiency spectra measured at different supersaturations plotted against the date in July 2006.

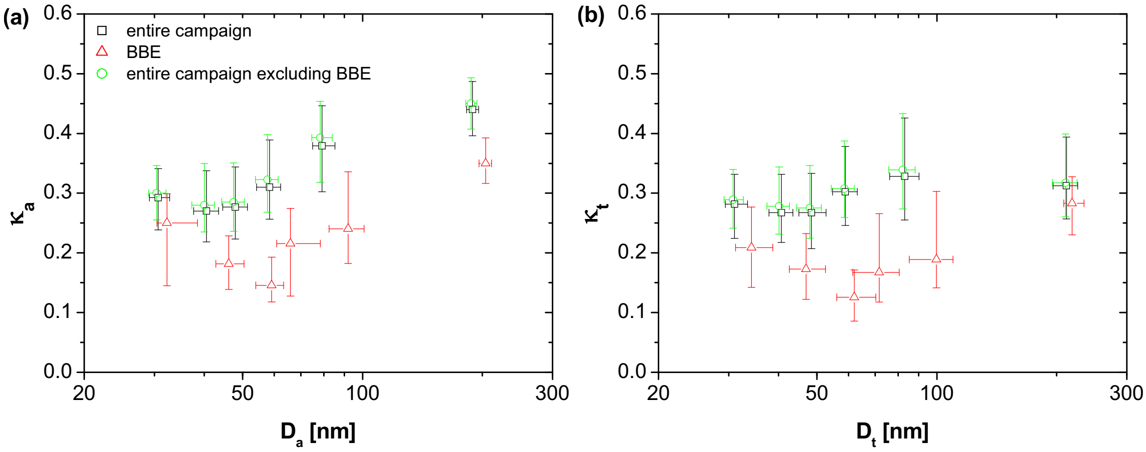

Figure 3.6: Hygroscopicity parameters **(a)** for the CCN-active particles (κ_a) and **(b)** for the total aerosol (κ_t) averaged over different periods: the entire campaign, the biomass burning event (BBE) and the campaign excluding the biomass burning event. The data points are median values corresponding to a given level of supersaturation, and the error bars extend to lower and upper quartiles.

In addition to the diurnal variability, several CCN parameters exhibited pronounced changes during high pollution events. Especially on 23–26 July, the midpoint activation diameters and standard deviations of the CDF fits increased and the hygroscopicity parameters decreased relative to the campaign average (Fig. 3.5, panels a–h). The changes indicate an increase in the portion of particulate matter with low hygroscopicity (organic substances) and in the heterogeneity of particles (external mixing), and they were most pronounced for small particles ($\sim$30–80 nm; S≥0.27%).

The highly polluted period of 23–26 July 2006 was characterized by intense local biomass burning and very high aerosol mass concentrations (Garland et al., 2008). During this period, the source of the pollution was evident and unique: the burning of plant waste by local farmers was visible in the vicinity surrounding the measurement site, and it was the only time that such intense local biomass burning and pollution occurred during the campaign. The heavy biomass burning event started after a power outage in the evening of 22 July and ended by heavy rainfalls beginning at $\sim$13:00 on 26 July. Thus the period of 23 July, 00:00–26 July, 12:59 will be referred to as the "biomass burning event (BBE)". The average CCN parameters for this period are summarized in Table 3.2.

During the BBE, the CCN efficiency spectra were shifted towards larger particle sizes for all supersaturations, reflecting lower CCN activity than during the rest of the campaign. The increase of D_a was most pronounced for S=0.67% (+22% during the BBE) and least different for S=0.068% and S=1.27% (+8% during the BBE). Moreover, for all supersaturations, except 0.068%, the standard deviations of the CDF fits and heterogeneity parameters (σ/D), increased by factors up to $\sim$2, indicating a strong increase in the heterogeneity of small particles (30–100 nm, Table 3.2). Only the maximum activated fractions did not change significantly during the biomass burning event, i.e., the externally mixed fraction of particles that could not be activated at low S remained the same.

Figure 3.6 gives an overview of the effective hygroscopicity parameters (κ_a, κ_t) that have been derived from the midpoint activation diameters (D_a, D_t) averaged over the entire campaign and over the biomass burning event. Figure 3.6 a shows that during the BBE the average hygroscopicity of

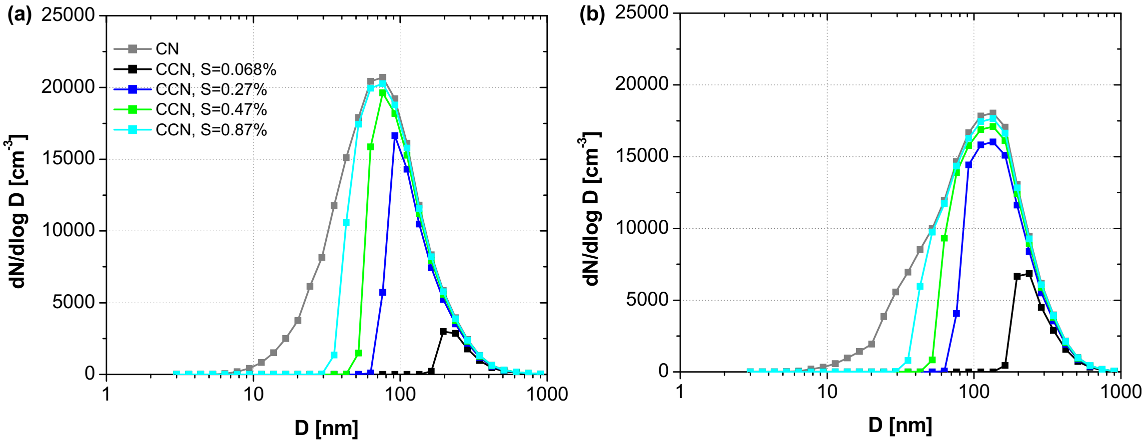

Figure 3.7: Number size distributions of total aerosol particles (CN) and cloud condensation nuclei (CCN) averaged over **(a)** the entire campaign and **(b)** the biomass burning event. The CCN size distributions were calculated by multiplying the median CN size distribution with the median CCN efficiency spectra from Fig. 3.3. For clarity and to avoid potential biases due to different averaging times, CCN size distributions are displayed only for the supersaturation levels covered throughout the campaign.

CCN-active particles was substantially reduced at all sizes. Averaged over all diameters, the mean value of κ_a during the BBE was ~30% lower than during the rest of the campaign: 0.24 vs. 0.34 (Table 3.2).

As illustrated in Fig. 3.6 b, the average hygroscopicity of the total aerosol, including CCN-active and -inactive particles, was also strongly reduced for small particles (<100 nm) but not so much for large particles (~200 nm). Averaged over all diameters, however, the mean value of κ_t during the BBE was also ~30% lower than during the rest of the campaign: 0.21 vs. 0.30 (Table 3.2).

These are the first size-resolved CCN field measurement data and hygroscopicity parameters reported for freshly emitted biomass burning smoke in the atmosphere. They are consistent with earlier lab studies reporting low hygroscopicity of freshly emitted biomass burning particles (Rissler et al., 2006; Andreae and Rosenfeld, 2008; Petters et al., 2009).

3.3.2 CCN size distributions and number concentrations

Figure 3.7 shows total aerosol particle (CN) and CCN number size distributions averaged over the entire campaign and over the biomass burning event, respectively. The corresponding averages of the total CCN number concentrations ($N_{\mathrm{CCN,S}}$) and of the total CCN efficiencies ($N_{\mathrm{CCN,S}}/N_{\mathrm{CN,tot}}$) are summarized in Table 3.2. As illustrated in Fig. 3.7 a, the average CN size distribution for the entire campaign was monomodal with a maximum at ~70 nm, and the corresponding total particle number concentration was $N_{\mathrm{CN,tot}}$=1.8×10^4 cm^{-3} (Table 3.2). At S=0.068% the CCN size distribution accounted only for ~5% of $N_{\mathrm{CN,tot}}$, because only a minor fraction of the CN were larger than the activation diameter (~200 nm). At S=0.27–0.87% the CCN activation diameters were close to the maximum of the CN number mode and the integral CCN efficiencies were substantially higher ($N_{\mathrm{CCN,S}}/N_{\mathrm{CN,tot}}$=36–71%; Table 3.2). During the biomass burning event (Fig. 3.7 b), the CN size distribution was broader and the maximum was shifted to larger sizes (~120 nm, a value typical of biomass smoke; Reid et al., 2005). The average number concentration of CN was slightly smaller

Table 3.3: Characteristic deviations between observed CCN number concentrations $N_{\mathrm{CCN,S}}$ and CCN number concentrations predicted by different model approaches ($N_{\mathrm{CCN,S,p}}$): arithmetic mean values of the relative bias ($\Delta_{\mathrm{b}}N_{\mathrm{CCN,S}}$=($N_{\mathrm{CCN,S,p}}-N_{\mathrm{CCN,S}}$)/$N_{\mathrm{CCN,S}}$) and of the total relative deviation ($\Delta_{\mathrm{d}}N_{\mathrm{CCN,S}}=|N_{\mathrm{CCN,S,p}}-N_{\mathrm{CCN,S}}|/N_{\mathrm{CCN,S}}$, including systematic and statistical errors). CPL is the classical power law and MPL the modified power law approach, respectively. $\mathrm{SD_m}$ is the campaign average CN size distribution (Fig. 3.7 a), and $\mathrm{SD_u}$ and $\mathrm{SD_r}$ are the generic urban and rural size distributions as listed in Seinfeld and Pandis (2006, Table 8.3), respectively. n_{SD} is the number of data points.

S	CPL		MPL		κ_{t} var.		κ_{a} var.		κ_{t}=0.3		κ_{a}=0.34		κ_{cut}=0.26		κ_{t} var., const. $\mathrm{SD_m}$		κ_{t} var., const. $\mathrm{SD_u}$		κ_{t} var., const. $\mathrm{SD_r}$		n_{SD}
	bias	dev.	bias	dev.	bias	dev.	bias	dev.	bias	dev.	bias	dev.	bias	dev.	bias	dev.	bias	dev.	bias	dev.	
[%]	[%]	[%]	[%]	[%]	[%]	[%]	[%]	[%]	[%]	[%]	[%]	[%]	[%]	[%]	[%]	[%]	[%]	[%]	[%]	[%]	
0.068	+310.7	313.3	+33.9	63.6	+2.5	8.6	+41.4	41.4	+4.2	19.5	+16.6	24.9	−8.8	18.8	+33.2	71.5	+95.3	113.8	−75.3	77.2	331
0.27	+54.6	89.6	+32.5	53.4	+6.7	7.4	+13.2	13.5	+6.4	17.2	+13.0	19.4	−1.0	16.5	+38.9	72.1	+123.4	132.4	−74.6	76.3	331
0.47	+37.7	75.2	+22.1	37.5	+5.1	5.8	+6.9	7.3	+8.4	12.8	+12.9	15.2	+3.3	11.4	+35.2	68.2	+134.7	138.8	−76.7	77.4	337
0.67	+57.1	85.5	+20.2	33.0	+4.3	4.6	+5.9	6.3	+11.4	14.0	+15.1	16.5	+7.2	12.0	+45.6	74.4	+171.5	173.3	−75.2	75.9	230
0.87	+41.2	69.2	+11.9	21.3	+3.4	3.6	+4.0	4.1	+7.5	9.0	+10.1	10.7	+4.6	7.6	+26.7	60.6	+161.3	162.6	−78.0	78.1	327
1.27	+23.8	43.3	+1.9	6.2	+4.7	4.7	+5.0	5.0	+5.7	6.0	+6.9	6.9	+4.3	5.4	−1.5	39.1	+145.9	145.9	−81.1	81.1	97
all	+98.3	124.1	+23.1	40.3	+4.4	6.0	+14.2	14.5	+7.2	14.0	+13.1	16.8	+0.8	12.9	+33.2	67.3	+135.6	142.4	−76.3	77.3	1653

($\sim$1.5$\times$10^4 cm^{-3}), but due to the larger average particle sizes the CCN number concentrations at S=0.068% and 0.27% were higher (+90% and +8%, respectively). For $S\geq$0.47%, however, $N_{\mathrm{CCN,S}}$ was lower compared to the rest of the campaign (Table 3.2).

The geometric mean diameters (D_{g}), standard deviations (σ_{g}), and integral number concentrations (N_{g}) of monomodal lognormal fits to the median CN size distributions were D_{g}=70 nm, σ_{g}=1.94, and N_{g}=14 600 cm^{-3} for the entire campaign, and D_{g}=107 nm, σ_{g}=2.09, and N_{g}=14 200 cm^{-3} for the biomass burning event.

The number concentration of total aerosol particles ($N_{\mathrm{CN,tot}}$) and cloud condensation nuclei ($N_{\mathrm{CCN,S}}$) exhibited high temporal variability throughout the campaign with ranges of $\sim$10^3–4$\times$10^4 cm^{-3} for $N_{\mathrm{CN,tot}}$ and $\sim$10^2–3$\times$10^3 cm^{-3}, $\sim$10^3–2$\times$10^4 cm^{-3}, and $\sim$3$\times$10^3–3$\times$10^4 cm^{-3} for $N_{\mathrm{CCN,S}}$ at S=0.068%, 0.27%, and 0.87%, respectively. The corresponding mean values and standard deviations are listed in Table 3.2. Similarly high CCN number concentrations have been observed near the city of Beijing, China (Appendix C; Wiedensohler et al., 2009)

3.3.3 Prediction of CCN number concentration

In this section different model approaches are compared for the approximation/prediction of CCN concentration as a function of water vapor supersaturation, aerosol particle number concentration, size distribution and hygroscopicity: (1) the classical power law approach relating $N_{\mathrm{CCN,S}}$ to $N_{\mathrm{CCN,1}}$, i.e., to the CCN concentration at S=1%; (2) a modified power law approach relating $N_{\mathrm{CCN,S}}$ to the concentration of aerosol particles with $D>$30 nm ($N_{\mathrm{CN,30}}$); and (3) the κ-Köhler model approach relating $N_{\mathrm{CCN,S}}$ to the aerosol particle size distribution (dN_{CN}/d log$D$) and effective hygroscopicity. For all data points obtained during the campaign, the model results were compared with the observed values, and the mean values of the relative deviations are summarized in Table 3.3.

3.3.3.1 Classical power law

Figure 3.8 shows the campaign median values of $N_{\mathrm{CCN,S}}$ plotted against S and a power law fit

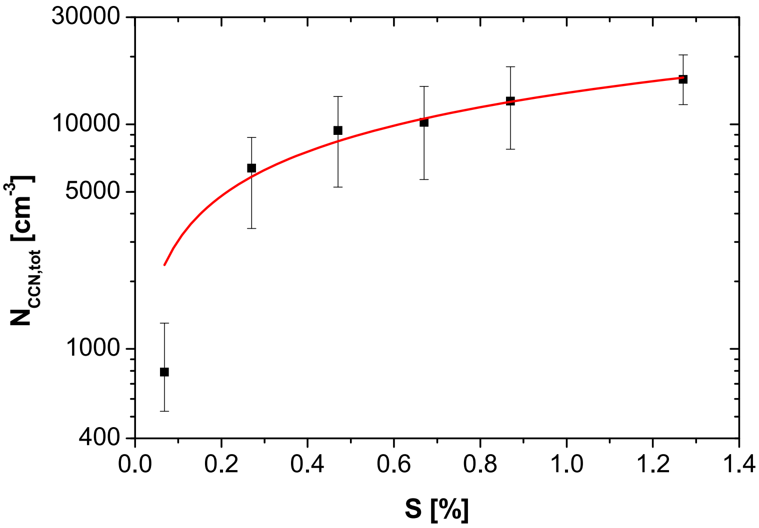

Figure 3.8: CCN number concentrations ($N_{\mathrm{CCN,S}}$) averaged over the entire campaign and plotted against water vapor supersaturation (S). The data points are median values, and error bars extend to lower and upper quartiles. The red line is a classical power law fit of the function $N_{\mathrm{CCN,S}}{=}N_{\mathrm{CCN,1}}{\cdot}(S/(1\%))^k$ with the best fit parameters $N_{\mathrm{CCN,1}}$=13 699 cm^{-3} and k=0.65 (R^2=0.97, n=6).

of the function $N_{\mathrm{CCN,S}}{=}N_{\mathrm{CCN,1}}{\cdot}(S/(1\%))^k$ (Pruppacher and Klett, 1997, Origin 6.1G software, Levenberg-Marquardt algorithm). The obtained fit parameter $N_{\mathrm{CCN,1}}{\approx}1.4{\times}10^4$ cm^{-3} is substantially higher than any previously reported value, and $k{\approx}0.65$ is within the range of values reported for other continental locations (0.4–0.9; Pruppacher and Klett, 1997; Andreae, 2009). The mean relative deviations of the individual measurement data points from the average power law were in the range of 40–90% for S=0.27–1.27%, but as high as 310% for S=0.068% (Table 3.3).

3.3.3.2 Modified power law

Figure 3.9 shows all observed values of $N_{\mathrm{CCN,S}}$ plotted against $N_{\mathrm{CN,30}}$ and power law fits of the form $N_{\mathrm{CCN,S}}{=}N_{\mathrm{CN,30}}{\cdot}s^{-q}$ with s=1+S/(100%) (Pruppacher and Klett, 1997, Origin 6.1G software, Levenberg-Marquardt algorithm). An overview of the best fit values obtained for the exponent q and the corresponding correlation coefficients is given in Table 3.4. In this approach, CN with $D{<}30$ nm were excluded, because they are generally not CCN-active and highly variable due to new particle formation (nucleation events). Moreover, the water vapor saturation ratio s was used instead of the supersaturation S, because the exponent varies more regularly with s than with S (Table 3.4: monotonous dependence of q on s vs. non-monotonous dependence of Q on S). At high supersaturations ($S{\geq}0.47\%$), $N_{\mathrm{CCN,S}}$ was fairly well correlated to $N_{\mathrm{CN,30}}$ (R^2=0.69–0.95), and the mean relative deviations between the power law fit and the observed values of $N_{\mathrm{CCN,S}}$ were less than 40% (Table 3.3). At S=0.27% the correlation was much worse (R^2=0.49, mean deviation 54%), and at S=0.068% there was practically no correlation and the individual $N_{\mathrm{CCN,S}}$ data points deviated by up to one order of magnitude from the power law fit (R^2=0.04, mean deviation 64%).

3.3.3.3 κ-Köhler model with variable CN size distribution

In Fig. 3.10, predicted CCN number concentrations ($N_{\mathrm{CCN,S,p}}$) that were obtained with the κ-Köhler model and different hygroscopicity parameters are plotted against observed values of $N_{\mathrm{CCN,S}}$.

Table 3.4: Fit parameter Q and q of the modified power law fit functions $N_{\mathrm{CCN,S}}=N_{\mathrm{CN,30}} \cdot (S/(1\%))^{Q}$ and $N_{\mathrm{CCN,S}}=N_{\mathrm{CN,30}} \cdot s^{-q}$, respectively. The correlation coefficient R^2 is the same for both fits. n_{SD} is the number of data points.

S [%]	s	Q	q	R^2	n_{SD}
0.068	1.00068	1.07	4242	0.04	331
0.27	1.0027	0.72	349.8	0.49	331
0.47	1.0047	0.71	114.5	0.69	337
0.67	1.0067	1.01	60.29	0.78	230
0.87	1.0087	1.78	28.67	0.87	327
1.27	1.0127	−0.53	9.95	0.95	97

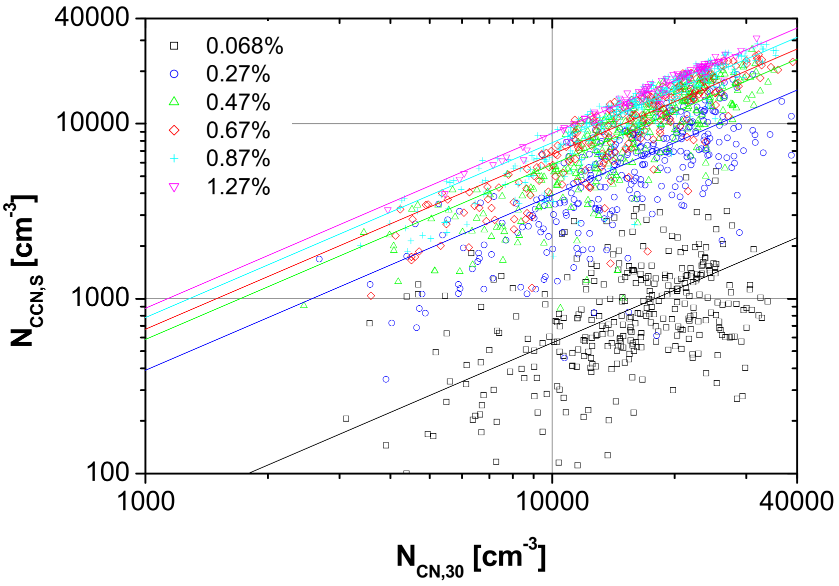

Figure 3.9: CCN number concentrations ($N_{\mathrm{CCN,S}}$) observed at different supersaturation levels plotted against the number concentration of aerosol particles with D>30 nm ($N_{\mathrm{CN,30}}$). The lines are modified power law fits of the function $N_{\mathrm{CCN,S}}=N_{\mathrm{CN,30}} \cdot s^{-q}$ with the parameter q as given in Table 3.4.

For each data point, $N_{\mathrm{CCN,S,p}}$ was calculated by integrating the measured CN size distribution above the critical dry particle diameter for CCN activation that corresponds to the given values of κ and S (Sects. 3.2.2.4 and 3.3.2).

As illustrated in Fig. 3.10 a, the predicted and observed values of $N_{\mathrm{CCN,S}}$ are in very good agreement, when for each data point κ_{t} was taken from the CCN efficiency spectrum measured in parallel to the CN size distribution. With this approach, the mean relative deviation averaged over all supersaturations was only 6%, and the overall mean bias of the model values was +4% (Table 3.3). The agreement demonstrates that κ_{t} is a suitable proxy for the effective hygroscopicity and CCN activity of the investigated ensemble of aerosol particles including CCN-active and -inactive particles. The deviations and the bias increased with lower S, which can be explained by the decreasing MAF,

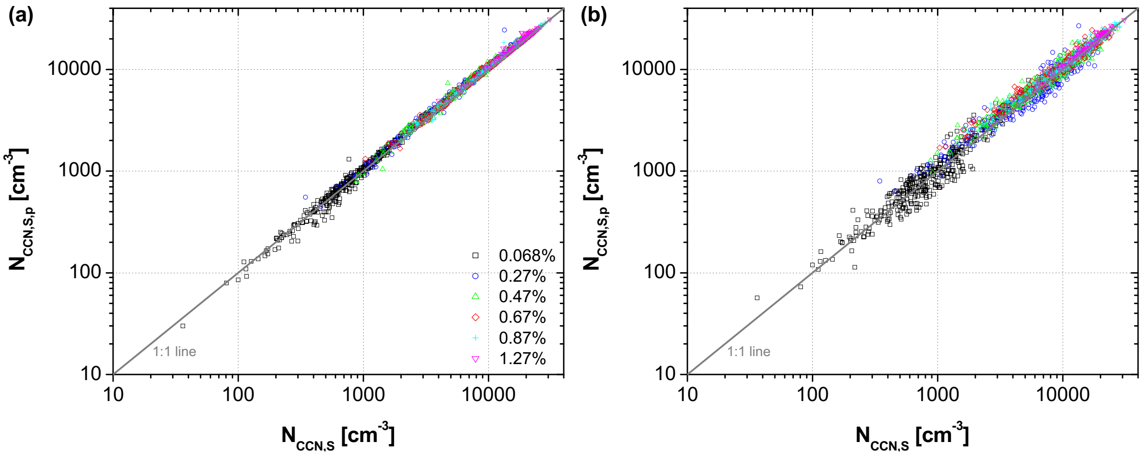

Figure 3.10: Predicted CCN number concentrations ($N_{\mathrm{CCN,S,p}}$) based on the κ-Köhler model approach **(a)** with variable values of κ_{t} as derived from individual CCN efficiency spectra and **(b)** with a constant average value of κ=0.3 plotted against the observed CCN number concentrations ($N_{\mathrm{CCN,S}}$).

indicating that the effect of external mixing between CCN-active and -inactive particles is not fully captured by κ_{t}. Nevertheless, the results obtained with κ_{t} were clearly better than with κ_{a}, which represents the effective hygroscopicity of the CCN-active particles only and thus leads to higher mean deviation and bias (15%, +14%, Table 3.3). Only at S=0.47–1.27%, where $\mathrm{MAF_f}\approx 1$ and $\kappa_{\mathrm{a}}\approx\kappa_{\mathrm{t}}$, were the results obtained with individual κ_{a} values nearly the same as with individual κ_{t}, and thus the overall mean bias and deviation were significantly higher (+14%, 15%, Table 3.3).

Fair agreement was also achieved when the campaign average value of κ_{t}=0.30 and the corresponding constant activation diameters for the prescribed supersaturation levels (215, 86, 59, 47, 39, and 30 nm; S=0.068–1.27%) were used for the calculation of $N_{\mathrm{CCN,S}}$ from the individual measured CN size distributions. With this approach, the overall mean relative deviation was more than twice as high, but the bias was hardly higher than when individual κ_{t} values were used (14% and +7.2%, respectively; Table 3.3; Fig. 3.10 b). Note that the campaign average value of κ_{t} equals the average value of hygroscopicity parameters observed or inferred for other continental locations (Andreae and Rosenfeld, 2008; Pöschl et al., 2009, and references therein) in agreement with global model simulations (Tsigaridis et al., 2006; Kreidenweis et al., 2009).

The approach using a constant average value of κ=0.3 cannot fully account for the observed temporal variations in aerosol composition and CCN properties. It yields relative deviations in the range of -40% to +80% of $N_{\mathrm{CCN,S}}$. Under most circumstances, however, i.e., for 76% of all data points, the deviations were still less than ±20%, which appears quite reasonable for data that span more than two orders of magnitude. Even during the BBE, which was characterized by ~30% lower hygroscopicity parameters ($\kappa_{\mathrm{t}}\approx$0.2; Sect. 3.3.1.2), the average deviation between predicted and observed $N_{\mathrm{CCN,S}}$ was only 21%.

With average or individual values of κ_{a}, the positive bias was higher than with κ_{t} (6–10%, Table 3.3). The approach using individual values of κ_{cut} yielded the same concentrations as observed because $N_{\mathrm{CCN,S,p}}$ was calculated from κ_{cut} in the reverse way as κ_{cut} from $N_{\mathrm{CCN,S}}$. With a constant average value of κ_{cut}=0.26, the relative deviations were essentially the same as with constant κ_{t}.

3.3.3.4 κ-Köhler model with constant CN size distribution

To test the relative importance of aerosol particle size distribution and hygroscopicity for the variability of $N_{\mathrm{CCN,S}}$, I performed additional Köhler model calculations in which the effective hygroscopicity parameters were allowed to vary (variable κ_{t} from the fitting of measured CCN efficiency spectra) while the CN size distribution was kept constant. In analogy to Gunthe et al. (2009), I used the campaign average size distribution (Fig. 3.7 a) and a generic urban and rural size distribution as listed in Seinfeld and Pandis (2006, Table 8.3, based on Jaenicke, 1993) with three lognormal modes, respectively.

With the constant campaign average size distribution (Fig. 3.7 a) and variable κ_{t}, the mean relative deviation between observed and predicted CCN concentrations ($\sim$70%) was higher by a factor of $\sim$5 than with the constant campaign average value of κ_{t}=0.3 and variable size distribution ($\sim$15%, Table 3.3). Assuming a constant generic size distribution for urban areas with variable κ_{t}, the mean relative deviation between observed and predicted CCN concentrations ($\sim$140%) was higher by a factor of 10 than under the assumption of an average value of κ_{t}=0.3 with variable size distribution (14%, Table 3.3). Assuming a constant generic size distribution for rural areas with variable κ_{t}, the mean relative deviation between observed and predicted CCN concentrations ($\sim$80%) were only a little higher than when assuming the campaign average size distributions, but lead to an underprediction of $N_{\mathrm{CCN,S}}$.

This demonstrates that the variability of CCN concentrations is much more strongly influenced by the variability of aerosol particle number concentration and size distribution than by the variability of aerosol composition and hygroscopicity. This applies for the temporal variations during the PRD 2006 campaign (factor of $\sim$5 between col. 11 and 17, Table 3.3) as well as for spatial/geographic variations between the Pearl River Delta and other urban regions (factor of 2 between col. 17 and 19, Table 3.3).

3.4 Size-resolved aerosol chemical composition, diurnal cycles, and mixing state

In this section the CCN measurement results as discussed in Sect. 3.3 are compared with other aerosol properties, which are the size-resolved aerosol composition (measured with the AMS; see Sect. 3.2.3), the mixing state of soot particles (measured with the VTDMA; see Sect. 3.2.4), and the single scattering albedo (measured with the Nephelometer and PAS; see Sect. 3.2.5).

For correlation analyses, the time resolution of the AMS, VTDMA, and optical data sets was adjusted to the time resolution of the CCN data. The AMS or VTDMA data point corresponding to a CCN data point was chosen to be the one that is closest in time within a time interval of +/- 10 min (AMS) or +/- 60 min (VTDMA). The optical data were averaged over the time interval of one CCN measurement. If for a CCN data point no corresponding AMS, VTDMA, or optical data point was available, the CCN data point was discarded.

During PRIDE-PRD 2006, CCN data were recorded for six supersaturation (S) levels between 0.068% and 1.27% but two levels (S=0.67% and S=1.27%) were not measured throughout the entire campaign (see Fig. 3.5 a, b). To avoid potential biases due to different averaging times, the data points measured at these S were omitted in the correlation analyses of this section.

Due to the resulting different averaging intervals, the campaign averages calculated in this section

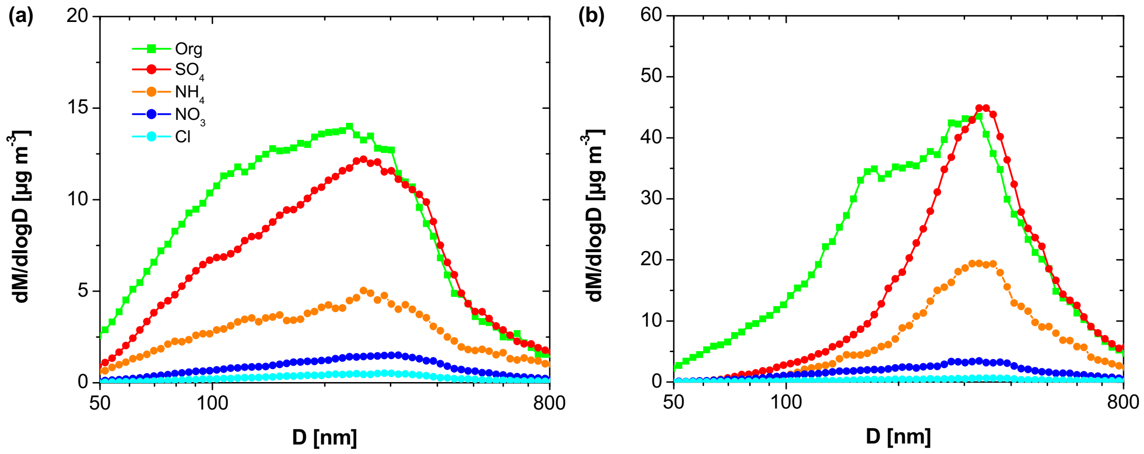

Figure 3.11: Mass size distributions of organic and inorganic compounds determined by aerosol mass spectrometry (AMS) averaged **(a)** over the entire campaign excluding the biomass burning event (BBE), and **(b)** over the BBE.

might differ slightly from those of Sect. 3.3. The CCN data set that was discussed in Sect. 3.3 comprised measurements from 30 June to 30 July 2006. The data set that was taken for the correlation analyses in this section, however, comprised CCN measurements from 12/14 July to 30 July 2006 because of the limited availability of the AMS/VTDMA measurements. Since the second half of July was characterized by two polluted periods (cf. Fig. 3.5), in this section, the average particle hygroscopicity is lower and the average particle number size distribution is shifted to larger sizes compared to the averages shown in Sect. 3.3.

3.4.1 Chemical composition and effective hygroscopicity of CCN-active particles

3.4.1.1 Observations and derivation of κ_{org} and κ_{inorg}

Figure 3.11 shows the average aerosol mass size distribution of organic and inorganic compounds as determined by AMS measurements performed in parallel to the CCN measurements. For the campaign average (excluding the BBE), the organic mass size distribution peaked around 220 nm and the sulfate size distribution slightly above 250 nm with a maximum value of $\sim$13 μg m^{-3} and $\sim$12 μg m^{-3} per logarithmic decade of particle diameter, respectively. The mass size distributions of the other inorganic compounds also peaked around 250 to 300 nm but with much lower concentrations (with ammonia being about one third, nitrate one tenth, and chloride 5% of the sulfate concentration). During the biomass burning event, the mass concentrations of all components were more than three times higher than during the rest of the campaign. The mass size distributions of the inorganic compounds were narrower with a shifted peak to 300 to 350 nm. The mass size distribution of the organic compounds, however, exhibited two separate peaks around 170 nm and 300 nm with a maximum value of $\sim$35 μg m^{-3} and $\sim$40 μg m^{-3} per logarithmic decade of particle diameter, respectively. This means that during the BBE only the organic mass increased for the small particle size range ($<\sim$200 nm) whereas the other substances remained almost the same.

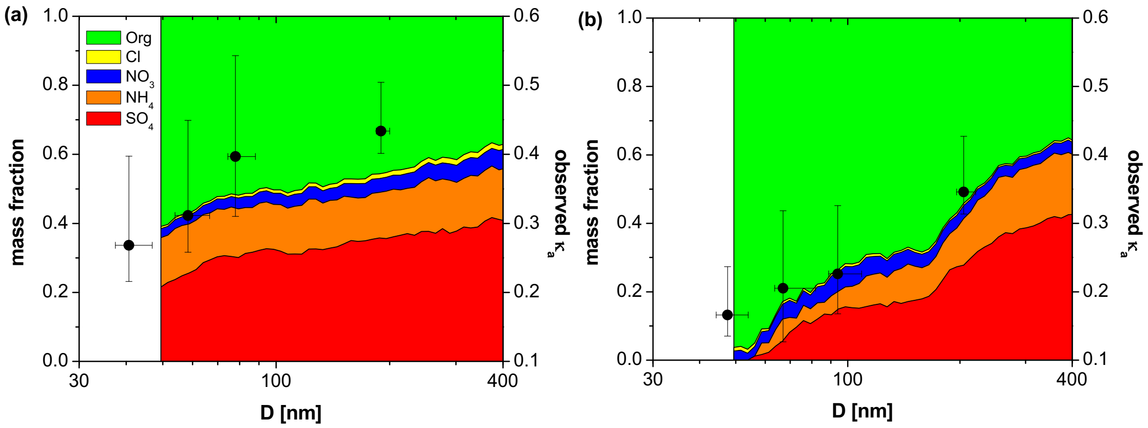

Figure 3.12: Size distributions of mass fractions of organic and inorganic compounds (colored areas) determined by the AMS, and observed effective hygroscopicity parameter of CCN-active particles (κ_a, data points) averaged **(a)** over the entire campaign excluding the BBE, and **(b)** over the BBE. Data points are median values and error bars indicate inter-quartile ranges.

Figure 3.12 shows the size distributions of the mass fractions of chemical compounds averaged over the entire campaign excluding the BBE and averaged over the BBE. For both the averaging periods, the ratio of inorganic to organic mass increased with particle size. The larger particles (>∼200 nm) exhibited an inorganic mass fraction of 50–60% throughout the whole campaign, whereas for the smaller particles (50–200 nm) the mass fractions of chemical compounds during the BBE differed a lot from those during the rest of the campaign (increasing organic mass fraction with decreasing size, up to almost 100% during the BBE and up to only ∼60% during the rest of the campaign). In the same figure, the effective hygroscopicity parameter κ_a is plotted versus the activation diameter D_a (median values and inter-quartile ranges over the two averaging periods). The scale of the κ-axis is chosen so that it matches the scale of the mass fraction according to the expected relationship between hygroscopicity and chemical composition, that is κ=0.1 for aerosol that consists only of organic material and κ=0.6 for aerosol consisting of only inorganic material, as proven e.g. by Gunthe et al. (2009). In Fig. 3.12 b it can be seen that during the BBE, the κ data points lie well on the border between inorganic and organic mass fraction. This can be expected when assuming the simple mixing rule for κ values of different particle components (Gunthe et al., 2009):

$$\kappa_\mathrm{a,p} = \kappa_\mathrm{org} \cdot f_\mathrm{org} + \kappa_\mathrm{inorg} \cdot f_\mathrm{inorg} = 0.1 \cdot f_\mathrm{org} + 0.6 \cdot f_\mathrm{inorg} \tag{3.2}$$

with κ_org and κ_inorg being the effective hygroscopicity parameters for organic and inorganic components, respectively, and f_org and f_org being the organic and inorganic mass fractions, respectively. As shown in the plot of the campaign average excluding the BBE (Fig. 3.12 a), the κ values did not follow the line between inorganic and organic mass fraction as well. The hygroscopicity increased with particle size as the inorganic mass fraction did but κ_a became too high for D>60 nm compared with the expected hygroscopicity. This inconsistency can be partly attributed to the large number of data points with low mass concentrations that go into the campaign average and make the AMS data less reliable. For the BBE, however, this is not the case since the mass concentrations were generally much higher.

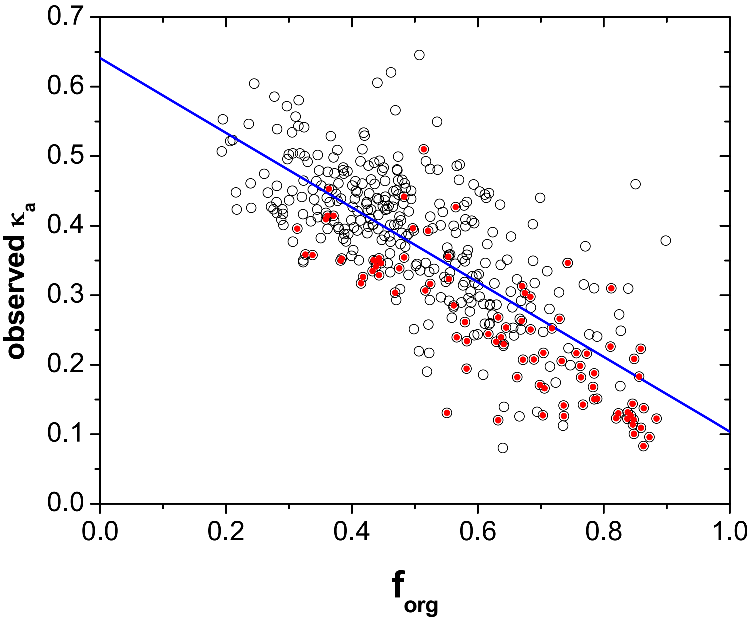

Figure 3.13: Correlation between the observed effective hygroscopicity parameter of CCN-active particles (κ_a) and the organic mass fraction (f_org) determined by size-resolved AMS measurements for the entire campaign. Data points at which $m_\mathrm{D}<1\,\mathrm{g\,m^{-3}}$ are excluded. Red dots indicate the data points measured during the BBE. The blue line is a linear leasts squares fit with the following equation, correlation coefficient, and number of data points: $y = 0.64 - 0.54 \cdot x$, R^2=0.57, n=379.

In order to investigate the relationship between chemical composition and hygroscopicity of the aerosol particles measured in this campaign more specifically, the κ_a values obtained for every measured CCN efficiency spectrum were correlated with the measured organic mass fraction (f_org). When this was performed for all data points only a poor correlation could be found (R^2=0.44). This was most likely due to the large amount of data points at which the mass within the integration interval (m_D, see Sect. 3.2.3) was very low (40% of the data points exhibited $m_\mathrm{D}<1\,\mu\mathrm{g\,m^{-3}}$), which negatively impacted the reliability of f_org. The correlation shown in Fig. 3.13 consists therefore only of data points with $m_\mathrm{D}\geq1\,\mu\mathrm{g\,m^{-3}}$, which improved the fit (R^2=0.57, n=379). Extrapolation of the fit line to f_org=0 yielded $\kappa_\mathrm{inorg}\approx0.6$ for the inorganic fraction, which is characteristic for ammonium sulfate and related compounds (Petters and Kreidenweis, 2007; Rose et al., 2008). Extrapolation of the fit line to f_org=1 yielded $\kappa_\mathrm{org}\approx0.1$ for the organic fraction, which is in agreement with hygroscopicity parameters found for SOA, etc. (King et al., 2009; Gunthe et al., 2009; Dusek et al., 2010).

3.4.1.2 Prediction of κ_a and $N_\mathrm{CCN,S}$

In Fig. 3.14 the κ values predicted from the AMS measurement data ($\kappa_\mathrm{a,p}$, calculated from Eq. (3.2)) are plotted against the κ values derived from the 3-parameter CDF fits to the measured CCN efficiency spectra (κ_a). Note that in this plot all data points are shown including the ones for which $m_\mathrm{D}\leq1\,\mu\mathrm{g\,m^{-3}}$. As expected from the above findings, $\kappa_\mathrm{a,p}$ and κ_a exhibit a weak correlation (R^2=0.44) with a lot of outliers that can, however, be mostly attributed to unreliable AMS data due to low mass concentrations. In fact, in the range between κ=0.25 to 0.55, where ~80% of the data points lie, the predicted deviate from the observed values on average by less than 20%. For smaller values,

Table 3.5: Arithmetic means of the observed κ_{a} and $N_{\mathrm{CCN,S}}$ values, and characteristic deviations between predicted values ($\kappa_{\mathrm{a,p}}$ and $N_{\mathrm{CCN,S,p}}$) and those observed (relative bias and total relative deviation, including systematic and statistical errors). n_κ and n_{N} are the number of data points that are contained in the averages of $\kappa_{\mathrm{a,p}}$ and $N_{\mathrm{CCN,S,p}}$, respectively.

S	κ_{a}	$\kappa_{\mathrm{a,p}}$ (Eq. (3.2))		n_κ	$N_{\mathrm{CCN,S}}$ [cm^{-3}]	$N_{\mathrm{CCN,S,p}}$ with $\kappa_{\mathrm{a,p}}$ [cm^{-3}]		$N_{\mathrm{CCN,S,p}}$ with κ=0.3 [cm^{-3}]		n_{N}
		rel. bias [%]	rel. dev. [%]			rel. bias [%]	rel. dev. [%]	rel. bias [%]	rel. dev. [%]	
0.068	0.42	–7.6	14.3	229	1130	+34.0	34.5	+7.9	19.1	176
0.27	0.36	–2.3	20.5	229	6529	+14.0	16.0	+11.6	19.6	179
0.47	0.28	+15.6	29.1	173	8748	+13.1	14.5	+15.3	16.9	151
all	0.36	+0.7	20.6	631		+20.7	22.0	+11.4	18.6	506

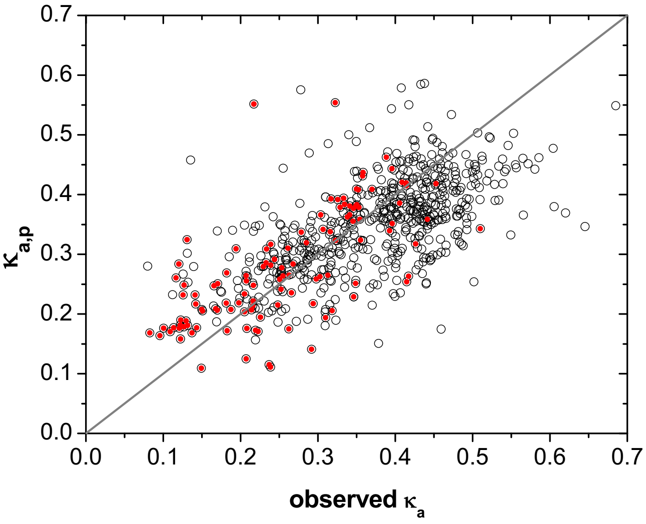

Figure 3.14: Effective hygroscopicity parameters predicted from the organic and inorganic mass fractions determined by AMS measurements ($\kappa_{\mathrm{a,p}}$, Eq. (3.2)) plotted against the values obtained from the CCN measurements (κ_{a}) observed for the entire campaign. Note, that the data points at which m_{D}<1 g m^{-3} are included. Red dots indicate the data points measured during the BBE. The diagonal grey line indicates the 1:1 ratio.

κ_{a} is on average over-predicted (by up to 100% and more), whereas for larger values it is mainly under-predicted (by up to a few tens of percent).

For each data point of Fig. 3.14, the total CCN number concentration ($N_{\mathrm{CCN,S}}$) was calculated by integrating the measured CN size distribution above the critical dry particle diameter for CCN activation that corresponds to the given values of $\kappa_{\mathrm{a,p}}$ and S. In spite of the low correlation of the predicted versus observed κ, the mean relative deviations between the $N_{\mathrm{CCN,S}}$ predicted on the basis of $\kappa_{\mathrm{a,p}}$ ($N_{\mathrm{CCN,S,p}}$, Eq. (3.2)) and the observed values of $N_{\mathrm{CCN,S}}$ were mostly less than 20% with a positive bias on average. This confirms the relatively low sensitivity of $N_{\mathrm{CCN,S}}$ against κ as discussed already in Sect. 3.3.3.3 and 3.3.3.4.

In Tab. 3.5 is shown that the over-prediction becomes larger with decreasing supersaturation, which has been also found in Sect. 3.3.3.3 (Tab. 3.3) and Gunthe et al. (2009). This confirms that the prediction of $N_{\mathrm{CCN,S}}$ is generally less robust at low S, which is due to the enhanced error sensitivity caused by the steep slope of the aerosol size distribution typically observed at the large activation di-

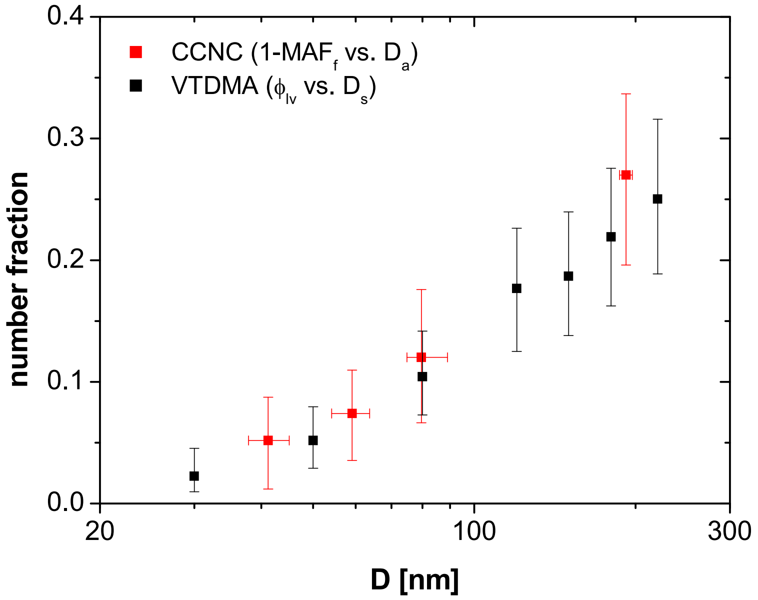

Figure 3.15: Number fraction of particles of low volatility (ϕ_{lv}, black symbols) and of particles that are not CCN-active within the investigated size range (1–MAF$_\mathrm{f}$, red symbols) plotted versus particle size (selected by the VTDMA, D_{VT}, and activation diameter, D_a, respectively). Symbols are median values throughout the campaign, error bars extend to lower and upper quartiles.

ameters corresponding to low supersaturations (Ervens et al., 2007) and also to the stronger influence of externally mixed CCN-inactive particles at large D and low S (Figs. 3.2 and 3.3, Sect. 3.2.2.4).

Table 3.5 also shows the $N_{\mathrm{CCN,S,p}}$ calculated for the same data set using a constant κ of 0.3 (which is the campaign average value for κ_t) as has been done similarly in Sect. 3.3.3.3. It is remarkable that the average deviations between predicted and observed values of $N_{\mathrm{CCN,S}}$ are lower for the constant κ (19%) than when using the composition dependent $\kappa_{\mathrm{a,p}}$ (22%), especially for the smallest supersaturation (19% versus 35% relative deviation). The same result was found by Gunthe et al. (2009) for a data set from pristine tropical rainforest air of Amazonia. It confirms that κ_a is not sufficient to predict $N_{\mathrm{CCN,S}}$ well, if a significant fraction of externally mixed CCN-inactive particles is present as observed for this data set. The parameter κ_a turns out to overestimate the particle hygroscopicity because it describes the effective hygroscopicity of the CCN-active particles only and not the effective hygroscopicity of the ensemble of CCN-active and -inactive particles as the parameter κ_t would do (Sect. 3.2.2.4).

3.4.2 Hygroscopicity and influence of externally mixed soot particles

3.4.2.1 Observations and derivation of κ_{soot}

As described in Sect. 3.3.1.1 and shown in Fig. 3.4, the CCN efficiency spectra at low supersaturations ($S \leq 0.27\%$) observed during PRIDE-PRD2006 did not reach full activation, indicating a substantial portion (1–MAF$_\mathrm{f}$) of externally mixed CCN-inactive particles with much lower hygroscopicity. It was supposed that this fraction most likely comprises freshly emitted (non-aged/non-coated) soot particles with $\kappa \approx 0.01$. In order to proof this suggestion, in this section, the CCN efficiency spectra were compared with the aerosol optical properties and VTDMA measurements.

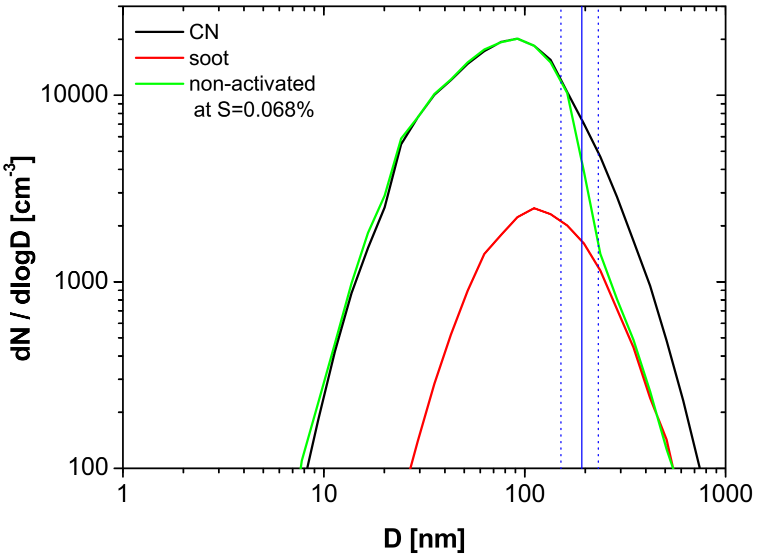

Figure 3.16: Campaign median number size distributions of CN (black), of the externally mixed fresh soot particles (red), and of the non-activated particles at S=0.068% (green). The blue solid line indicated where the median activation diameter D_a is located. The blue dashed lines denote the location of $D_\mathrm{a}-3\sigma_\mathrm{a}$ and $D_\mathrm{a}+3\sigma_\mathrm{a}$.

In Fig. 3.15 the non-activated fraction as obtained from the campaign average CCN efficiency spectra (1–$\mathrm{MAF_f}$) and the number fraction of particles of low volatility obtained from VTDMA measurements (ϕ_lv) characterizing the fresh, uncoated soot particles, are plotted versus the activation diameter (D_a) and the diameter selected by the VTDMA (D_VT), respectively. The figure shows that ϕ_lv increased from 0.02 to 0.25 for particles between 30 to 220nm. The non-activated fraction, 1–$\mathrm{MAF_f}$, followed almost exactly the same trend and increased from 0.05 to 0.27 for particles between 40 to 190 nm.

Figure 3.16 shows the campaign median number size distributions of CN, of the externally mixed fresh soot particles measured by the VTDMA, and of the non-activated particles at S=0.068%. The CN size distribution is monomodal and peaks around 90 nm with a maximum value of 20 000 $\mathrm{cm^{-3}}$ per logarithmic decade of particle diameter. The number size distribution of soot particles peaks around 110 nm with a maximum value of 2500 $\mathrm{cm^{-3}}$. The size distribution of the non-activated particles at S=0.068% follows for particles larger than $D_\mathrm{a}+3\sigma_\mathrm{a}$ exactly the distribution of the soot particles and for particles smaller than $D_\mathrm{a}-3\sigma_\mathrm{a}$ the distribution of CN. In the range between $D_\mathrm{a}+3\sigma_\mathrm{a}$ and $D_\mathrm{a}-3\sigma_\mathrm{a}$ (indicated by the dotted blue vertical lines), the particle activation occurs and thus the size distribution of non-activated particles jumps from following the soot size distribution to following the CN size distribution. This figure indicates that the particles larger ~250 nm that do not activate at S=0.068% represent the freshly emitted soot particles measured by the VTDMA. They do not activate at this supersaturation because they are too hydrophobic. The particles smaller than ~250 nm do not activate not only due to their reduced hygroscopicity but also due to their more strongly curved surface (Kelvin effect, Sect. 1.3).

In Fig. 3.17 a the number fraction of 270 nm particles that activate at S=0.068% ($\mathrm{MAF_m}$) is plotted versus the number fraction of fresh soot particles at 220 nm as determined by the VTDMA. In the CCN measurements the 270 nm size bin was the largest size selected. For all supersaturations,

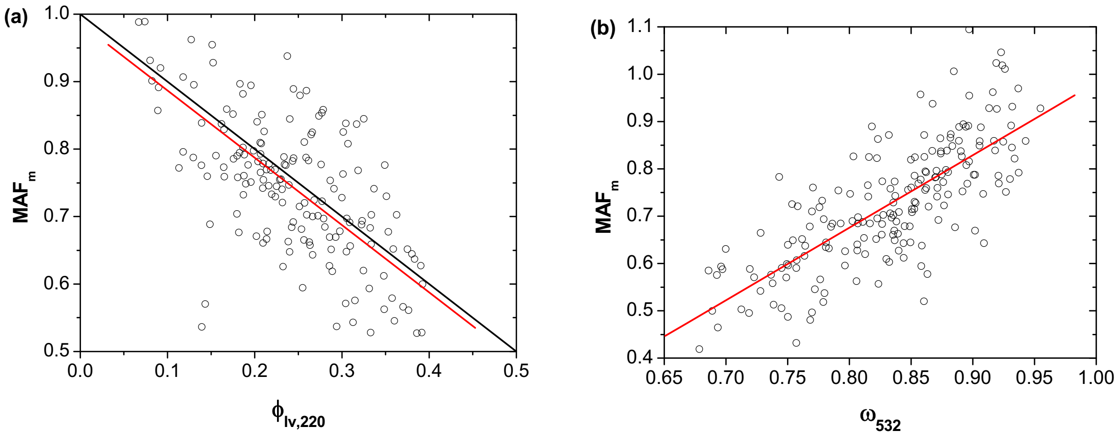

Figure 3.17: Correlation between **(a)** the number fraction of activated particles at 270 nm ($\mathrm{MAF_m}$) for S=0.068% and the number fraction of fresh soot particles at 220($\phi_{\mathrm{lv},220}$) and **(b)** $\mathrm{MAF_m}$ for S=0.068% and the single scattering albedo (ω_{532}).

the measured CCN efficiency spectra were not anymore raising at this size but already approached a plateau, which is referred to as the maximum activated fraction ($\mathrm{MAF_m}$, being the activated fraction measured at 270 nm; cf. Fig. 2.3). It can be regarded as the level at which the externally mixed particles with lower hygroscopicity are not or not fully activated. In the VTDMA measurements the 220 nm size bin is the largest size selected. It can be assumed that ϕ_{lv} measured at this size is comparable to ϕ_{lv} at 270 nm. (This could be proven by extrapolation of the soot size distribution (Fig. 3.16).)

The correlation plot in Fig. 3.17 a shows that $\mathrm{MAF_m}$ decreased with increasing ϕ_{lv} with a linear leasts squares fit (red line) that is close to the 1:1 line. This is another indicator that the particles with a size of 270 nm that did not activate at S=0.068% corresponded to the freshly emitted soot particles at that size, which could be directly measured by the VTDMA. Since they were not activated at 0.068% supersaturation they must have a hygroscopicity of less than κ=0.15 (Eq. (3.1)).

In Fig. 3.17 b $\mathrm{MAF_m}$ is plotted versus the single scattering albedo (see Sect. 3.2.5). ω_{532} is inversely related to the proportion of absorbing material (soot) in the investigated ensemble of aerosol particles. $\mathrm{MAF_m}$ increased with increasing ω_{532} and exhibited a good correlation (R^2=0.57). This confirms that the non-activated fraction is related to the soot content of the aerosol and also suggests that the fraction of externally mixed soot particles is proportional to the total fraction of absorbing material.

Figure 3.18 shows the statistical distributions of the diurnal cycles of $\mathrm{MAF_m}$, $\mathrm{MAF_f}$, $\phi_{\mathrm{lv},220}$, and ω_{532}. All parameters exhibited pronounced cycles indicating a lower fraction of CCN-active particles ($\mathrm{MAF_m}\approx \mathrm{MAF_f}\approx$0.7) and a higher fraction of soot particles ($\phi_{\mathrm{lv},220}\approx$0.3, $\omega_{532}\approx$0.8) during nighttime and a higher fraction of CCN-active particles ($\mathrm{MAF_m}\approx \mathrm{MAF_f}\approx$0.8) and lower fraction of soot particles ($\phi_{\mathrm{lv},220}\approx$0.2, $\omega_{532}\approx$0.9) during daytime.

On the basis of the assumption that the fraction of CCN-inactive particles at 270 nm equals the not (fully) activated fraction of externally mixed soot particles, I want to derive the CCN efficiency spectrum for those soot particles in order to estimate their hygroscopicity. I therefore take the activated fraction at 270 nm measured for every scan and for all supersaturations and subtract the respective

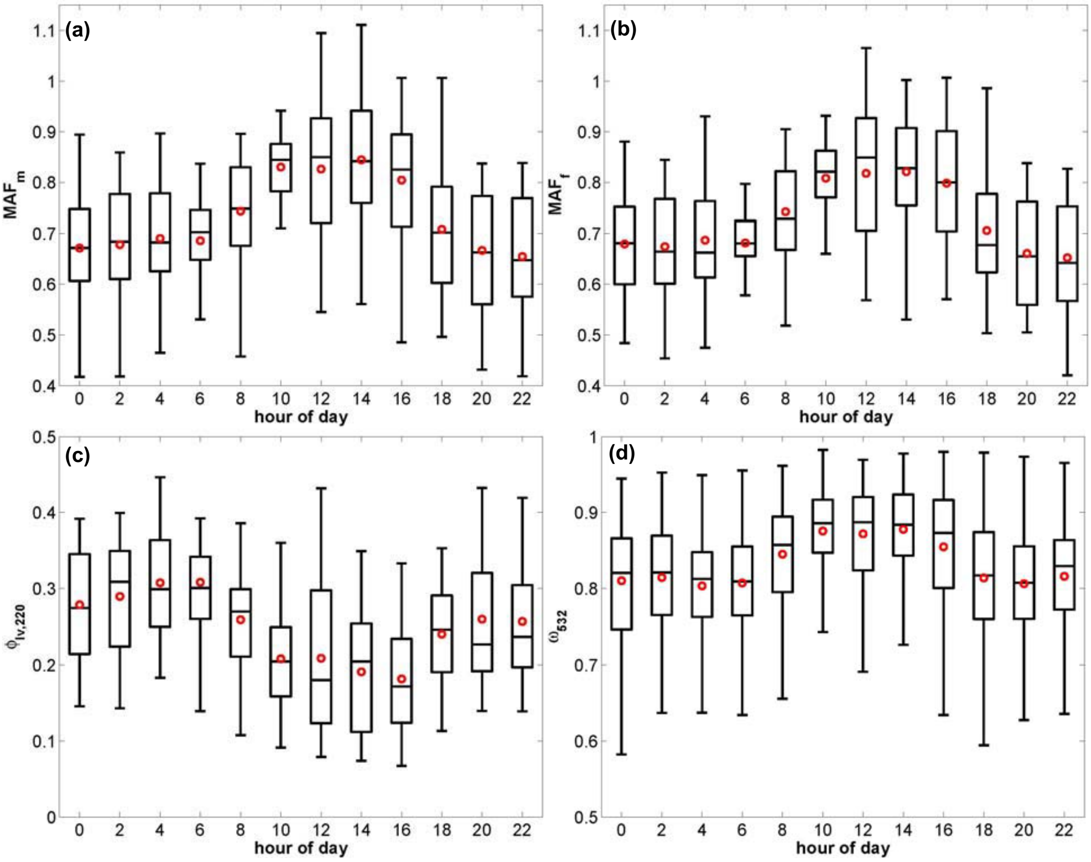

Figure 3.18: Statistical distribution of diurnal cycles of **(a)** the measured and **(b)** the fitted maximum activated fraction at S=0.068% ($\mathrm{MAF_m}$ and $\mathrm{MAF_f}$), **(c)** the number fraction of 220 nm particles of low volatility ($\phi_{\mathrm{lv},220}$), and **(d)** the single scattering albedo ω_{532}. The red dot is the mean value, the horizontal line in the box is the median, the limits of the boxes are the 25th and 75th percentile and the vertical lines extend to 5th and 95th percentiles.

$\phi_{\mathrm{lv},220}$ so that the CCN efficiency spectrum of soot particles calculates as follows:

$$\left(\frac{N_{\mathrm{CCN}}}{N_{\mathrm{CN}}}\right)_{\mathrm{soot}} = \frac{\mathrm{MAF_m} - (1 - \phi_{\mathrm{lv},220})}{\phi_{\mathrm{lv},220}} \tag{3.3}$$

In Fig. 3.19 the campaign median values of the CCN efficiency spectrum of soot particles calculated according to Eq. (3.3) are plotted versus the supersaturation. The data point at the lowest supersaturation is slightly below zero and the other values spread from 0.7 to 1.0. To obtain the critical supersaturation the data points were fitted with a CDF. It is difficult to provide a good fit through these data points because there was only one point that lay on the slope of the CDF.

Nevertheless, the free fit through the median values yielded a critical supersaturation (S_{c}) of 0.26 corresponding to a κ value of 0.009 (Eq. (3.1)). (The fit through all data points yielded S_{c}=0.25% corresponding to κ=0.010.) Even if this value might exhibit a large uncertainty, it is sure that the critical supersaturation must be between 0.068% and 0.27%. This would result in a κ range of 0.15 to 0.008 for the hygroscopicity of the soot particles (Eq. (3.1)).

To get a best estimate for κ the data points in Fig. 3.19 were fitted keeping $\mathrm{MAF_f}$ constant to the value of the free fit and varying σ so that the data point at S=0.068% is just zero. According to this fitting the hygroscopicity parameter for the soot particles (κ_{soot}) would calculate to be 0.011.

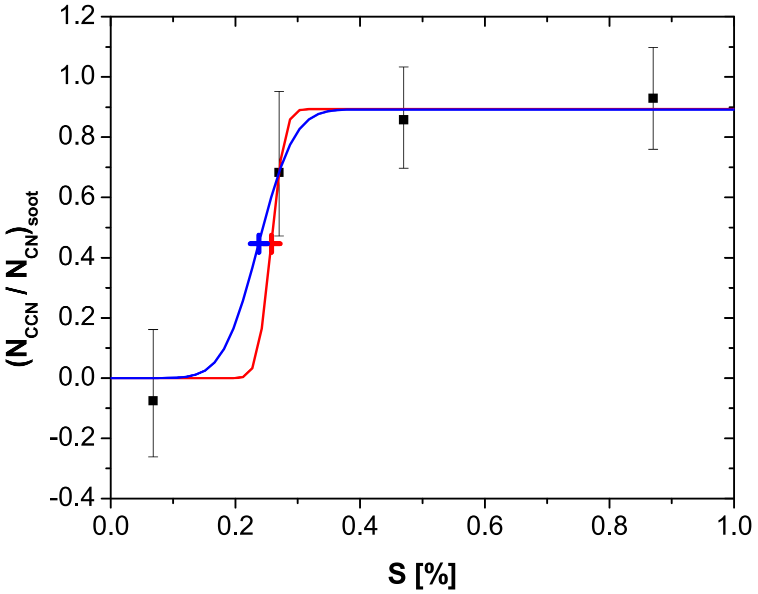

Figure 3.19: CCN efficiency spectrum of externally mixed fresh soot particles. Black data points are median values of the data points calculated by Eq. (3.3), errpr bars extend to their lower and upper quartiles. The red line is a free fit of a 3-parameter CDF to the black data points and the red cross is the point of the critical supersaturation obtained from the fit. The blue line and cross are the best estimates for the CDF fit and the respective critical supersaturation.

3.4.2.2 Prediction of κ_{t} and $N_{\mathrm{CCN,S}}$

With the derived hygroscopicity for soot particles $\kappa_{\mathrm{soot}}\approx 0.01$ and the CCN measurement results I infer the effective hygroscopicity of CCN-active and -inactive particles (κ_{t}) as follows:

$$\kappa_{\mathrm{t,p}}(\mathrm{CCN}) = \kappa_{\mathrm{a}} \cdot \mathrm{MAF_m} + \kappa_{\mathrm{soot}} \cdot (1 - \mathrm{MAF_m}) \tag{3.4}$$

in which κ_{a} is the observed effective hygroscopicity of CCN-active particles and $\mathrm{MAF_m}$ the number fraction of CCN-active particles at 270 nm.

In Fig. 3.20 a the predicted κ_{t} values are plotted versus the measured ones. The two variables exhibited a very good correlation (R^2=0.94), whereby κ was slightly over-estimated for small values and slightly under-estimated for large values. This plot shows that κ_{t} can be successfully derived from knowledge of the effective hygroscopicity of CCN-active (κ_{a}) and -inactive particles (κ_{soot}) on the assumption that 1–$\mathrm{MAF_m}$ comprises the fraction of CCN-inactive particles. It confirms that κ_{t} is indeed a suitable proxy for the effective hygroscopicity of an external mixture of CCN-active and -inactive particles (see Rose et al., 2010b).

Assuming that the fraction of CCN-inactive particles equals the fraction of soot particles (1–$\mathrm{MAF_m}\approx\phi_{\mathrm{lv}}$), I infer the effective hygroscopicity of CCN-active and -inactive particles (κ_{t}) as follows:

$$\kappa_{\mathrm{t,p}}(\mathrm{VT}) = \kappa_{\mathrm{a}} \cdot (1 - \phi_{\mathrm{lv,D_a}}) + \kappa_{\mathrm{soot}} \cdot \phi_{\mathrm{lv,D_a}} = \kappa_{\mathrm{a}} - \phi_{\mathrm{lv,D_a}} \left(\kappa_{\mathrm{a}} - \kappa_{\mathrm{soot}}\right) \tag{3.5}$$

in which κ_{a} is the observed effective hygroscopicity of CCN active particles and $\phi_{\mathrm{lv,D_a}}$ the number fraction of fresh soot particles with D_{VT} close to the activation diameter D_{a}.

In Fig. 3.20 b the κ_{t} values predicted with Eq. (3.5)are plotted versus the measured ones. The two variables exhibited still a very good correlation (R^2=0.89), with κ being slightly over-estimated

Table 3.6: Arithmetic means of the observed κ_t and $N_\mathrm{CCN,S}$ values, and characteristic deviations between predicted values ($\kappa_\mathrm{t,p}$ and $N_\mathrm{CCN,S,p}$) and those observed (relative bias and total relative deviation, including systematic and statistical errors). n_κ and $\mathrm{n_N}$ are the number of data points that are contained in the averages of $\kappa_\mathrm{t,p}$ and $N_\mathrm{CCN,S,p}$, respectively. Note that comparable values from Tab. 3.5 might differ from the ones in this table due to different averaging periods.

S	κ_t	$\kappa_\mathrm{t,p}$(VT,AMS), Eq. (3.6)		n_κ	$N_\mathrm{CCN,S}$ [cm^{-3}]	$N_\mathrm{CCN,S,p}$ with $\kappa_\mathrm{t,p}$(VT,AMS) [cm^{-3}]		$N_\mathrm{CCN,S,p}$ with κ=0.3 [cm^{-3}]		$\mathrm{n_N}$
		rel. bias [%]	rel. dev. [%]			rel. bias [%]	rel. dev. [%]	rel. bias [%]	rel. dev. [%]	
0.068	0.32	+1.0	14.6	155	1214	+10.5	15.2	+8.0	18.2	116
0.27	0.33	−1.4	21.5	150	7069	+7.8	11.3	+10.3	19.3	114
0.47	0.27	+10.4	26.3	104	9268	+10.2	12.4	+15.7	16.7	90
all	0.31	+2.5	20.1	409		+9.4	13.0	+11.0	18.2	320

for small values and slightly under-estimated for large values. It shows that κ_t can be successfully derived from knowledge of the effective hygroscopicity of CCN-active (κ_a) and -inactive particles (κ_soot), and the mixing state. Note, that the relative deviation between the predicted and the measured κ_t became a little larger when MAF decreased but not when ϕ_lv increased.

In the next step I predict the effective hygroscopicity of an ensemble of CCN-active and -inactive particles (κ_t) only from information about the size-resolved chemical composition of the particles and the mixing state, i.e., I use the AMS and VTDMA measurement results but no CCN data. κ_t is then calculated by:

$$\kappa_\mathrm{t,p}(\mathrm{VT,AMS}) = \kappa_\mathrm{a,p} \cdot (1 - \phi_\mathrm{lv,D_a}) + \kappa_\mathrm{soot} \cdot \phi_\mathrm{lv,D_a} = \kappa_\mathrm{a,p} - \phi_\mathrm{lv,D_a} \left(\kappa_\mathrm{a,p} - \kappa_\mathrm{soot}\right) \tag{3.6}$$

in which $\kappa_\mathrm{a,p}$ is calculated from f_org and f_inorg by Eq. (3.2).

Figure 3.20 c shows κ_t calculated with Eq. (3.6) plotted versus the observed κ_t. It can be seen that the prediction of κ_t only from data of the chemical composition and mixing state was less successful since only a moderate correlation (R^2=0.52) could be found. In the range between κ=0.25 to 0.55, where 70% of the data points lay, the predicted deviated from the observed value on average by less than 20%. For smaller values, κ was on average over-predicted (by up to 100% and more), whereas for larger values it was mainly under-predicted (by up to a few tens of percent). Table 3.6 shows that the deviations increased with supersaturation. However, the deviations were independent of MAF (not shown here).

In analogy to the calculation in Sect. 3.4.1.2, $N_\mathrm{CCN,S}$ was determined from the predicted κ_t values. In spite of the low correlation of predicted versus measured κ values, the relative deviations between $N_\mathrm{CCN,S}$ predicted on the basis of $\kappa_\mathrm{t,p}(\mathrm{VT,AMS})$ and the observed values of $N_\mathrm{CCN,S}$ were on average 13% with a positive bias in summary (Tab. 3.6). Other than found for the prediction using $\kappa_\mathrm{a,p}$ (Eq. (3.2), Tab. 3.5), the deviations increased not for the smaller supersaturations.

When calculating $N_\mathrm{CCN,S}$ for the same data set using a constant κ of 0.3, the relative deviations between the predicted and observed values of $N_\mathrm{CCN,S}$ were larger (∼18% on average) than when calculated with $\kappa_\mathrm{t,p}(\mathrm{VT,AMS})$. This is in contrast to what was found in Sect. 3.4.1 (more exact prediction of $N_\mathrm{CCN,S}$ using a constant κ=0.3 than using individual $\kappa_\mathrm{a,p}$) and it confirms the findings of Sect. 3.3.3: κ_t is a better proxy for the prediction of $N_\mathrm{CCN,S}$ than κ_a, if the aerosol consists of a fraction of CCN-active and a fraction of CCN-inactive particles with much lower hygroscopicity.

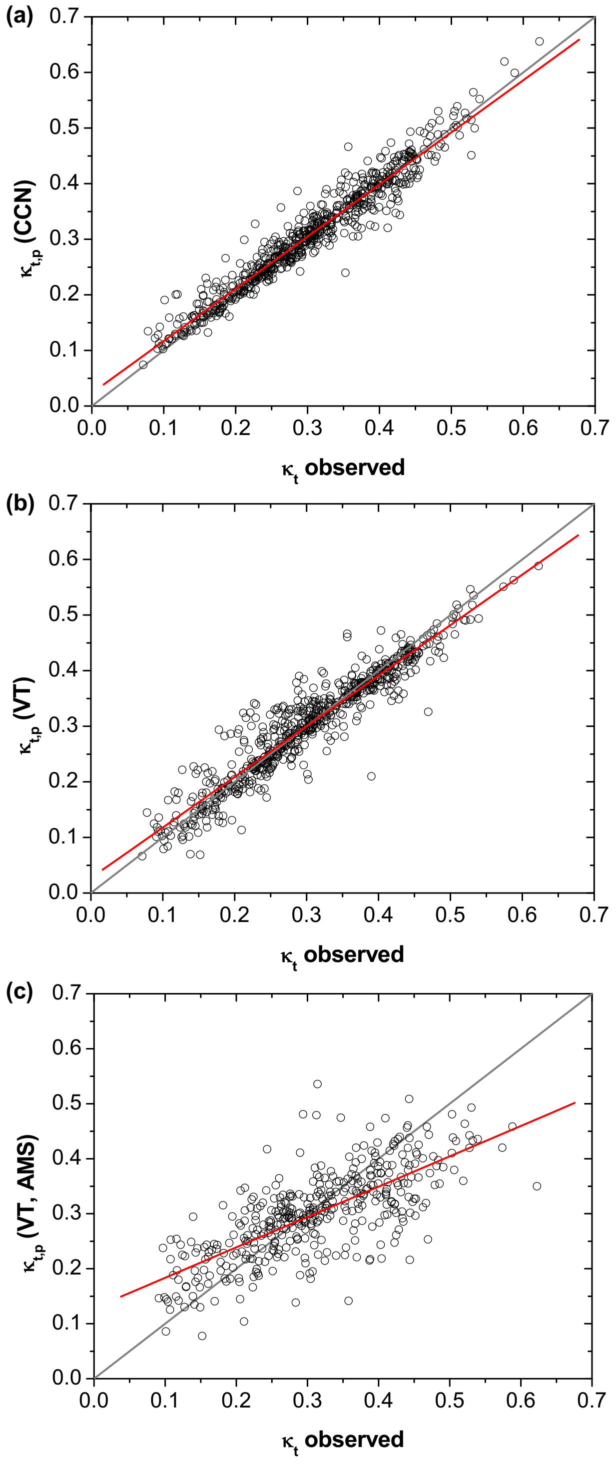

Figure 3.20: Correlation plot of **(a)** the predicted κ_t as calculated from the CCN data ($\mathrm{MAF_m}$) and Eq. (3.4) ($\kappa_\mathrm{t,p}(\mathrm{CCN})$) versus the observed κ_t, **(b)** the predicted κ_t as calculated from the VTDMA data ($\phi_\mathrm{lv,220}$) and Eq. (3.5) ($\kappa_\mathrm{t,p}(\mathrm{VT})$) versus the observed κ_t, and **(c)** the predicted κ_t as calculated from the VTDMA data ($\phi_\mathrm{lv,220}$), AMS data (f_org, f_inorg), and Eq. (3.6) ($\kappa_\mathrm{t,p}(\mathrm{VT, AMS})$) versus the observed κ_t. The grey lines are the 1:1 lines and the red lines are linear leasts squares fit lines through the data points: **(a)** R^2=0.94, y=0.02+0.94 x, n=656; **(b)** R^2=0.89, y=0.03+0.91 x, n=656; and **(c)** R^2=0.52, y=0.13+0.55 x, n=409.

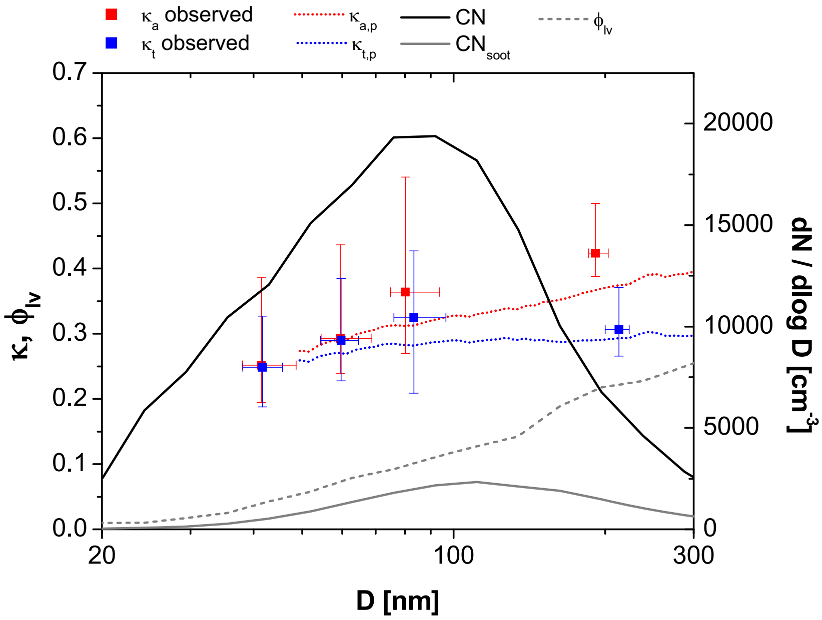

Figure 3.21: Comparison of the predicted (red and blue lines, left axis) and measured (red and blue data points, left axis) hygroscopicity parameters. Supporting lines are the number size distribution of CN (solid black, right axis), of soot particles (solid grey, right axis), and of the fraction of soot particles (dashed grey, left axis) averaged over the campaign. Lines and data points are median values, and error bars indicate the interquartile ranges of the corresponding data points.

Moreover, a constant average value of κ_{t}=0.3 is a good approximation, if no information on particle composition is available, but cannot account for the observed temporal variations in aerosol composition and CCN properties.

Figure 3.21 shows the campaign average size distribution of the predicted κ_{a} and κ_{t} and the average measured κ_{a} and κ_{t} versus the activation diameter as observed at the four selected supersaturations. $\kappa_{\mathrm{a,p}}$ was calculated by Eq. (3.2) using the average size distribution of the organic and inorganic mass fractions. $\kappa_{\mathrm{t,p}}$ was calculated by Eq. (3.6) using the size distribution of $\kappa_{\mathrm{a,p}}$ and ϕ_{lv} calculated from the average CN and soot size distribution. Below 70 nm, κ_{a} and κ_{t} were almost the same for both the measured and the predicted values, but with increasing particle size κ_{a} became significantly larger than κ_{t}. This can be explained by the increasing fraction of externally mixed soot particles with particle size as indicated by the grey dashed line in Fig. 3.21 because κ_{t} is the combination of the hygroscopicity of the CCN-active particles (κ_{a}) and the much lower hygroscopicity of the soot particles (κ_{soot}).

For κ_{t}, the measured values were only slightly higher than the predicted ones but for κ_{a} the measured values differed a lot for D>70 nm. As observed already in Fig. 3.14, κ_{a} was significantly under-predicted for larger κ values, which were typically observed for larger particle sizes (~15% under-prediction for particles ≥70 nm). Since the variability of mass concentrations was relatively little at these sizes, this result suggests that the discrepancy between measured and predicted κ_{a} is not likely to be due to unreliable AMS data. It rather suggests that the effective hygroscopicity of the inorganic and/or organic fraction (κ_{inorg} and/or κ_{org}) seemed to be size-dependent (increased κ_{inorg} and/or κ_{org} with increasing particle size).

3.5 Conclusions

In this chapter the CCN measurement results of the PRIDE-PRD2006 campaign were presented.

The measured CCN efficiency spectra (activation curves) could be described by cumulative Gaussian distribution functions, from which characteristic hygroscopicity parameters (κ) could be derived. These κ parameters describe the influence of particle composition on CCN activity. The parameter κ_a characterizes the average hygroscopicity of CCN-active particles, whereas the parameter κ_t is an approximate measure (proxy) for the effective hygroscopicity of the total ensemble of CCN-active and -inactive particles. Both of these parameters were consistent with AMS and/or VTDMA measurement data.

The dry CCN activation diameters measured during PRIDE-PRD2006 at S=0.068–1.27% were in the range of 200–30 nm and the effective hygroscopicity parameters varied in the range of 0.1–0.5. The mean value of κ_t characterizing the hygroscopicity of all aerosol particles averaged over the whole campaign and investigated size range was 0.3, which equals the average value of κ observed or inferred for other continental locations (Andreae and Rosenfeld, 2008; Pöschl et al., 2009). Particles in the Aitken size range ($D\approx$30–70 nm, $\kappa_\mathrm{a}\approx\kappa_\mathrm{t}\approx$0.28) were on average less hygroscopic than particles in the accumulation size range ($D\approx$70–200 nm, $\kappa_\mathrm{t}\approx$0.33, $\kappa_\mathrm{a}\approx$0.41).

The hygroscopicity parameters derived from the CCN measurements were consistent with AMS measurement data showing that the organic mass fraction (f_org) was on average as high as 60% in the Aitken mode and a little lower in the accumulation mode (40–50%). Extrapolation of the negative linear correlation between κ_a and f_org yielded the following κ values for organic and inorganic particle components: $\kappa_\mathrm{org}\approx$0.1, which can be regarded as the effective hygroscopicity of secondary organic aerosol (SOA) and $\kappa_\mathrm{inorg}\approx$0.6, which is characteristic for ammonium sulfate and related salts.

During a strong local biomass burning event (BBE) the mass concentrations of all chemical compounds were more than three times higher than during the rest of the campaign. f_org was little higher in the accumulation mode and increased to almost 100% for the smallest particles ($\sim$50 nm.) Accordingly, the aerosol particles were generally less CCN active ($\kappa_\mathrm{t}\approx$0.2). Due to the very intense local sources and high level of pollution, the κ values observed during the BBE can be regarded as characteristic for freshly emitted smoke from the open burning of agricultural waste.

At low S($\leq$0.27%), the maximum activated fraction (MAF) remained generally well below one, which indicates substantial portions of externally mixed CCN-inactive particles with much lower hygroscopicity. At S=0.068%, the average MAF$_\mathrm{f}$ was only $\sim$0.75 with minimum values as low as $\sim$0.4, i.e., even at diameters as large as $\sim$250 nm an average of $\sim$25% up to $\sim$60% of the aerosol particles were not CCN-active. To my knowledge such high portions of externally mixed CCN-inactive particles have not been observed before in atmospheric aerosols. Note, however, that these CCN-inactive particles contributed only around $\sim$3% to the total aerosol particle number concentration. The integral CCN efficiencies at moderate supersaturations ($N_\mathrm{CCN,S}/N_\mathrm{CN,tot}\approx$0.36–0.53 at S=0.27%–0.47%, Tab. 3.2) were even slightly higher than the global average value reported by Andreae (2009) ($N_\mathrm{CCN,S}/N_\mathrm{CN,tot}\approx$0.36 at S=0.4%).

From correlation of the CCN data with the single scattering albedo and with the fraction of particles of low volatility obtained with VTDMA measurements it could be concluded that those externally mixed particles with lower hygroscopicity represent the fraction of externally mixed fresh soot particles. The estimation of the effective hygroscopicity of these soot particles yielded κ_{soot}≈0.01.

From the measured CCN efficiency spectra and total aerosol particle (CN) size distributions, CCN size distributions and total CCN number concentrations ($N_{\mathrm{CCN,S}}$) were derived. On average, $N_{\mathrm{CCN,S}}$ ranged from $1000\,\mathrm{cm}^{-3}$ at S=0.068% to $16\,000\,\mathrm{cm}^{-3}$ at S=1.27%, representing ∼6% to ∼85% of the total aerosol particle number concentration ($N_{\mathrm{CN,tot}}$). During the biomass burning event, the CN size distribution was broader and the maximum was shifted to larger sizes (from ∼70 nm to ∼120 nm). The average number concentration of CN was slightly smaller (∼$1.5\times10^4\,\mathrm{cm}^{-3}$ vs. ∼$1.8\times10^4\,\mathrm{cm}^{-3}$), but due to the larger average particle sizes the CCN concentrations at low supersaturation were substantially higher (+100% at S=0.068%, +10% at S=0.27%). For high supersaturations ($S\geq$0.47%), however, $N_{\mathrm{CCN,S}}$ decreased by up to ∼25% compared to the rest of the campaign.

Based on the measurement data, I have tested different model approaches (power laws and κ-Köhler models) for the approximation/prediction of $N_{\mathrm{CCN,S}}$ as a function of water vapor supersaturation, aerosol particle number concentration, size distribution and hygroscopicity. Depending on S and on the applied type of power law or hygroscopicity parameter, the relative deviations between observed and predicted $N_{\mathrm{CCN,S}}$ can range from a few percent to several hundred percent. The largest deviations occurred at low S with power laws based on particle number concentration without size information. Much better predictions could be made when using measured aerosol size distributions in combination with κ-Köhler models.

With variable κ values obtained from individual CCN efficiency spectra, the relative deviations between observed and predicted $N_{\mathrm{CCN,S}}$ were on average less than ∼10% and rarely exceeded 20%.

When using κ values obtained from AMS-based organic and inorganic mass fractions ($\kappa_{\mathrm{a,p}}$) the predicted $N_{\mathrm{CCN,S}}$ were only in fair agreement with the measurement results (mostly less than 20% average deviation).This confirms that κ_{a} is not sufficient to predict $N_{\mathrm{CCN,S}}$ well, if a significant fraction of externally mixed CCN-inactive particles is present as observed for this data set.

From a combination of the AMS based $\kappa_{\mathrm{a,p}}$, the VTDMA based ϕ_{lv}, and κ_{soot}, the effective hygroscopicity of an external mixture of CCN-active and -inactive particles could be predicted ($\kappa_{\mathrm{t,p}}$). The prediction of $N_{\mathrm{CCN,S}}$ with $\kappa_{\mathrm{t,p}}$ was much better than with $\kappa_{\mathrm{a,p}}$ (10% average deviation) confirming that the information on the mixing state is important to sufficiently predict CCN concentrations only from the knowledge of chemical composition.

These results confirm the applicability of the κ-Köhler model approach for efficient description of the CCN properties of atmospheric aerosols. Note, however, that in the case of externally mixed CCN-active and -inactive aerosol particles, the use of κ parameters derived from different types of fits to the measured CCN efficiency spectra (2- or 3-parameter CDF) can lead to substantially different results – especially at low S (increase of deviations by up to a factor of ∼4).

Assuming a constant average value of κ=0.3, the deviations were on average still less than ∼20%, which confirms that κ=0.3 may be suitable as a first-order approximation for the effective hygroscopicity and CCN activity of continental aerosols. Model calculations assuming constant particle number concentrations and size distributions led to substantially larger deviations (∼70% to ∼140%).

These findings confirm earlier studies suggesting that aerosol particle number and size are the major predictors for the variability of the CCN concentration in continental boundary layer air, followed by particle composition and hygroscopicity as relatively minor modulators (Gunthe et al., 2009; Pöschl et al., 2009). Thus the influence of aerosol chemical composition and hygroscopicity appears to be less variable and less uncertain than other factors that determine the effects of aerosols on warm cloud formation in the atmosphere (e.g., particle number concentration, size distribution, sources, sinks, and meteorological conditions). Depending on the required and applicable level of detail, the information and parameterizations presented in this study should enable efficient description of the CCN activity of atmospheric aerosols in detailed process models as well as in large-scale atmospheric and climate models (Heintzenberg and Charlson, 2009).

4 Summary and conclusions

The main findings and conclusions of this thesis and related publications, to which the underlying PhD work contributed, can be summarized as follows.

Reliable CCN measurements require experimental calibration of the water vapor supersaturation in the applied instrument, using well-defined model aerosols like ammonium sulfate or sodium chloride. Careful calibration is particularly important at low supersaturation levels, and flow model calculations may help to extrapolate but cannot replace the results of calibration experiments. A comprehensive comparison and uncertainty analysis of various Köhler models and thermodynamic parameterizations commonly used in CCN studies showed that the relative deviations in supersaturation are as high as 25% for ammonium sulfate and 12% for sodium chloride. The deviations are mainly caused by different parameterizations for the activity of water in aqueous solutions of the salts. The Aerosol Inorganics Model (AIM) and equivalent parameterizations appear best suited to serve as accurate reference standards. In any case, CCN studies should always report exactly which Köhler model equations and parameters were used to ensure comparability of the results.

Test experiments showed that the conditions of particle generation and drying are important because they can affect the shape and microstructure of the calibration aerosol particles (especially of NaCl). A comparison with other CCN instruments during the LExNo laboratory campaign corroborated the high accuracy and precision of the instrument and the measurement procedures developed and applied in this thesis. Experiments with test aerosols of complex chemical composition confirmed the consistency of observations and multi-component Köhler modeling.

The mean CCN number concentrations observed in polluted mega-city air and biomass burning smoke in the Pearl River Delta, China (PRIDE-PRD2006) ranged from $1000\,\mathrm{cm}^{-3}$ at S=0.068% to $16\,000\,\mathrm{cm}^{-3}$ at S=1.27%, which are among the highest values ever observed and about two orders of magnitude higher than at remote continental locations (Jungfraujoch (CLACE-5, CLACE-6), Amazon (AMAZE-08)). Nevertheless, the ratios between CCN concentration and total aerosol particle concentration (integral CCN efficiencies) were similar to the ratios observed in remote continental air ($\sim$6% to $\sim$85% at S=0.068% to 1.27% for a total particle number concentration of $\sim 18\,000\,\mathrm{cm}^{-3}$).

The measured CCN efficiency spectra (activation curves) could be described by cumulative Gaussian distribution functions, from which characteristic hygroscopicity parameters could be derived. These κ parameters, which describe the influence of particle composition on CCN activity, increased with particle size and were in the range of 0.1 to 0.5 with an overall average value of $\kappa\approx$0.3. Both the temporal variability and the size-dependence of the effective hygroscopicity of CCN-active particles could be parameterized as a function of organic and inorganic mass fractions determined by aerosol mass spectrometry (AMS). The characteristic κ values of organic and inorganic components were similar to those observed in other regions of the world: $\kappa_{\mathrm{org}}\approx$0.1 and $\kappa_{\mathrm{inorg}}\approx$0.6.

At low supersaturation ($S\leq$0.27%), the maximum activated fraction of the CCN efficiency spectra observed during PRIDE-PRD2006 remained generally well below one, indicating substantial portions of externally mixed CCN-inactive particles with much lower hygroscopicity (up to $\sim$60% at $\sim$250 nm). Comparison of these results with other aerosol properties (volatility and optical properties) suggest that these particles were fresh soot particles ($\kappa_{\mathrm{soot}}\approx$0.01).

The observed CCN number concentrations ($N_{\mathrm{CCN,S}}$) could be efficiently predicted using a simple

κ-Köhler model with a single proxy for the effective average hygroscopicity of the aerosol. Note, however, that different types of κ-parameters have to be distinguished for external mixtures of CCN-active and -inactive aerosol particles: κ_{a} for the CCN-active particles, and κ_{t} for the total ensemble of CCN-active and -inactive particles. Using individual κ_{a} values derived from the measured organic and inorganic mass fraction (AMS data) and individual particle number size distributions, the relative deviations between predicted and observed $N_{\mathrm{CCN,S}}$ were $\sim$20%. Including information about the mixing state and the hygroscopicity of the soot particles (κ_{t}), the relative deviations between predicted and observed $N_{\mathrm{CCN,S}}$ were $\sim$10%.

When a constant average value of κ=0.3 and individually measured particle number size distributions were taken for approximation of $N_{\mathrm{CCN,S}}$, the average relative deviations from the observed $N_{\mathrm{CCN,S}}$ were <15%. In contrast, model calculations using variable κ values as measured (derived from CCN efficiency spectra) and constant size distributions led to much higher deviations: $\sim$70% for the campaign average size distribution, $\sim$80% for a generic rural size distribution, and $\sim$140% for a generic urban size distribution. These findings confirm earlier studies suggesting that aerosol particle number and size are the major predictors for the variability of the CCN concentration in continental boundary layer air, followed by particle composition and hygroscopicity as relatively minor modulators. In order to perform highly accurate predictions of $N_{\mathrm{CCN,S}}$, however, not only the particle composition but also the mixing state is important to know.

The CCN properties measured during CAREBeijing (mega-city air near Beijing, China) and CLACE-5 (high-alpine air on the Jungfraujoch, Switzerland) were similar to those found for the PRIDE-PRD2006 campaign, although these sites exhibited very different levels of pollution (average total particle number concentrations of $17\,000\,\mathrm{cm}^{-3}$ vs. $420\,\mathrm{cm}^{-3}$, respectively). The effective hygroscopicity increased with particle size, and the overall average hygroscopicity parameter was $\kappa\approx0.3$. In both campaigns, externally mixed particles with much lower hygroscopicity were observed, but their fractions were lower than during PRIDE-PRD2006 ($\sim$20% for CAREBeijing and $\sim$15% for CLACE-5). First simulations of the global distribution of κ with an atmospheric chemistry model (Pringle et al., 2010) are consistent with the field measurement results of this and related recent studies. They confirm that the observed average value of $\kappa\approx0.3$ can be regarded as an approximate global average effective hygroscopcity parameter of CCN in continental air.

The κ values determined by field measurements of aerosol chemical composition or CCN activity can be directly implemented in cloud models (Reutter et al., 2009), which is more realistic than equivalent model salt aerosols as used in earlier approaches. Sensitivity studies with a cloud parcel model showed that within the range of effective hygroscopicity parameters characteristic for continental atmospheric aerosols (κ=0.1–0.5), the number of cloud droplets formed in convective updrafts depends rather weakly on the actual value of κ. In accordance with the Köhler model predictions of CCN number concentration as outlined above, the cloud parcel model calculations also indicated that changes in aerosol particle number concentration and size distribution have a stronger influence than changes in particle hygroscopicity. Depending on the required and applicable level of detail, the information and parameterizations presented in this study should enable efficient description of the CCN activity of atmospheric aerosols in detailed process models as well as in large-scale atmospheric and climate models.

Appendix

A Related publications

The following scientific publications include contributions from the research work performed within the PhD studies underlying this thesis (measurements, modeling, and interpretation).

Rose, D., Gunthe, S. S., Mikhailov, E., Frank, G. P., Dusek, U., Andreae, M. O., and Pöschl, U.: Calibration and measurement of a continuous-flow cloud condensation nuclei counter (DMT-CCNC): CCN activation of ammonium sulfate and sodium chloride aerosol particles in theory and experiment, Atmos. Chem. Phys., 8, 1153–1179, 2008.

Rose, D., Nowak, A., Achtert, P., Wiedensohler, A., Hu, M., Shao, M., Zhang, Y., Andreae, M. O., and Pöschl, U.: Cloud condensation nuclei in polluted air and biomass burning smoke near the mega-city Guangzhou, China – Part 1: Size-resolved measurements and implications for the modeling of aerosol particle hygroscopicity and CCN activity, Atmos. Chem. Phys., 10, 3365–3383, 2010.

Rose, D., Garland, R. M., Yang, H., Gunthe, S. S., Berghof, M., Wehner, B., Wiedensohler, A., Takegawa, N., Kondo, Y., Andreae, M. O., and Pöschl, U.: Cloud condensation nuclei in polluted air and biomass burning smoke near the mega-city Guangzhou, China – Part 2: Size-resolved aerosol chemical composition, diurnal cycles, and mixing state of CCN-inactive soot particles, Atmos. Chem. Phys. Discuss., to be submitted, 2010.

Rose, D. et al.: Size-resolved measurements of cloud condensation nuclei (CCN) at a high alpine observatory, Jungfraujoch, during the CLACE-5 campaign, in preparation, 2010.

Rose, D. et al.: Size-resolved measurements of cloud condensation nuclei (CCN) near the mega-city Beijing, China, in preparation, 2010.

Dusek, U., Frank, G. P., Curtius, J., Drewnick, F., Schneider, J., Kürten, A., **Rose, D.**, Andreae, M. O., Borrmann, S., , and Pöschl, U.: Enhanced organic mass fraction and decreased hygroscopicity of cloud condensation nuclei (CCN) during new particle formation events, Geophys. Res. Lett., 37, doi:10.1029/2009GL040930, 2010.

Garland, R. M., Yang, H., Schmid, O., **Rose, D.**, Nowak, A., Achtert, P., Wiedensohler, A., Takegawa, N., Kita, K., Miyazaki, Y., Kondo, Y., Hu, M., Shao, M., Zeng, L. M., Zhang, Y. H., Andreae, M. O., and Pöschl, U.: Aerosol optical properties in a rural environment near the mega-city Guangzhou, China: implications for regional air pollution, radiative forcing and remote sensing, Atmos. Chem. Phys., 8, 5161–5186, 2008.

Gunthe, S. S., King, S. M., **Rose, D.**, Chen, Q., Roldin, P., Farmer, D. K., Jimenez, J. L., Artaxo, P., Andreae, M. O., Martin, S. T., and Pöschl: Cloud condensation nuclei in pristine tropical rainforest air of Amazonia: size-resolved measurements and modeling of atmospheric aerosol composition and CCN activity, Atmos. Chem. Phys., 9, 7551–7575, 2009.

Henning, S., Wex, H., Hennig, T., Kiselev, A., Snider, J., **Rose, D.**, Dusek, U., Frank, G. P., Pöschl, U., Kristensson, A., Bilde, M., Tillmann, R., Kiendler-Scharr, A., Mentel, T. F., Walter, S., Schneider, J., Wennrich, C., and Stratmann, F.: Soluble mass, hygroscopic growth and droplet activation during LExNo, J. Geophys. Res., 115, D11206, doi:10.1029/2009JD012626, 2010.

Pöschl, U., **Rose, D.**, and Andreae, M. O.: Climatologies of cloud-related aerosols - Part 2: Particle hygroscopicity and cloud condensation nucleus activity, in Clouds in the Perturbed Climate System: Their Relationship to Energy Balance, Atmospheric Dynamics, and Precipitation, Strüngmann Forum Report, vol. 2, edited by: Heintzenberg, J. and Charlson, R. J., MIT Press, Cambridge, MA, pp. 57–72, 2009.

Pöschl, U., Martin, S. T., Sinha, B., Chen, Q., Gunthe, S. S., Huffman, J. A., Borrmann, S., Farmer, D. K., Garland, R. M., Helas, G., Jimenez, J. L., King, S. M., Manzi, A., Mikhailov, E., Pauliquevis, T., Petters, M. D., Prenni, A. J., Roldin, P., **Rose, D.**, Schneider, J., Su, H., Zorn, S. R., Artaxo, P., and Andreae, M. O.: Rainforest aerosols as biogenic nuclei of clouds and precipitation in the Amazon, Science, 329, 1513, doi: 10.1126/science.1191056, 2010.

Reutter, P., Su, H., Trentmann, J., Simmel, M., **Rose, D.**, Gunthe, S. S., Wernli, H., Andreae, M. O., and Pöschl, U.: Aerosol- and updraft-limited regimes of cloud droplet formation: influence of particle number, size and hygroscopicity on the activation of cloud condensation nuclei (CCN), Atmos. Chem. Phys., 9, 7067–7080, 2009.

Snider, J. R., Wex, H., **Rose, D.**, Kristensson, A., Stratmann, F., Hennig, T., Henning, S., Kiselev, A., Bilde, M., Burkhart, M., Dusek, U., Frank, G. P., Kiendler-Scharr, A., Mentel, T. F., Petters, M. D., and Pöschl, U.: Intercomparison of CCN and Hygroscopic Fraction Measurements from LExNo, J. Geophys. Res., 115, D11205, doi:10.1029/2009JD012618, 2010.

Stratmann, F., Bilde, M., Dusek, U., Frank, G. P., Hennig, T., Henning, S., Kiendler-Scharr, A., Kiselev, A., Kristensson, A., Lieberwirt, I., Mentel, T. F., Pöschl, U., **Rose, D.**, Schneider, J., Snider, J., Tillmann, R., Walter, S., and Wex, H.: Examination of Laboratory-Generated Coated Soot Particles: An Overview over the LExNo Campaign, J. Geophys. Res., 115, D11203, doi: 10.1029/2009JD012628, 2010.

Su, H., **Rose, D.**, Cheng, Y. F., Gunthe, S. S., Massling, A., Stock, M., Wiedensohler, A., Andreae, M. O., and Pöschl, U.: Technical Note: Hygroscopicity distribution concept for measurement data analysis and modeling of aerosol particle hygroscopicity and CCN activity, Atmos. Chem. Phys., 10, 7489-7503, 2010.

Wex, H., Stratmann, F., Hennig, T., Hartmann, S., Niedermeier, D., Nilsson, E., Ocskay, R., **Rose, D.**, Salma, I., Ziese, M.: Connecting hygroscopic growth at high humidities to cloud activation for different particle types, Environ. Res. Lett., 3, 035004, doi:10.1088/1748-9326/3/3/035004, 2008.

Wiedensohler, A., Cheng, Y. F., Nowak, A., Wehner, B., Achtert, P., Berghof, M., Birmili, W., Wu, Z. J., Hu, M., Zhu, T., Takegawa, N., Kita, K., Kondo, Y., Lou, S. R., Hofzumahaus, A., Holland, F., Wahner, A., Gunthe, S. S., **Rose, D.**, Su, H., and Pöschl, U.: Rapid aerosol particle growth and increase of cloud condensation nucleus activity by secondary aerosol formation and condensation: A case study for regional air pollution in northeastern China, J. Geophys. Res., 114, doi:10.1029/2008JD010884, 2009.

B Köhler theory and models[3]

In this appendix, consistent and precise specifications and distinctions of different types of Köhler models frequently used to calculate critical supersaturations for the CCN activation of ammonium sulfate and sodium chloride aerosol particles will be presented. Model results and differences are compared and discussed in Sect. 2.3.7 and 2.3.8.

B.1 Basic equations and parameters

According to Köhler theory (Köhler, 1936; Pruppacher and Klett, 1997; Seinfeld and Pandis, 2006), the condition necessary for an aqueous solution droplet to be in equilibrium with water vapor in the surrounding gas phase can be expressed by the following basic equation (Kreidenweis et al., 2005; Koehler et al., 2006):

$$s = a_{\mathrm{w}} \cdot Ke \tag{B.1}$$

The water vapor saturation ratio, s, is defined as the ratio of the actual partial pressure of water to the equilibrium vapor pressure over a flat surface of pure water at the same temperature. Expressed in percent, s is identical to the relative humidity (RH), which is typically used to describe the abundance of water vapor under sub-saturated conditions. Under supersaturated conditions ($s>1$, $\mathrm{RH}>100\,\%$), it is customary to describe the abundance of water vapor by the so-called supersaturation S, which is expressed in percent and defined by:

$$S = (s-1) \cdot 100\,\% \tag{B.2}$$

a_{w} is the activity of water in the aqueous solution, and Ke is the so-called Kelvin term, which describes the enhancement of the equilibrium water vapor pressure due to surface curvature.

Under the common assumption that the partial molar volume of water can be approximated by the molar volume of pure water (Kreidenweis et al., 2005), the Kelvin term for a spherical aqueous solution droplet with the diameter D_{wet} is given by:

$$Ke = \exp\left(\frac{4\,\sigma_{\mathrm{sol}}\,M_{\mathrm{w}}}{R\,T\,\rho_{\mathrm{w}}\,D_{\mathrm{wet}}}\right) \tag{B.3}$$

M_{w} and ρ_{w} are the molar mass and density of water (see Tab. B.1), and σ_{sol} is the surface tension of the solution droplet. R and T are the universal gas constant and absolute temperature, respectively. Deviations from this approximation are generally negligible for the dilute aqueous solution droplets formed by hygroscopic salts like ammonium sulfate and sodium chloride at $s{\approx}1$ (Brechtel and Kreidenweis, 2000; Kreidenweis et al., 2005). To describe a_{w} and σ_{sol} as a function of droplet composition, various types of equations, parameterizations, and approximations have been proposed and can be used as detailed below.

For a given type and mass of solute (dissolved substance), a plot of s vs. D_{wet} generally exhibits a maximum in the region where $s>1$ and $S>0$. The saturation ratio and supersaturation at this

---

[3] This section is based on the manuscript "Calibration and measurement of a continuous-flow cloud condensation nuclei counter (DMT-CCNC): CCN activation of ammonium sulfate and sodium chloride aerosol particles in theory and experiment" by D. Rose, S. S. Gunthe, E. Mikhailov, G. P. Frank, U. Dusek, M. O. Andreae, and U. Pöschl, published in Atmos. Chem. Phys. (Rose et al., 2008).

Table B.1: Density and molar mass at 298.15 K for the investigated compounds.

	H_2O	NaCl	$(NH_4)_2SO_4$
ρ [kg m^{-3}]	997.1	2165	1770
M [kg mol^{-1}]	0.0180153	0.0584428	0.1321395

maximum are the so-called critical saturation s_c and critical supersaturation S_c, respectively, which are associated with the so-called critical droplet diameter, $D_\mathrm{wet,c}$. Droplets reaching or exceeding this diameter can freely grow by condensation of water vapor from the supersaturated gas phase and form cloud droplets (Pruppacher and Klett, 1997; Seinfeld and Pandis, 2006).

Aerosol particles consisting of soluble and hygroscopic substances, such as ammonium sulfate and sodium chloride, generally take up water vapor and already form aqueous solution droplets at $s<1$ (hygroscopic growth). The ratio of the droplet diameter, D_wet, to the diameter of a compact spherical particle consisting of the dry solute, D_s (mass equivalent diameter of the dry solute particle), is defined as the (mass equivalent) growth factor of the dry solute particle, g_s:

$$g_\mathrm{s} = \frac{D_\mathrm{wet}}{D_\mathrm{s}} = \left(\frac{\rho_\mathrm{s}}{x_\mathrm{s}\rho_\mathrm{sol}}\right)^{\frac{1}{3}} \tag{B.4}$$

x_s is the mass fraction of the solute in the droplet, and ρ_s is the density of the dry solute (cf. Tab. B.1). Equations (B.1), (B.3), and (B.4) can be used to describe the hygroscopic growth and CCN activation of aerosol particles (D_wet as a function of s – or vice versa – for any given value of D_s), if a_w, ρ_sol, and σ_sol are known as a function of droplet composition, which is usually described by the solute mass fraction x_s, molality μ_s, or molarity c_s.

The molality is defined as the amount of substance (number of moles) of solute, $n_\mathrm{s}=m_\mathrm{s}\,M_\mathrm{s}^{-1}$, divided by the mass of solvent, i.e., by the mass of water in an aqueous solution, $m_\mathrm{w}=n_\mathrm{w}\,M_\mathrm{w}$. M_s is the molar mass of the solute (cf. Tab. B.1), m_s is the mass of the solute, and n_w is the amount of substance (number of moles) of water in the solution.

The molarity is defined as the amount of substance divided by the volume of the solution in units of mol L^{-1}. Mass fraction, molality, and molarity of the solute are related by:

$$\mu_\mathrm{s} = \frac{x_\mathrm{s}}{M_\mathrm{s}\,(1-x_\mathrm{s})} = \frac{m_\mathrm{s}}{M_\mathrm{s}\,m_\mathrm{w}} = \frac{n_\mathrm{s}}{M_\mathrm{w}\,n_\mathrm{w}} = \frac{\pi\,\rho_\mathrm{s}\,D_\mathrm{s}^3}{6\,M_\mathrm{s}\,n_\mathrm{w}\,M_\mathrm{w}} \tag{B.5}$$

$$c_\mathrm{s} = \frac{x_\mathrm{s}\,\rho_\mathrm{sol}}{M_\mathrm{s}} \cdot 10^{-3}\,\mathrm{m}^3\,\mathrm{L}^{-1} \tag{B.6}$$

The scaling factor $10^{-3}\,\mathrm{m}^3\,\mathrm{L}^{-1}$ is required to relate the molarity in mol L^{-1} to the other quantities, which are generally given in SI units.

Depending on the types of parameterizations used to describe a_w, ρ_sol, and σ_sol, different models can be used to calculate the critical supersaturation S_c for any given value of D_s. The different options considered and compared in this study are outlined below and discussed in Sect. 2.3.7.

In the Köhler model calculations used for CCNC calibration, the experimentally determined critical dry particle diameter D_c (i.e., the fit parameter D_a or D_t, or a shape corrected value as detailed

Table B.2: Polynomial coefficients used to calculate the water activity with Eq. (B.7) or (B.8). The coefficients a_1, a_2, a_3, and a_4 for $(NH_4)_2SO_4$ and NaCl at 298 K are given in Tang and Munkelwitz (1994) and in Tang (1996), respectively. The coefficients k_1, k_2, and k_3 are the Kelvin corrected values for $(NH_4)_2SO_4$ and the Kelvin and shape corrected values for NaCl, taken from Kreidenweis et al. (2005).

water activity parameters	$(NH_4)_2SO_4$	NaCl
a_1	-2.715×10^{-3}	-6.366×10^{-3}
a_2	3.113×10^{-5}	8.624×10^{-5}
a_3	-2.336×10^{-6}	-1.158×10^{-5}
a_4	1.412×10^{-8}	1.518×10^{-7}
k_1	2.42848	5.78874
k_2	–3.85261	–8.38172
k_3	1.88159	3.9265

in Sect. 2.2.3.4) was taken as the dry solute mass equivalent diameter D_s, corresponding to a solute mass of $m_\mathrm{s}=\pi/6\,\rho_\mathrm{s}\,D_\mathrm{s}^3$. The CCNC column top temperature (T_1) was taken as the model temperature T.

B.2 Activity parameterization (AP) models

For the activity of water in aqueous solution droplets of $(NH_4)_2SO_4$, NaCl, and other salts, Tang and Munkelwitz (1994) and Tang (1996) have presented parameterizations derived from electrodynamic balance (EDB) single particle experiments as polynomial fit functions of solute mass percentage ($100\,x_\mathrm{s}$):

$$a_\mathrm{w} = 1 + \sum_q a_q\ (100\,x_\mathrm{s})^q \tag{B.7}$$

The polynomial coefficients a_q for $(NH_4)_2SO_4$ and NaCl at 298 K are listed in Table B.2.

An alternative parameterization of a_w has been proposed by Kreidenweis et al. (2005), who derived the following relation between a_w and the growth factor of dry solute particles (g_s) determined in measurements with a hygroscopicity tandem differential mobility analyzer (HTDMA):

$$g_\mathrm{s} = \frac{D_\mathrm{wet}}{D_\mathrm{s}} = \left(1 + \left(k_1 + k_2\,a_\mathrm{w} + k_3\,a_\mathrm{w}^2\right)\frac{a_\mathrm{w}}{1-a_\mathrm{w}}\right)^{\frac{1}{3}} \tag{B.8}$$

The coefficients k_1, k_2, and k_3 for $(NH_4)_2SO_4$ and NaCl are listed in Table B.2.

The water activity a_w can be also calculated with the Aerosol Inorganics Model (AIM, Pitzer-Simonson-Clegg mole fraction based model; http://www.aim.env.uea.ac.uk/aim/aim.html; Clegg et al., 1998a,b). For a variety of inorganic substances, the solute molality can be calculated online for prescribed a_w values and the results can be downloaded in form of a table. The model was run for $(NH_4)_2SO_4$ and NaCl at 298.15 K and for each salt a table of a_w vs. μ_s in the activity range of

Table B.3: Polynomial coefficients used to calculate the density of a solution droplet using Eq. (B.9). The coefficients d_1, d_2, d_3, and d_4 for $(NH_4)_2SO_4$ and NaCl at 298 K are given in Tang and Munkelwitz (1994) and in Tang (1996), respectively.

density parameters	$(NH_4)_2SO_4$	NaCl
d_1	5.92×10^{-3}	7.41×10^{-3}
d_2	-5.036×10^{-6}	-3.741×10^{-5}
d_3	1.024×10^{-8}	2.252×10^{-6}
d_4	–	-2.06×10^{-8}

0.9 to 0.9999 (100 equidistant steps from 0.9 to 0.97, 300 steps of 0.0001 from 0.97 to 0.9999) was obtained, covering a molality range of $\sim$3 to $\sim 0.002\,\mathrm{mol\,kg^{-1}}$.

Low (1969) provided a table of a_w for ammonium sulfate and sodium chloride for molality values of 0.1 to 6 $\mathrm{mol\,kg^{-1}}$. For the calculation of S_c, however, this range of molalities is insufficient and has to be extrapolated below 0.1 $\mathrm{mol\,kg^{-1}}$. This approach has been tested with a third order polynomial fit, but the results were very different from the parameterizations given above (deviations up to a factor of 2 in S_c) and are not discussed any further.

For the density of aqueous solution droplets of $(NH_4)_2SO_4$ and NaCl, and other salts, Tang and Munkelwitz (1994) and Tang (1996) have also presented parameterizations of experimentally determined values as polynomial fit functions of solute mass percentage ($100\,x_\mathrm{s}$):

$$\rho_\mathrm{sol} = \rho_\mathrm{w} + \left[\sum_q d_q\,(100\,x_\mathrm{s})^q\right] \cdot 10^3\,\mathrm{kg\,m^{-3}} \tag{B.9}$$

ρ_w is the density of pure water in $\mathrm{kg\,m^{-3}}$ (e.g., 997.1 $\mathrm{kg\,m^{-3}}$ at 298 K) and the coefficients for $(NH_4)_2SO_4$ and NaCl at 298 K are listed in Table B.3.

Under the assumption of volume additivity (partial molar volumes of solute and solvent in solution are equal to molar volumes of pure substances; Mikhailov et al., 2004), ρ_sol can also be calculated by

$$\rho_\mathrm{sol} = \left(\frac{1-x_\mathrm{s}}{\rho_\mathrm{w}} + \frac{x_\mathrm{s}}{\rho_\mathrm{s}}\right)^{-1} \tag{B.10}$$

The simplest parameterization of ρ_sol used in this study was approximating it by the density of pure water, either with a constant value of 997.1 $\mathrm{kg\,m^{-3}}$ or a temperature dependent one. The temperature dependence of the density of pure water can be described according to Pruppacher and Klett (1997):

$$\rho_\mathrm{w} = \left[\frac{A_0 + A_1\,t + A_2\,t^2 + A_3\,t^3 + A_4\,t^4 + A_5\,t^5}{1 + B\,t}\right] \cdot 1\,\mathrm{kg\,m^{-3}} \tag{B.11}$$

Here t is the temperature in °C (t=$T-273.15$ K) and the coefficients A_0 to A_5, and B are given in Tab. B.4.

The deviations caused by using different parameterizations and approximations of ρ_sol turned out to be small, as detailed in Sect. 2.3.7.

Table B.4: Coefficients used to calculate the density of water as a function of temperature according to Eq. (B.11) taken from Pruppacher and Klett (1997).

density parameters	value
A_0	999.8396
A_1 [°C^{-1}]	18.224944
A_2 [°C^{-2}]	–7.92221×10^{-3}
A_3 [°C^{-3}]	–55.44846×10^{-6}
A_4 [°C^{-4}]	149.7562×10^{-9}
A_5 [°C^{-5}]	–393.2952×10^{-12}
B [°C^{-1}]	18.159725×10^{-3}

For the surface tension of aqueous salt solution droplets, Seinfeld and Pandis (2006) proposed the following parameterization:

$$\sigma_{\mathrm{sol}} = \sigma_{\mathrm{w}} + \gamma_{\mathrm{s}} \cdot c_{\mathrm{s}} \tag{B.12}$$

in which γ_{s}=$2.17 \cdot 10^{-3}\mathrm{N\,m^{-1}\,L\,mol^{-1}}$ for $(\mathrm{NH_4})_2\mathrm{SO_4}$ and γ_{s}=$1.62 \cdot 10^{-3}\mathrm{N\,m^{-1}\,L\,mol^{-1}}$ for NaCl. σ_{w} is the surface tension of pure water as detailed below, and c_{s} is the molarity of the solute. Alternative concentration-dependent parameterizations (Hänel, 1976; Weast and Astle, 1982; Chen, 1994; Gysel et al., 2002) exhibited only small deviations in σ_{sol} in the concentration range of interest (<1 % for μ_{s}<$1\mathrm{mol\,kg^{-1}}$).

The simplest parameterization of σ_{sol} used in this study was approximating it by the surface tension of pure water, either with a constant value of 0.072 N m^{-1} or a temperature dependent one. According to Seinfeld and Pandis (2006), the temperature dependence of the surface tension of pure water can be described by:

$$\sigma_{\mathrm{w}} = 0.0761\,\mathrm{N\,m^{-1}} - \gamma_{\mathrm{t}}\ (\mathrm{T} - 273\,\mathrm{K}) \tag{B.13}$$

in which γ_t=$1.55 \times 10^{-4}\,\mathrm{N\,m^{-1}\,K^{-1}}$.

Combination of Eqs. (B.1), (B.3), and (B.4) leads to the following version of the Köhler equation, which was taken as the basis for all activity parameterization (AP) model calculations:

$$s = a_{\mathrm{w}} \exp\left(\frac{4\,\sigma_{\mathrm{sol}}\,M_{\mathrm{w}}}{\rho_{\mathrm{w}}\,R\,T\,g_{\mathrm{s}}\,D_{\mathrm{s}}}\right) \tag{B.14}$$

Depending on the applied type of water activity parameterization, three types of AP models are distinguished: AP1 using the mass percentage-based parameterizations of Tang and Munkelwitz (1994) and Tang (1996), AP2 using the growth factor-based parameterizations of Kreidenweis et al. (2005), and AP3 using the Pitzer-Simonson-Clegg mole fraction based model AIM.

In AP1 model calculations, x_{s} was taken as the primary variable to calculate a_{w} from Eq. (B.7); ρ_{sol} from Eq. (B.9) with ρ_{w} from Eq. (B.11); g_{s} from Eq. (B.4); σ_{sol} from Eq. (B.12) with σ_{w} from

Eq. (B.13) and c_s from Eq. (B.6); and s from Eq. (B.14) (base case AP1, Table 2.3). The maximum value of s (critical saturation ratio, s_c) was determined by the variation of x_s (numerical minimum search for $-s$ with the 'fminsearch' function, Matlab software), and via Eq. (B.2) it was converted into the corresponding critical supersaturation S_c.

In AP2 model calculations, a_w was taken as the primary variable to calculate g_s from Eq. (B.8); ρ_sol from Eq. (B.10) with ρ_w from Eq. (B.11); $x_\mathrm{s}{=}m_\mathrm{s}/\left(m_\mathrm{s}{+}m_\mathrm{w}\right)$, and $m_\mathrm{w}{=}\pi/6\,\rho_\mathrm{w}\,D_\mathrm{s}^3\left(g_\mathrm{s}^3{-}1\right)$ (volume additivity assumption); σ_sol from Eq. (B.12) with σ_w from Eq. (B.13) and c_s from Eq. (B.6); and s from Eq. (B.14) (base case AP2, Table 2.3). The maximum value of s (critical saturation ratio) was determined by variation of a_w (numerical minimum search for $-s$ with the 'fminsearch' function, Matlab software), and via Eq. (B.2) it was converted into the corresponding S_c.

In AP3 model calculations, x_s was taken as the primary variable to calculate μ_s from Eq. (B.5) and a_w by linear interpolation of the tabulated data of a_w vs. μ_s obtained from the online AIM (see above); ρ_sol from Eq. (B.9) with ρ_w from Eq. (B.11); g_s from Eq. (B.4); σ_sol from Eq. (B.12) with σ_w from Eq. (B.13) and c_s from Eq. (B.6); and s from Eq. (B.14) (base case AP3, Table 2.3). The maximum value of s (critical saturation ratio, s_c) was determined by the variation of x_s (numerical minimum search for $-s$ with the 'fminsearch' function, Matlab software), and via Eq. (B.2) it was converted into the corresponding critical supersaturation S_c. In sensitivity studies investigating the influence of various simplifications and approximations of the droplet density and surface tension, individual parameterizations were exchanged as detailed in Table 2.3, but the basic calculation procedure remained unchanged (test cases AP3.a to AP3.d).

B.3 Osmotic coefficient (OS) models

According to Robinson and Stokes (1959), the activity of water in aqueous solutions of ionic compounds can be described by:

$$a_\mathrm{w} = \exp\left(-\nu_\mathrm{s}\,\Phi_\mathrm{s}\,\mu_\mathrm{s}\,M_\mathrm{w}\right) \tag{B.15}$$

ν_s is the stoichiometric dissociation number of the solute, i.e., the number of ions per molecule or formula unit ($\nu_\mathrm{NaCl}{=}2$, $\nu_{(\mathrm{NH_4})_2\mathrm{SO_4}}{=}3$). Φ_s is the molal or practical osmotic coefficient of the solute in aqueous solution, which deviates from unity if the solution is not ideal (incomplete dissociation, ion-ion and ion-solvent interactions).

Based on an ion-interaction approach, Pitzer and Mayorga (1973) derived semiempirical parameterizations, which describe Φ_s as a function of solute molality μ_s. The general form for electrolytes dissociating into two types of ions is:

$$\Phi_\mathrm{s} = 1 - |z_1\,z_2|\left(A_\Phi\frac{\sqrt{I}}{1+b\sqrt{I}}\right) + \mu_\mathrm{s}\frac{2\,\nu_1\,\nu_2}{\nu_\mathrm{s}}\left(\beta_0 + \beta_1\,e^{-\alpha\sqrt{I}}\right) + \mu_\mathrm{s}^2\frac{2\,(\nu_1\,\nu_2)^{\frac{3}{2}}}{\nu_\mathrm{s}}C_\Phi \tag{B.16}$$

ν_1 and ν_2 are the numbers of positive and negative ions produced upon dissociation per formula unit of the solute ($\nu_\mathrm{s}{=}\nu_1{+}\nu_2$); $|z_1|$ and $|z_2|$ are the numbers of elementary charges carried by the ions: $\nu_1{=}|z_2|{=}2$ and $\nu_2{=}|z_1|{=}1$ for $(\mathrm{NH_4})_2\mathrm{SO_4}$; $\nu_1{=}\nu_2{=}|z_1|{=}|z_2|{=}1$ for NaCl. The ionic strength is given by $I{=}0.5\,\mu_\mathrm{s}\left(\nu_1\,z_1^2{+}\nu_2\,z_2^2\right)$. A_Φ is the Debye-Hückel coefficient, which has the value $0.3915\,(\mathrm{kg\,mol^{-1}})^{1/2}$ for water at 298.15 K. The parameters α and b are $2\,(\mathrm{kg\,mol^{-1}})^{1/2}$ and $1.2\,(\mathrm{kg\,mol^{-1}})^{1/2}$, respectively. The coefficients β_0, β_1 and C_Φ depend on the chemical composition

Table B.5: Ion-interaction coefficients at 298.15 K used to calculate the practical osmotic coefficients of ammonium sulfate and sodium chloride in aqueous solution using Eq. (B.16).

parameter	$(NH_4)_2SO_4$[a]	NaCl[a]	NaCl[b]
β_0 [$\mathrm{kg\,mol^{-1}}$]	0.0409	0.0765	0.1018
β_1 [$\mathrm{kg\,mol^{-1}}$]	0.6585	0.2664	0.2770
C_Φ [$\mathrm{kg^2\,mol^{-2}}$]	–0.0012	0.00127	0.00119

[a] Pitzer and Mayorga (1973); [b] Mokbel et al. (1997)

Table B.6: Parameters of Y_a, Y_b, and Y_c for ammonium sulfate and sodium chloride taken from Brechtel and Kreidenweis (2000) used in Eq. (B.17).

Salt	Y_a [$\mathrm{mol\,m^{-3}}$]	Y_b [$\mathrm{mol\,m^{-3}}$]	Y_c [$\mathrm{mol\,m^{-3}}$]
$(NH_4)_2SO_4$	321.3×10^{-3}	80.3×10^{-3}	8.93×10^{-3}
NaCl	74.1×10^{-3}	74.1×10^{-3}	18.52×10^{-3}

of the solute and have been tabulated by Pitzer and Mayorga (1973) for over 200 compounds (1:1, 1:2, and 2:1 electrolytes). For ammonium sulfate and sodium chloride, at 298.15 K, the respective values and more recent updates from Mokbel et al. (1997) are listed in Table B.5. In the here performed model calculations the parameters of Pitzer and Mayorga (1973) were used. For the relevant conditions of CCN activation, the parameters of Mokbel et al. (1997) lead essentially to the same S_c values (relative deviations <0.4 %).

A more simplified form of Eq. (B.16) was introduced by Brechtel and Kreidenweis (2000):

$$\Phi_\mathrm{s} = 1 - \frac{A_\Phi \sqrt{Y_a\, c}}{\sqrt{2} + b\sqrt{Y_b\, c}} + 2Y_c\, c\, \beta_0 \qquad \text{(B.17)}$$

with the coefficient $c = D_\mathrm{s}^3 / \left(\rho_\mathrm{w}\,\left(D_\mathrm{wet}^3 - D_\mathrm{s}^3\right)\right)$. The parameters A_Φ, b, and β_0 are the same variables used in Eq. (B.16) and are given above. The coefficients Y_a, Y_b, and Y_c for ammonium sulfate and sodium chloride are taken from Brechtel and Kreidenweis (2000) and listed in Table B.6.

Depending on the applied type of osmotic coefficient parameterization, two types of OS models are distinguished: OS1 using the parameterization of Pitzer and Mayorga (1973) (Eq. B.16), and OS2 using the parameterization of Brechtel and Kreidenweis (2000) (Eq. B.17).

The OS1 model calculations were performed in analogy to the AP1 model calculations as detailed above (with x_s as the primary variable for the calculation of other parameters), except that a_w was calculated from Eq. (B.15) with Φ_s from Eq. (B.16) and μ_s from Eq. (B.5). The OS2 model calculations were done in the same way as OS1 unless using Eq. (B.17) for parameterizing Φ_s.

B.4 Van't Hoff factor (VH) models

According to McDonald (1953) and the early cloud physics literature, the activity of water in aqueous solutions of ionic compounds can be described by the following form of Raoult's law, where the effects of ion dissociation and interactions are represented by the so-called van't Hoff factor, i_s:

$$a_\mathrm{w} = \frac{n_\mathrm{w}}{n_\mathrm{w} + i_\mathrm{s}\, n_\mathrm{s}} = \left(1 + i_\mathrm{s} \frac{n_\mathrm{s}}{n_\mathrm{w}}\right)^{-1} = (1 + i_\mathrm{s}\, \mu_\mathrm{s}\, M_\mathrm{w})^{-1} \tag{B.18}$$

For strong electrolytes such as ammonium sulfate and sodium chloride, the van't Hoff factor is similar to the stoichiometric dissociation number, and deviations of i_s from ν_s can be attributed to solution non-idealities (incomplete dissociation, ion-ion and ion-solvent interactions). The exact relation between i_s and ν_s or Φ_s is given by equating Eqs. (B.15) and (B.18). As detailed by Kreidenweis et al. (2005), the resulting equation can be approximated by a series expansion of the exponential term in Eq. (B.15), inserting $n_\mathrm{s}/n_\mathrm{w}{=}\mu_\mathrm{s}\, M_\mathrm{w}$ (cf. Eq. (B.5)) and truncation of the series. It follows then that:

$$i_\mathrm{s} \approx \nu_\mathrm{s}\, \Phi_\mathrm{s} \tag{B.19}$$

Deviations from this approximation are negligible for the dilute aqueous solution droplets formed by hygroscopic salts such as ammonium sulfate and sodium chloride at $s{\approx}1$ (molality <0.01 mol kg^{-1}; relative magnitude of quadratic and higher terms of series expansion <1 %).

Combination of Eqs. (B.14) and (B.15) with $\mu_\mathrm{s}{=}m_\mathrm{s}/\,(M_\mathrm{s}\, m_\mathrm{w})$, $m_\mathrm{w}{=}\pi/6\, D_\mathrm{wet}^3\, \rho_\mathrm{sol}{-}m_\mathrm{s}$, $g_\mathrm{s}\, D_\mathrm{s}{=}$ D_wet, and Eq. (B.19) leads to:

$$s = \exp\left(\frac{4\,\sigma_\mathrm{sol}\, M_\mathrm{w}}{\rho_\mathrm{w}\, R\, T\, D_\mathrm{wet}} - \frac{i_\mathrm{s}\, m_\mathrm{s}\, M_\mathrm{w}}{M_\mathrm{s}\left(\frac{\pi}{6} D_\mathrm{wet}^3\, \rho_\mathrm{sol} - m_\mathrm{s}\right)}\right) \tag{B.20}$$

For the dilute aqueous solution droplets formed by hygroscopic salts like ammonium sulfate and sodium chloride at $s{\approx}1$, the contribution of the solute to the total mass of the droplet is low ($m_\mathrm{s}/(\pi/6\, D_\mathrm{wet}^3\, \rho_\mathrm{sol}){<}4\,\%$ at D_s=20 nm and <0.1 % at 200 nm). If m_s is neglected, Eq. (B.20) reduces to:

$$s = \exp\left(\frac{4\,\sigma_\mathrm{sol}\, M_\mathrm{w}}{\rho_\mathrm{w}\, R\, T\, D_\mathrm{wet}} - \frac{6\, i_\mathrm{s}\, m_\mathrm{s}\, M_\mathrm{w}}{\pi\, M_\mathrm{s}\, D_\mathrm{wet}^3\, \rho_\mathrm{sol}}\right) \tag{B.21}$$

For the dilute salt solution droplets, differences between ρ_w and ρ_sol (<3 % at D_s=20 nm, <0.1 % at 200 nm) and between σ_w and σ_sol (<1 % at D_s=20 nm, ∼ 0 % at 200 nm) are also relatively small. With the approximations of $\rho_\mathrm{sol}{\approx}\rho_\mathrm{w}$ and $\sigma_\mathrm{sol}{\approx}\sigma_\mathrm{w}$, Eq. (B.21) can be transformed into the following simplified and widely used form of the Köhler equation (e.g. Pruppacher and Klett, 1997; Seinfeld and Pandis, 2006):

$$s = \exp\left(\frac{A}{D_\mathrm{wet}} - \frac{B}{D_\mathrm{wet}^3}\right) \tag{B.22}$$

where

$$A = \frac{4\,\sigma_\mathrm{w}\, M_\mathrm{w}}{\rho_\mathrm{w}\, R\, T} \tag{B.23}$$

and

$$B = \frac{6\, i_\mathrm{s}\, m_\mathrm{s}\, M_\mathrm{w}}{\pi\, M_\mathrm{s}\, \rho_\mathrm{w}} = \frac{i_\mathrm{s}\, M_\mathrm{w}\, \rho_\mathrm{s}\, D_\mathrm{s}^3}{M_\mathrm{s}\, \rho_\mathrm{w}} = \frac{6\, i_\mathrm{s}\, n_\mathrm{s}\, M_\mathrm{w}}{\pi\, \rho_\mathrm{w}} \tag{B.24}$$

Under the assumption of complete dissociation and ideal solution behavior (Φ_s=1), the van't Hoff factor is i_s=2 for NaCl and i_s=3 for $\mathrm{(NH_4)_2SO_4}$ solutions. For NaCl this approximation is quite common and the deviations from experimental results are small (Gerber et al., 1977), but for $\mathrm{(NH_4)_2SO_4}$ it has been shown that i_s has to be between 2 and 2.5 to achieve agreement between measured and calculated droplet diameters (Gerber et al., 1977; Pradeep Kumar et al., 2003).

McDonald (1953) already remarked that the van't Hoff factor is not a constant value, but varies with the solute molality. Low (1969) presented a table of van't Hoff factors for a number of electrolytes at molalities of 0.1–6 mol kg^{-1} and 298.15 K. For ammonium sulfate, i_s can be parameterized as a function of μ_s with the following cubic polynomial fit of the tabulated values (Frank et al., 2007):

$$i_\mathrm{s} = 0.021\,\mathrm{kg^2\,mol^{-2}} \cdot \mu_\mathrm{s}^2 - 0.0428\,\mathrm{kg\,mol^{-1}} \cdot \mu_\mathrm{s} + 1.9478 \tag{B.25}$$

An alternative parameterization given by Young and Warren (1992) is valid for smaller molalities:

$$i_\mathrm{s} = -0.007931 \cdot \log^2\left(\mu_\mathrm{s} \cdot \mathrm{kg\,mol^{-1}}\right) - 0.1844 \cdot \log\left(\mu_\mathrm{s} \cdot \mathrm{kg\,mol^{-1}}\right) + 1.9242 \tag{B.26}$$

From the different Köhler equations listed above, four different VH models (VH1–VH4) were derived and tested.

The non-simplified VH model calculations (VH1) for ammonium sulfate solution droplets were made taking μ_s as the primary variable to calculate a_w from Eq. (B.18) and to calculate i_s. The value of i_s was calculated from Eq. (B.25) for $\mu_\mathrm{s}>1$, and from Eq. (B.26) for $\mu_\mathrm{s}\leq 1$ as suggested by Frank et al. (2007). $x_\mathrm{s}=m_\mathrm{s}/\left(m_\mathrm{s}+m_\mathrm{w}\right)$; m_w was calculated from Eq. (B.5); ρ_sol from Eq. (B.9) with ρ_w from Eq. (B.11); g_s from Eq. (B.4); σ_sol from Eq. (B.12) with σ_w from Eq. (B.13) and c_s from Eq. (B.6); and s from Eq. (B.14).

VH2 model calculations were made using a simplified Köhler equation (Eq. B.20; assuming $i_\mathrm{s}\approx\nu_\mathrm{s}\,\Phi_\mathrm{s}$). In this equation, i_s was calculated as in VH1 using μ_s as a primary variable. x_s, ρ_w, ρ_sol, and σ_sol were calculated as in VH1. D_wet was calculated from Eq. (B.4).

A further simplified Köhler equation (Eq. B.21) was used to make VH3 model calculations. μ_s was taken as a primary variable to calculate i_s. i_s, x_s, ρ_w, ρ_sol, and σ_sol were calculated as in VH1; D_wet as in VH2; all parameters were inserted into Eq. (B.21) to calculate s.

The VH4 model used Eq. (B.22) to calculate s. μ_s was taken as a primary variable to calculate i_s. i_s, x_s, ρ_w, σ_w were calculated as in VH1. D_wet was calculated from Eq. (B.4) which required the parameterization of ρ_sol. Because the Köhler equation used for VH4 was derived assuming ρ_sol as ρ_w, the same approximation was also used to calculate D_wet.

For all VH model calculations, the maximum value of s was determined by variation of μ_s (numerical minimum search for –s with the 'fminsearch' function, Matlab software). The critical supersaturation S_c was calculated from the maximum of s using Eq. (B.2).

In sensitivity studies investigating the influence of simplifications and approximations, individual parameterizations were exchanged as detailed in Table 2.3, but the basic calculation procedure (VH1, VH2, VH3, VH4) remained unchanged.

B.5 Effective hygroscopicity parameter (EH) models

Petters and Kreidenweis (2007) defined a hygroscopicity parameter κ that can be used to parameterize the composition dependent water activity of a solution droplet:

$$a_\mathrm{w} = \left(1 + \kappa \frac{V_\mathrm{s}}{V_\mathrm{w}}\right)^{-1} \tag{B.27}$$

with $V_\mathrm{s}{=}n_\mathrm{s}\,M_\mathrm{s}/\rho_\mathrm{s}$ and $V_\mathrm{w}{=}n_\mathrm{w}\,M_\mathrm{w}/\rho_\mathrm{w}$ being the volumes of the dry solute and of the water in the droplet, respectively. From comparison with Eq. (B.18) follows:

$$\kappa = i_\mathrm{s} \frac{n_\mathrm{s}\,V_\mathrm{w}}{n_\mathrm{w}\,V_\mathrm{s}} = i_\mathrm{s} \frac{v_\mathrm{w}}{v_\mathrm{s}} = i_\mathrm{s} \frac{\rho_\mathrm{s}\,M_\mathrm{w}}{\rho_\mathrm{w}\,M_\mathrm{s}} \tag{B.28}$$

with v_s and v_w being the molar volumes of the solute and of water, respectively. For the CCN activation of $(NH_4)_2SO_4$ and NaCl, Petters and Kreidenweis (2007) proposed κ values of 0.61 and 1.28 corresponding to i_s=2.52 and i_s=1.91, respectively. These κ values were derived from the Aerosol Inorganics Model (AIM), fullfilling Eq. (B.27) for $(NH_4)_2SO_4$ at S_c=0.27 % (D_s=67 nm) and for NaCl at S_c=0.15 % (D_s=80 nm).

Note that besides κ also other effective hygroscopicity parameters have been proposed and can be used in analogy to describe the influence of soluble particle material on the CCN activation of aerosol particles. For example, Wex et al. (2007) have defined and used an "ion density" parameter $\rho_\mathrm{ion}{=}\Phi_\mathrm{s}\,\nu_\mathrm{s}\,\rho_\mathrm{s}/M_\mathrm{s}{\approx}i_\mathrm{s}\,\rho_\mathrm{s}/M_\mathrm{s}{=}\kappa\,\rho_\mathrm{w}/M_\mathrm{w}$. The above κ values for $(NH_4)_2SO_4$ and NaCl are equivalent to ρ_ion values of 3.38×10^4 mol m^{-3} and 7.08×10^4 mol m^{-3}, respectively.

Assuming volume additivity ($V_\mathrm{w}{=}V_\mathrm{wet}{-}V_\mathrm{s}$, with the total volume of the solution droplet V_wet), and spherical shape of the dry solute particle and solution droplet (i.e., $D_\mathrm{s}^3{=}6\,V_\mathrm{s}/\pi$ and $D_\mathrm{wet}^3{=}6\,V_\mathrm{wet}/\pi$, respectively) Eq. (B.27) can be rewritten as:

$$a_\mathrm{w} = \frac{D_\mathrm{wet}^3 - D_\mathrm{s}^3}{D_\mathrm{wet}^3 - D_\mathrm{s}^3\,(1-\kappa)} \tag{B.29}$$

The full Köhler equation (Eq. B.14) with a_w taken from Eq. (B.29) and g_s from Eq. (B.4) results in the following equation, which was used as the basis for EH1 Köhler model calculations:

$$s = \frac{D_\mathrm{wet}^3 - D_\mathrm{s}^3}{D_\mathrm{wet}^3 - D_\mathrm{s}^3\,(1-\kappa)} \exp\left(\frac{4\,\sigma_\mathrm{sol}\,M_\mathrm{w}}{R\,T\,\rho_\mathrm{w}\,D_\mathrm{wet}}\right) \tag{B.30}$$

In EH1 Köhler model calculations x_s was taken as the primary variable to calculate D_wet from Eq. (B.4) with ρ_sol from Eq. (B.9) and ρ_w from Eq. (B.11); σ_sol was calculated from Eq. (B.12) with σ_w from Eq. (B.13) and c_s from Eq. (B.6); and s from Eq. (B.30). The maximum value of s (critical saturation ratio, s_c) was determined by the variation of x_s (numerical minimum search for $-s$ with the 'fminsearch' function, Matlab software), and via Eq. (B.2) it was converted into the corresponding critical supersaturation S_c.

B.6 Analytical approximation (AA) model

In all Köhler models that have been presented so far, the critical saturation s_c was determined through numerical iteration by varying the primary variable (such as μ_s, x_s, or a_w) for s in the particular proposed equation until it reached a maximum. Assuming a concentration-independent van't Hoff factor or effective hygroscopicity parameter, the iterative numerical solution can be approximated by a simplified analytical equation expressing s_c as a function of dry solute particle mass equivalent diameter, D_s (Petters and Kreidenweis, 2007; Seinfeld and Pandis, 2006):

$$s_\mathrm{c} = \exp\left(\sqrt{\frac{4\,A^3}{27\,B}}\right) = \exp\left(\sqrt{\frac{4\,A^3\,M_\mathrm{s}\,\rho_\mathrm{w}}{27\,i_\mathrm{s}\,M_\mathrm{w}\,\rho_\mathrm{s}\,D_\mathrm{s}^3}}\right) \tag{B.31}$$

$$s_\mathrm{c} = \exp\left(\sqrt{\frac{4\,A^3}{27\,\kappa\,D_\mathrm{s}^3}}\right) \tag{B.32}$$

In the AA model calculations, the widely used approximation $A{\approx}(0.66{\times}10^{-6}\,\mathrm{K\,m})\,/\,T$ was inserted for the Kelvin term parameter A as defined in Eq. (B.23) (Seinfeld and Pandis, 2006) and different values of i_s and κ were tested (i_s=2.2 or 3 and κ=0.61 for ammonium sulfate; i_s=2 and κ=1.28 for sodium chloride).

A comparison and discussion of critical supersaturations calculated with the different AP, OS, VH, EH and AA models specified above is given in Sect. 2.3.7. For CCNC calibration, the VH4 model has been used in this study unless mentioned otherwise.

C Supplementary data

In addition to the PRIDE-PRD2006 field campaign and results presented in Sect. 3, further measurements in polluted air were performed near the city of Beijing, China, in the course of a campaign aimed at the improvement of air quality for the Olympic Summer Games 2008 (CAREBeijing-2006, 11 August to 9 September 2006). CCN measurements at a remote continental location were performed during field campaigns at the Jungfraujoch observatory in the Swiss Alps (CLACE-5 and -6; 22 February to 21 March 2006 and 17 February to 14 March 2007, respectively). Moreover, the research work performed within the PhD studies underlying this thesis contributed to the investigation of CCN in pristine Amazonian rainforest air (AMAZE-08, 7 February to 14 March). An overview of measurement data acquired at these locations is given in the following figures.

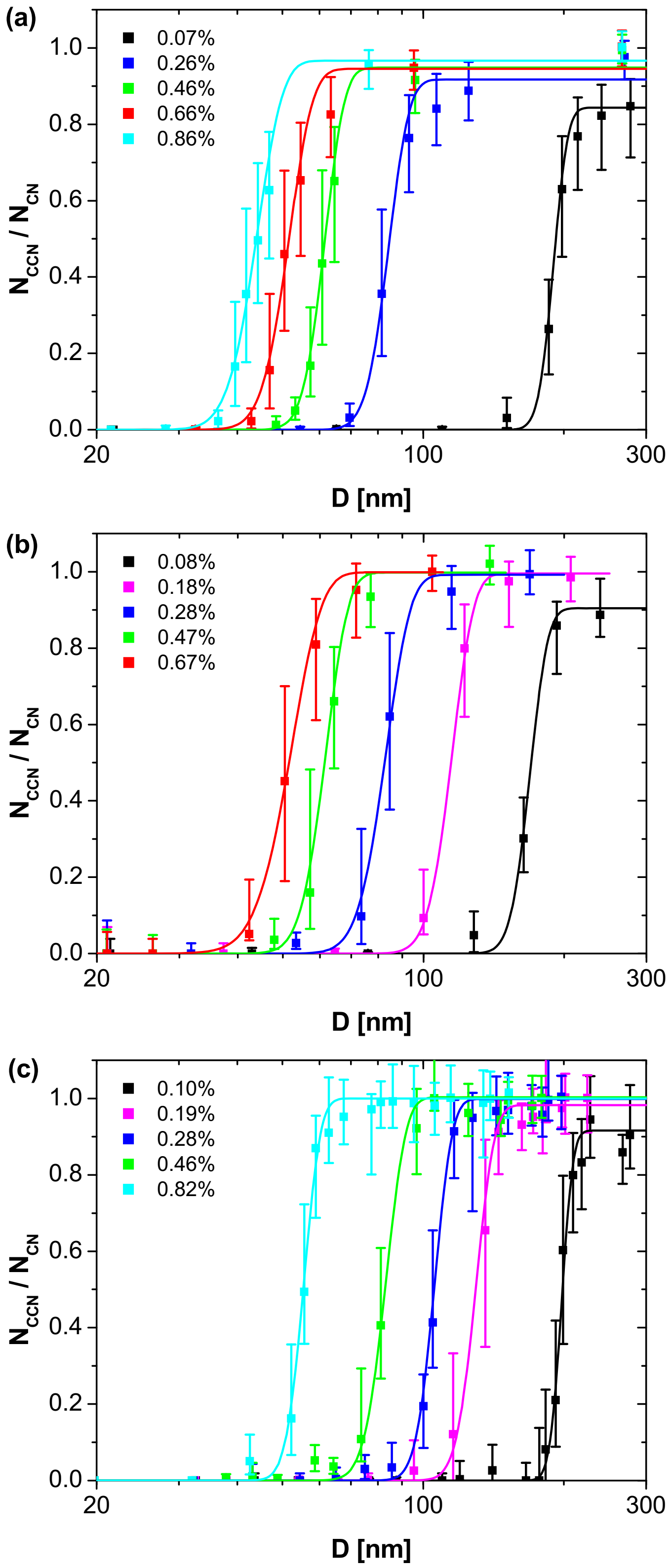

Figure C.1: Average CCN efficiency spectra for **(a)** the CAREBeijing-2006 campaign, **(b)** the CLACE-6 campaign, and **(c)** the AMAZE-08 campaign. The data points are median values calculated from CDF fits to all measured spectra at the particle diameters initially selected by the DMA (20–290 nm). The error bars extend from the lower to the upper quartile, and the lines are 3-parameter CDF fits to the data points (analogous to Fig. 3.3).

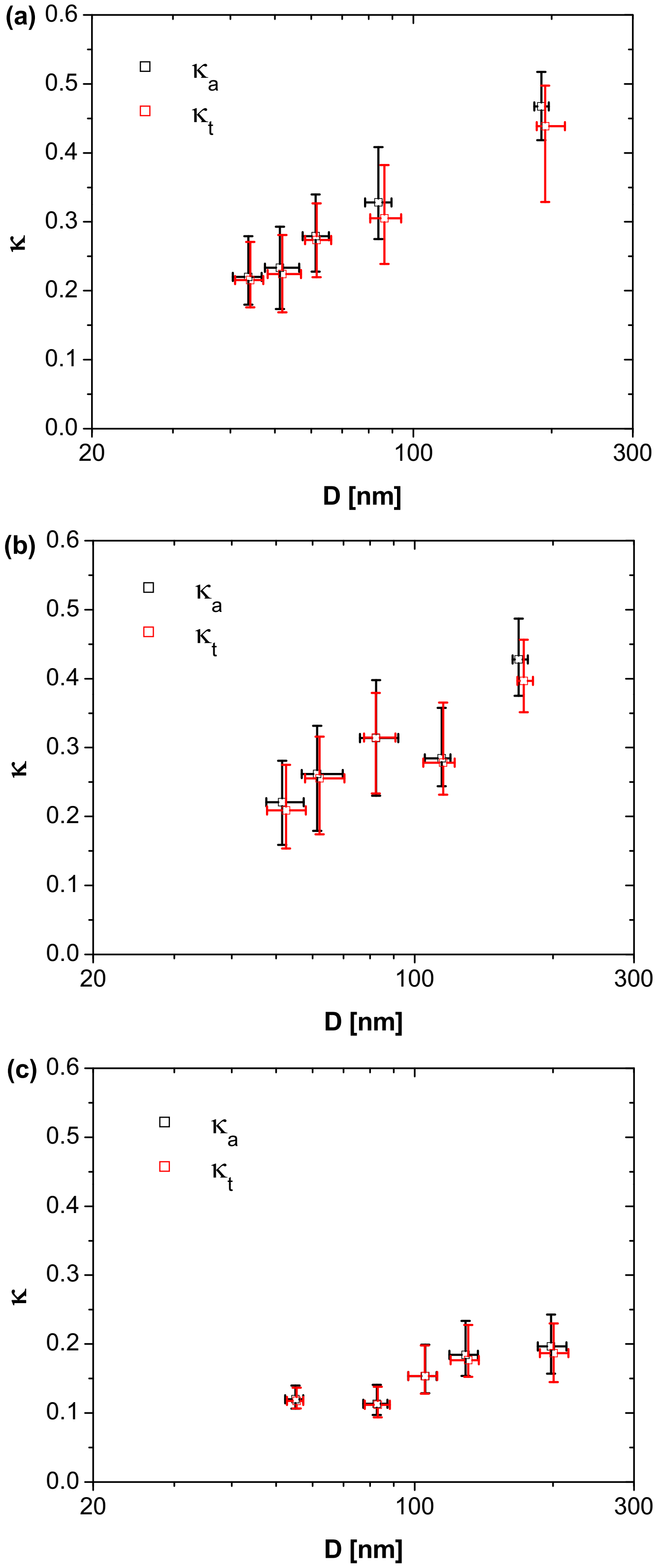

Figure C.2: Average effective hygroscopicity parameters for **(a)** the CAREBeijing-2006 campaign, **(b)** the CLACE-6 campaign, and **(c)** the AMAZE-08 campaign. κ_a and κ_t are plotted against the midpoint activation diameter (D_a or D_t, respectively). The data points are median values corresponding to a given level of supersaturation, and the error bars extend from the lower to the upper quartile (analogous to Fig. 3.4 b).

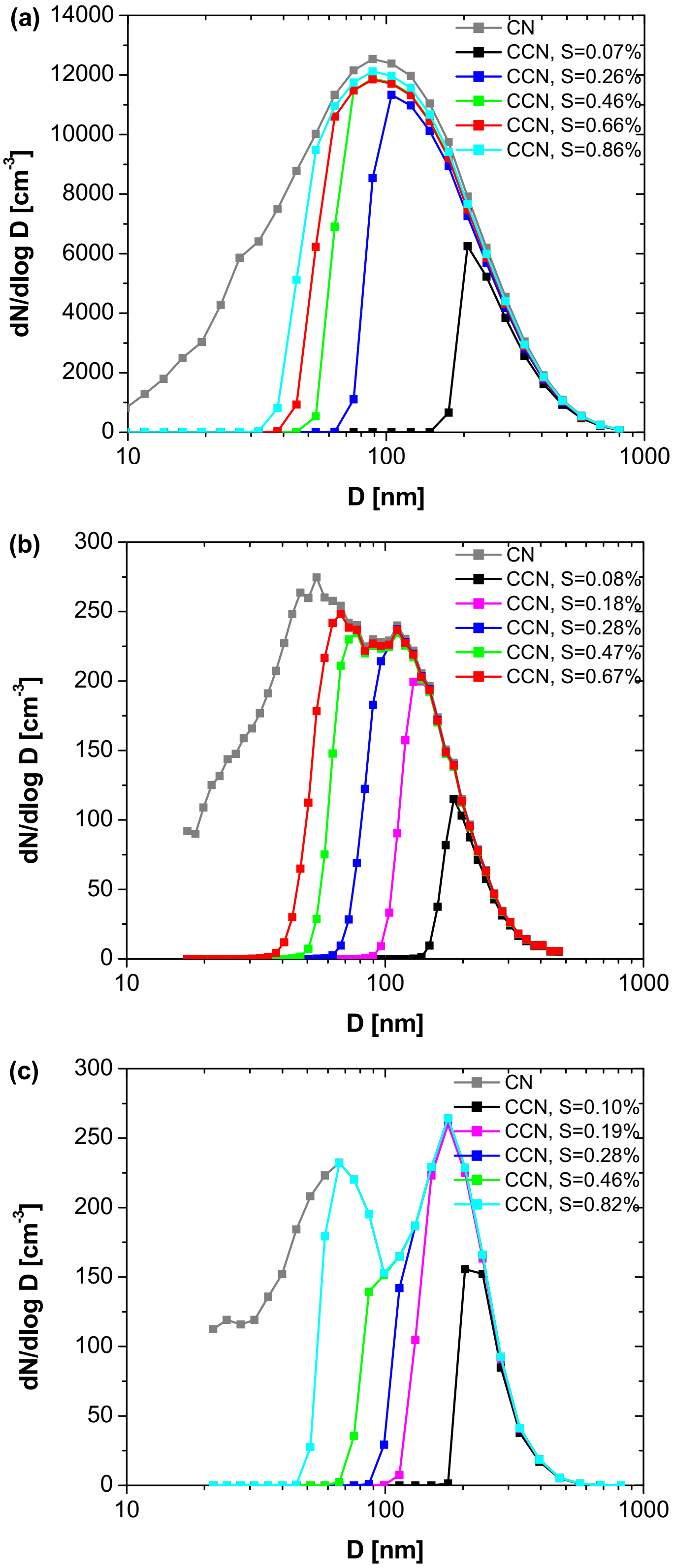

Figure C.3: Average number size distribution of total aerosol particles (CN) and cloud condensation nuclei (CCN) for **(a)** the CAREBeijing-2006 campaign, **(b)** the CLACE-6 campaign, and **(c)** the AMAZE-08 campaign. The CCN size distributions were calculated by multiplying the median CN size distribution with the median CCN efficiency spectra from Fig. C.1 (analogous to Fig. 3.7). Note, that the scale of the y-axis in (a) is different from the ones in (b) and (c).

List of Symbols

The following list explains the symbols most frequently used in this thesis.

Symbol	Unit	Quantity
a_w		water activity
c_s	mol L^{-1}	molarity of solute
D	m	dry particle diameter
D_a	m	midpoint activation diameter determined by 3-parameter CDF fit
D_B	m	mobility equivalent diameter
D_c	m	critical dry particle diameter
D_m	m	mass equivalent diameter
D_s	m	mass equivalent diameter of dry solute particle
D_t	m	midpoint activation diameter determined by 2-parameter CDF fit
D_wet	m	droplet diameter
f_inorg		mass fraction of inorganic ions (SO_4^{2-}, NH_4^+, NO_3^-, Cl^-)
f_org		organic mass fraction
g_s		particle growth factor
i_s		van’t Hoff factor of solute
$\mathrm{MAF_f}$		maximum activated fraction determined by 3-parameter CDF fit
$\mathrm{MAF_m}$		activated fraction measured at the largest selected diameter (∼270 nm)
m_D	kg	AMS mass concentrations integrated over the size interval of $D_\mathrm{a}-\sigma_\mathrm{a}$ to $D_\mathrm{a}+\sigma_\mathrm{a}$
m_s	kg	mass of dry solute
M_s	kg mol^{-1}	molar mass of solute
m_w	kg	mass of water
M_w	kg mol^{-1}	molar mass of water
N_CCN	cm^{-3}	number concentration of CCN in a size bin
$N_\mathrm{CCN,S}$	cm^{-3}	observed total number concentration of CCN at S
$N_\mathrm{CCN,S,p}$	cm^{-3}	predicted total number concentration of CCN at S
N_CN	cm^{-3}	number concentration of CN in a size bin
$N_\mathrm{CN,tot}$	cm^{-3}	total number concentration of CN
n_s	mol	number of moles of solute
n_w	mol	number of moles of water
p	Pa	pressure
Q	L min^{-1}	total flow rate of CCNC
R	J K^{-1} mol^{-1}	universal gas constant
RH	%	relative humidity
R_T	K W^{-1}	thermal resistance of CCNC
s		water vapor saturation ratio
s_c		critical water vapor saturation ratio
S	%	water vapor supersaturation
S_c	%	critical water vapor supersaturation
S_eff	%	effective supersaturation of water vapor in CCNC

Symbol	Unit	Quantity
T	K	absolute temperature
T_1	K	CCNC column top temperature
T_2	K	CCNC column middle temperature
T_3	K	CCNC column bottom temperature
x_s		mass fraction of solute in the droplet
χ		dynamic shape factor
ΔT	K	temperature difference at the outer wall of the CCNC column
ΔT^*	K	flow model temperature difference
ΔT_0	K	temperature difference offset
ΔT_inner	K	temperature difference inside the CCNC column
η		thermal efficiency of the CCNC
κ		effective hygroscopicity parameter
κ_a		effective hygroscopicity parameter derived from D_a (characteristic for CCN-active particles)
$\kappa_\mathrm{a,p}$		predicted κ_a value as calculated from Eq. (3.2)
κ_soot		effective hygroscopicity of soot particles
κ_t		effective hygroscopicity parameter derived from D_t (proxy for total ensemble of particles)
$\kappa_\mathrm{t,p}$		predicted κ_t value as calculated from Eq. (3.4), (3.5), or (3.6)
λ	m	mean free path
μ_s	mol kg^{-1}	molality of solute
ν_s		stoichiometric dissociation number of solute
ϕ_lv		number fraction of particles of low volatility
Φ_s		molal or practical osmotic coefficient of solute
ρ_s	kg m^{-3}	density of dry solute
ρ_sol	kg m^{-3}	density of solution droplet
ρ_w	kg m^{-3}	density of pure water
σ_sol	J m^{-2}	surface tension of solution droplet
σ_w	J m^{-2}	surface tension of pure water

List of Tables

List of Figures

Bibliography

Andreae, M. O.: Correlation between cloud condensation nuclei concentration and aerosol optical thickness in remote and polluted regions, Atmos. Chem. Phys., 9, 543–556, 2009.

Andreae, M. O. and Rosenfeld, D.: Aerosol-cloud-precipitation interactions. Part 1. The nature and sources of cloud-active aerosols, Earth Sci. Rev., 89, 13–41, 2008.

Andreae, M. O., Jones, C. D., and Cox, P. M.: Strong present-day aerosol cooling implies a hot future, Nature, 435, 1187–1190, 2005.

Andreae, M. O., Hegg, D., Feichter, J., Kloster, S., Levin, Z., Liousse, C., Radke, L., and Stier, P.: Sources and nature of atmospheric aerosols, in: Scientific assessment of the effects of aerosols on precipitation, edited by Levin, Z. and Cotton, W., World Meteorological Organization, 2007.

Andreae, M. O., Schmid, O., Yang, H., Yu, J., Zeng, L., and Zhang, Y.: Optical properties and chemical composition of the atmospheric aerosol in urban Guangzhou, China, Atmos. Environ., 42, 6335–6350, doi:10.1016/j.atmosenv.2008.01.030, 2008.

Bilde, M. and Svenningsson, B.: CCN activation of slightly soluble organics: the importance of small amounts of inorganic salt and particle phase, Tellus B, 56, 128–134, 2004.

Biskos, G., Paulsen, D., Russell, L. M., Buseck, P. R., and Martin, S. T.: Prompt deliquescence and efflorescence of aerosol nanoparticles, Atmos. Chem. Phys., 6, 4633–4642, 2006a.

Biskos, G., Russell, L. M.and Buseck, P. R., and Martin, S. T.: Nanosize effect on the hygroscopic growth factor of aerosol particles, Geophys. Res. Lett., 33, doi:10.1029/2005GL025199, 2006b.

Bougiatioti, A., Fountoukis, C., Kalivitis, N., Pandis, S. N., Nenes, A., and Mihalopoulos, N.: Cloud condensation nuclei measurements in the marine boundary layer of the Eastern Mediterranean: CCN closure and droplet growth kinetics, Atmos. Chem. Phys., 9, 7053–7066, 2009.

Brechtel, F. J. and Kreidenweis, S. M.: Predicting Particle Critical Supersaturation from Hygroscopic Growth Measurements in the Humidified TDMA. Part I: Theory and Sensitivity Studies, J. Atmos. Sci., 57, 1854–1871, 2000.

Broekhuizen, K., Pradeep Kumar, P., and Abbatt, J. P. D.: Partially soluble organics as cloud condensation nuclei: Role of trace soluble and surface active species, Geophys. Res. Lett., 31, doi: 10.1029/2003GL018203, 2004.

Broekhuizen, K., Chang, R.-W., Leaitch, W. R., Li, S.-M., and Abbatt, J. P. D.: Closure between measured and modeled cloud condensation nuclei (CCN) using size-resolved aerosol compositions in downtown Toronto, Atmos. Chem. Phys., 6, 2513–2524, 2006.

Burtscher, H., Baltensperger, U., Bukowiecki, N., Cohn, P., Hüglin, C., Mohr, M., Matter, U., Nyeki, S., Schmatloch, V., and Streit, N.: Separation of volatile and non-volatile aerosol fractions by thermodesorption: instrumental development and applications, J. Aerosol Sci., 32, 427–442, 2001.

Chan, M. N. and Chan, C. K.: Mass transfer effects in hygroscopic measurements of aerosol particles, Atmos. Chem. Phys., 5, 2703–2712, 2005.

Chang, R. Y.-W., Slowik, J. G., Shantz, N. C., Vlasenko, A., Liggio, J., Sjostedt, S. J., Leaitch, W. R., and Abbatt, J. P. D.: The hygroscopicity parameter (κ) of ambient organic aerosol at a field site subject to biogenic and anthropogenic influences: relationship to degree of aerosol oxidation, Atmos. Chem. Phys., 10, 5047–5064, 2010.

Charlson, R. J., Seinfeld, J. H., Nenes, A., Kulmala, M., Laaksonen, A., and Facchini, M. C.: Reshaping the theory of cloud formation, Science, 292, 2025–2026, 2001.

Chen, J.-P.: Theory of Deliquescence and Modified Köhler Curves, J. Atmos. Sci., 51, 3505–3516, 1994.

Cheng, Y. F., Eichler, H., Wiedensohler, A., Heintzenberg, J., Zhang, Y. H., Hu, M., Herrmann, H., Zeng, L. M., Liu, S., Gnauk, T., Brüggemann, E., and He, L. Y.: Mixing state of elemental carbon and non-light-absorbing aerosol components derived from in situ particle optical properties at Xinken in Pearl River Delta of China, J. Geophys. Res., 111, doi:10.1029/2005JD006929, 2006.

Cheng, Y. F., Berghof, M., Garland, R. M., Wiedensohler, A., Wehner, B., Su, H., Achtert, P., Nowak, A., Pöschl, U., Zhang, Y. H., Zhu, T., and Zeng, L. M.: Influence of soot mixing state on aerosol light absorption and single scattering albedo during air mass aging at a polluted regional site in northeastern China, J. Geophys. Res., 114, doi:10.1029/2008JD010883, 2009.

Chuang, P. Y., Collins, D. R., Pawlowska, H., Snider, J. R., Jonsson, H. H., Brenguier, J. L., Flagan, R. C., and Seinfeld, J. H.: CCN measurements during ACE-2 and their relationship to cloud microphysical properties, Tellus B, 52, 843–867, 2000.

Clegg, S. L. and Wexler, A.: Interactive comment on "Calibration and measurement uncertainties of a continuous-flow cloud condensation nuclei counter (DMT–CCNC): CCN activation of ammonium sulfate and sodium chloride aerosol particles in theory and experiment" by D. Rose et al., Atmos. Chem. Phys. Discuss., 7, S4180–S4183, 2007.

Clegg, S. L., Brimblecombe, P., and Wexler, A. S.: Thermodynamic model of the system H^+ – NH_4^+ – SO_4^{2-} – NO^{3-} – H_2O at tropospheric temperatures, J. Phys. Chem. A, 102, 2137–2154, 1998a.

Clegg, S. L., Brimblecombe, P., and Wexler, A. S.: A thermodynamic model of the system H^+ – NH_4^+ – Na^+ – SO_4^{2-} – NO^{3-} – Cl^- – H_2O at 298.15 K, J. Phys. Chem. A, 102, 2155–2171, 1998b.

DeCarlo, P. F., Slowik, J. G., Worsnop, D. R., Davidovits, P., and Jimenez, J. L.: Particle Morphology and Density Characterization by Combined Mobility and Aerodynamic Diameter Measurements. Part 1: Theory, Aerosol Sci. Technol., 38, 1185–1205, 2004.

Delene, D. J. and Deshler, T.: Calibration of a photometric cloud condensation nucleus counter designed for deployment on a balloon package, J. Atmos. Oceanic Technol., 17, 459–467, 2000.

Delene, D. J. and Deshler, T.: Vertical profiles of cloud condensation nuclei above Wyoming, J. Geophys. Res., 106, 12,579–12,588, 2001.

Deng, X., Tie, X., Wu, D., Zhou, X., Bi, X., Tan, H., Li, F., and Jiang, C.: Long-term trend of visibility and its characterizations in the Pearl River Delta (PRD) region, China, Atmos. Environ., 42, 1424–1435, 2008.

Dinar, E., Taraniuk, I., Graber, E. R., Katsman, S., Moise, T., Anttila, T., Mentel, T. F., and Rudich, Y.: Cloud condensation nuclei properties of model and atmospheric HULIS, Atmos. Chem. Phys., 6, 2465–2481, 2006.

Dusek, U., Frank, G. P., Hildebrandt, L., Curtius, J., Schneider, J., Walter, S., Chand, D., Drewnick, F., Hings, S., Jung, D., Borrmann, S., and Andreae, M. O.: Size matters more than chemistry for cloud nucleating ability of aerosol particles, Science, 312, 1375–1378, 2006.

Dusek, U., Frank, G. P., Curtius, J., Drewnick, F., Schneider, J., Kürten, A., Rose, D., Andreae, M. O., Borrmann, S., , and Pöschl, U.: Enhanced organic mass fraction and decreased hygroscopicity of cloud condensation nuclei (CCN) during new particle formation events, Geophys. Res. Lett., 37, doi:10.1029/2009GL040930, 2010.

Engelhart, G. J., Asa-Awuku, A., Nenes, A., and Pandis, S. N.: CCN activity and droplet growth kinetics of fresh and aged monoterpene secondary organic aerosol, Atmos. Chem. Phys., 8, 3937–3949, 2008.

Ervens, B., Cubison, M., Andrews, E., Feingold, G., Ogren, J., Jimenez, J., DeCarlo, P., and Nenes, A.: Prediction of cloud condensation nucleus number concentration using measurements of aerosol size distributions and composition and light scattering enhancement due to humidity, J. Geophys. Res., 112, 2007.

Ervens, B., Cubison, M. J., Andrews, E., Feingold, G., Ogren, J. A., Jimenez, J. L., Quinn, P. K., Bates, T. S., Wang, J., Zhang, Q., Coe, H., Flynn, M., and Allan, J. D.: CCN predictions using simplified assumptions of organic aerosol composition and mixing state: a synthesis from six different locations, Atmos. Chem. Phys., 10, 4795–4807, 2010.

Fan, S., Wang, B., Tesche, M., Engelmann, R., Althausen, A., Liu, J., Zhu, W., Fan, Q., Li, M.-H., Ta, N., Song, L., and Leong, K.: Meteorological conditions and structures of atmospheric boundary layer in October 2004 over Pearl River Delta area, Atmos. Environ., 42, 61746186, 2008.

Frank, G. P., Dusek, U., and Andreae, M. O.: Technical note: A method for measuring size-resolved CCN in the atmosphere, Atmos. Chem. Phys. Discuss., 6, 4879–4895, 2006.

Frank, G. P., Dusek, U., and Andreae, M. O.: Characterization of a static thermal-gradient CCN counter, Atmos. Chem. Phys., 7, 3071–3080, 2007.

Frey, A., Rose, D., Wehner, B., Müller, T., Cheng, Y., Wiedensohler, A., and Virkkula, A.: Application of the Volatility-TDMA Technique to Determine the Number Size Distribution and Mass Concentration of Less Volatile Particles, Aerosol Sci. Technol., 42, 817–828, 2008.

Garland, R. M., Yang, H., Schmid, O., Rose, D., Nowak, A., Achtert, P., Wiedensohler, A., Takegawa, N., Kita, K., Miyazaki, Y., Kondo, Y., Hu, M., Shao, M., Zeng, L. M., Zhang, Y. H., Andreae,

M. O., and Pöschl, U.: Aerosol optical properties in a rural environment near the mega-city Guangzhou, China: implications for regional air pollution, radiative forcing and remote sensing, Atmos. Chem. Phys., 8, 5161–5186, 2008.

Garland, R. M., Schmid, O., Nowak, A., Achtert, P., Wiedensohler, A., Gunthe, S. S., Takegawa, N., Kita, K., Kondo, Y., Hu, M., Shao, M., Zeng, L. M., Zhu, T., Andreae, M. O., and Pöschl, U.: Aerosol optical properties observed during Campaign of Air Quality Research in Beijing 2006 (CAREBeijing-2006): Characteristic differences between the inflow and outflow of Beijing city air, J. Geophys. Res., 114, doi:10.1029/2008JD010780, 2009.

Gerber, H. E., Hoppel, W. A., and Wojciechowski, T. A.: Experimental verification of the theoretical relationship between size and critical supersaturation of salt nuclei, J. Atmos. Sci, 34, 18361841, 1977.

Giebl, H., Berner, A., Reischl, G., Puxbaum, H., Kasper-Giebl, A., and Hitzenberger, R.: CCN activation of oxalic and malonic acid test aerosols with the University of Vienna cloud condensation nuclei counter, J. Aerosol Sci., 33, 1623–1634, 2002.

Gras, J. L.: CN, CCN and particle size in Southern Ocean air at Cape Grim, Atmos. Res., 35, 233–251, 1995.

Gunthe, S. S., King, S. M., Rose, D., Chen, Q., Roldin, P., Farmer, D. K., Jimenez, J. L., Artaxo, P., Andreae, M. O., Martin, S. T., and Pöschl, U.: Cloud condensation nuclei in pristine tropical rainforest air of Amazonia: size-resolved measurements and modeling of atmospheric aerosol composition and CCN activity, Atmos. Chem. Phys., 9, 7551–7575, 2009.

Gysel, M., Weingartner, E., and Baltensperger, U.: Hygroscopicity of Aerosol Particles at Low Temperatures. 2. Theoretical and Experimental Hygroscopic Properties of Laboratory Generated Aerosols, Environ. Sci. Technol., 36, 63–68, 2002.

Hagler, G. S., Bergin, M. H., Salmon, L. G., Yu, J. Z., Wan, E. C. H., Zheng, M., Zeng, L. M., Kiang, C. S., Zhang, Y. H., Lau, A. K. H., and Schauer, J. J.: Source areas and chemical composition of fine particulate matter in the Pearl River Delta region of China, Atmos. Environ., 40, 3802–3815, 2006.

Hänel, G.: The properties of atmospheric aerosol particles in function of the relative humidity at thermodynamic equilibrium with the scattering moist air, Adv. Geophys., 19, 188, 1976.

Heintzenberg, J. and Charlson, R. J.: Clouds in the Perturbed Climate System: Their Relationship to Energy Balance, Atmospheric Dynamics, and Precipitation, Strüngmann Forum Report, vol. 2, MIT Press, Cambridge, MA, 2009.

Henning, S., Rosenoern, T., D'Anna, B., Gola, A. A., Svenningsson, B., and Bilde, M.: Cloud droplet activation and surface tension of mixtures of slightly soluble organics and inorganic salt, Atmos. Chem. Phys., 5, 575–582, 2005.

Henning, S., Wex, H., Hennig, T., Kiselev, A., Snider, J., Rose, D., Dusek, U., Frank, G. P., Pöschl, U., Kristensson, A., Bilde, M., Tillmann, R., Kiendler-Scharr, A., Mentel, T. F., Walter, S., Schneider, J., Wennrich, C., and Stratmann, F.: Soluble mass, hygroscopic growth and droplet activation of coated soot particles during LExNo, J. Geophys. Res., 115, doi:10.1029/2009JD012626, 2010.

Hua, W., Chen, Z. M., Jie, C. Y., Kondo, Y., Hofzumahaus, A., Takegawa, N., Chang, C. C., Lu, K. D., Miyazaki, Y., Kita, K., Wang, H. L., Zhang, Y. H., and Hu, M.: Atmospheric hydrogen peroxide and organic hydroperoxides during PRIDE-PRD'06, China: their concentration, formation mechanism and contribution to secondary aerosols, Atmos. Chem. Phys., 8, 6755–6773, 2008.

Huang, Y., Chameides, W. L., and Dickinson, R. E.: Direct and indirect effects of anthropogenic aerosols on regional precipitation over east Asia, J. Geophys. Res., 112, doi: 10.1029/2006JD007114, 2007.

Hudson, J. G.: An Instantaneous CCN Spectrometer, J. Atmos. Oceanic Technol., 6, 1055–1065, 1989.

Hudson, J. G.: Cloud condensation nuclei, J. Appl. Met., 32, 596–607, 1993.

Hudson, J. G. and Xie, Y. H.: Vertical distributions of cloud condensation nuclei spectra over the summertime northeast Pacific and Atlantic Oceans, J. Geophys. Res., 104, 30,219–30,229, 1999.

Hudson, J. G. and Yum, S. S.: Cloud condensation nuclei spectra and polluted and clean clouds over the Indian Ocean, J. Geophys. Res., 107, 2002.

IAPSAG: WMO/IUGG International Aerosol Precipitation Science Assessment Group (IAPSAG) Report: Aerosol Pollution Impact on Precipitation: A Scientific Review, Tech. rep., World Meteorological Organization, 2007.

IPCC: Climate Change 2007: The Physical Science Basis. Contribution of Working Group I to the Fourth Assessment Report of the Intergovernmental Panel on Climate Change, p. 996, Cambridge University Press, Cambridge and New York, 2007.

Jaenicke, R.: Aerosol cloud climate interaction, Tropospheric aerosols, edited by Hobbs, P. V., Academic Press, San Diego, CA, pp. 1–31, 1993.

Jayne, J. T., Leard, D. C., Zhang, X. F., Davidovits, P., Smith, K. A., Kolb, C. E., and Worsnop, D. R.: Development of an aerosol mass spectrometer for size and composition analysis of submicron particles, Aerosol Sci. Technol., 33, 49–70, 2000.

King, S. M., Rosenø ern, T., Shilling, J. E., Chen, Q., and Martin, S. T.: Increased cloud activation potential of secondary organic aerosol for atmospheric mass loadings, Atmos. Chem. Phys., 9, 2959–2971, 2009.

King, S. M., Rosenoern, T., Shilling, J. E., Chen, Q., Wang, Z., Biskos, G., McKinney, K. A., Pöschl, U., and Martin, S. T.: Cloud droplet activation of mixed organic-sulfate particles produced by the photooxidation of isoprene, Atmos. Chem. Phys., 10, 3953–3964, 2010.

Knutson, E. O. and Whitby, K. T.: Aerosol classification by electric mobility: apparatus, theory, and applications, J. Aerosol Sci., 6, 443–451, 1975.

Koehler, K. A., Kreidenweis, S. M., DeMott, P. J., Prenni, A. J., Carrico, C. M., Ervens, B., and Feingold, G.: Water activity and activation diameters from hygroscopicity dataPart II: Application to organic species, Atmos. Chem. Phys., 6, 795–809, 2006.

Köhler, H.: The nucleus in and the growth of hygroscopic droplets, Trans. Farad. Soc., 32, 1152–1161, 1936.

Kondo, Y., Komazaki, Y., Miyazaki, Y., Moteki, N., Takegawa, N., Kodama, D., Deguchi, S., Nogami, M., Fukuda, M., and Miyakawa, T.: Temporal variations of elemental carbon in Tokyo, J. Geophys. Res, 111, D12 205, 2006.

Krämer, L., Pöschl, U., and Niessner, R.: Microstructural rearrangement of sodium chloride condensation aerosol particles on interaction with water vapor, J. Aerosol Sci., 31, 673–685, 2000.

Kreidenweis, S. M., Koehler, K., DeMott, P. J., Prenni, A. J., Carrico, C., and Ervens, B.: Water activity and activation diameters from hygroscopicity dataPart I: Theory and application to inorganic salts, Atmos. Chem. Phys., 5, 13571370, 2005.

Kreidenweis, S. M., Petters, M. D., and DeMott, P. J.: Single-parameter estimates of aerosol water content, Environ. Res. Lett., 3, doi:10.1088/1748-9326/3/3/035002, 2008.

Kreidenweis, S. M., Petters, M. D., and Chuang, P. Y.: Cloud particle precursors, in: Clouds in the Perturbed Climate System: Their Relationship to Energy Balance, Atmospheric Dynamics, and Precipitation, Strüngmann Forum Report, vol. 2, edited by: Heintzenberg, J. and Charlson, R. J., MIT Press, Cambridge, MA, 2009.

Kuwata, M., Kondo, Y., Mochida, M., Takegawa, N., and Kawamura, K.: Dependence of CCN activity of less volatile particles on the amount of coating observed in Tokyo, J. Geophys. Res., 112, doi:10.1029/2006JD007758, 2007.

Kuwata, M., Kondo, Y., Miyazaki, Y., Komazaki, Y., Kim, J. H., Yum, S. S., Tanimoto, H., and Matsueda, H.: Cloud condensation nuclei activity at Jeju Island, Korea in spring 2005, Atmos. Chem. Phys., 8, 2933–2948, 2008.

Kuwata, M., Kondo, Y., and Takegawa, N.: Critical condensed mass for activation of black carbon as cloud condensation nuclei in Tokyo, J. Geophys. Res., 114, doi:10.1029/2009JD012086, 2009.

Lance, S., Medina, J., Smith, J. N., and Nenes, A.: Mapping the Operation of the DMT Continuous Flow CCN Counter, Aerosol Sci. Technol., 40, 242–254, 2006.

Lance, S., Nenes, A., Mazzoleni, C., Dubey, M. K., Gates, H., Varutbangkul, V., Rissman, T. A., Murphy, S. M., Sorooshian, A., Flagan, R. C., Seinfeld, J. H., Feingold, G., and Jonsson, H. H.: Cloud condensation nuclei activity, closure, and droplet growth kinetics of Houston aerosol during the Gulf of Mexico Atmospheric Composition and Climate Study (GoMACCS), J. Geophys. Res., 114, doi:10.1029/2008JD011699, 2009.

Li, Z. Q., Xia, X., Cribb, M., Mi, W., Holben, B., Wang, P., Chen, H., Tsay, S. C., Eck, T. F., Zhao, F., Dutton, E. G., and Dickerson, R. E.: Aerosol optical properties and their radiative effects in northern China, J. Geophys. Res., 112, doi:10.1029/2006JD007382, 2007.

Liu, B. H., Xu, M., Henderson, M., Qi, Y., and Li, Y. Q.: Taking China's temperature: Daily range, warming trends, and regional variations, 1955–2000, J. Climate, 17, 4453–4462, 2004.

Lohmann, U. and Feichter, J.: Global indirect aerosol effects: a review, Atmos. Chem. Phys., 5, 715–737, 2005.

Low, R. D. H.: A theoretical study of nineteen condensation nuclei, J. de Rech. Atmos., 4, 65–78, 1969.

Massie, S. T., Torres, O., and Smith, S. J.: Total Ozone Mapping Spectrometer (TOMS) observations of increases in Asian aerosol in winter from 1979 to 2000, J. Geophys. Res., 109, D18 211, doi:10.1029/2004JD004 620, 2004.

Matsumoto, K., Tanaka, H., Nagao, I., and Ishizaka, Y.: Contribution of particulate sulfate and organic carbon to cloud condensation nuclei in the marine atmosphere, Geophys. Res. Lett., 24, 655–658, 1997.

McDonald, J. E.: Erroneous cloud physics use of Raoult's Law, J. Met., 10, 416–433, 1953.

McFiggans, G., Artaxo, P., Baltensperger, U., Coe, H., Facchini, M. C., Feingold, G., Fuzzi, S., Gysel, M., Laaksonen, A., Lohmann, U., Mentel, T. F., Murphy, D. M., O'Dowd, C. D., Snider, J. R., and Weingartner, E.: The effect of physical and chemical aerosol properties on warm cloud droplet activation, Atmos. Chem. Phys., 6, 2593–2649, 2006.

Mikhailov, E., Vlasenko, S., Niessner, R., and Pöschl, U.: Interaction of aerosol particles composed of protein and salts with water vapor: hygroscopic growth and microstructural rearrangement, Atmos. Chem. Phys., 4, 323350, 2004.

Mikhailov, E., Vlasenko, S., Martin, S. T., Koop, T., and Pöschl, U.: Amorphous and crystalline aerosol particles interacting with water vapor: conceptual framework and experimental evidence for restructuring, phase transitions and kinetic limitations, Atmos. Chem. Phys., 9, 9491–9522, 2009.

Mokbel, I., Ye, S., Jose, J., and Xans, P.: Study of non ideality of various aqueous sodium chloride solutions by vapor pressures measurements and correlation of experimental results by Pitzer's method, J. Chim. Phys., 94, 122137, 1997.

Niedermeier, D., Wex, H., Voigtländer, J., Stratmann, F., Brüggemann, E., Kiselev, A., Henk, H., and Heintzenberg, J.: LACIS-measurements and parameterization of sea-salt particle hygroscopic growth and activation, Atmos. Chem. Phys., 8, 579–590, 2008.

Padró, L. T., Asa-Awuku, A., Morrison, R., and Nenes, A.: Inferring thermodynamic properties from CCN activation experiments: single-component and binary aerosols, Atmos. Chem. Phys., 7, 5263–5274, 2007.

Petters, M. D. and Kreidenweis, S. M.: A single parameter representation of hygroscopic growth and cloud condensation nucleus activity, Atmos. Chem. Phys., 7, 19611971, 2007.

Petters, M. D. and Kreidenweis, S. M.: A single parameter representation of hygroscopic growth and cloud condensation nucleus activity - Part 2: Including solubility, Atmos. Chem. Phys., 8, 6273–6279, 2008.

Petters, M. D., Prenni, A. J., Kreidenweis, S. M., and DeMott, P. J.: On measuring the critical diameter of cloud condensation nuclei using mobility selected aerosol, Aerosol Sci. Technol., 41, 907–913, 2007.

Petters, M. D., Carrico, C. M., Kreidenweis, S. M., Prenni, A. J., DeMott, P. J., Collett Jr., J. L., and Moosmüller, H.: Cloud condensation nucleation activity of biomass burning aerosol, J. Geophys. Res., 114, doi:10.1029/2009JD012353, 2009.

Philippin, S., Wiedensohler, A., and Stratmann, F.: Measurements of non-volatile fractions of pollution aerosols with an eight-tube volatility tandem differential mobility analyzer (VTDMA-8), J. Aerosol Sci., 35, 185–203, doi:10.1016/j.jaerosci.2003.07.004, 2004.

Pitzer, K. S. and Mayorga, G.: Thermodynamics of electrolytes. II. Activity and osmotic coefficients for strong electrolytes with one or both ions univalent, J. Phys. Chem., 77, 2300–2308, 1973.

Pöschl, U., Rose, D., and Andreae, M. O.: Climatologies of cloud-related aerosols - Part 2: Particle hygroscopicity and cloud condensation nucleus activity, in: Clouds in the Perturbed Climate System: Their Relationship to Energy Balance, Atmospheric Dynamics, and Precipitation, Strüngmann Forum Report, vol. 2, edited by: Heintzenberg, J. and Charlson, R. J., MIT Press, Cambridge, MA, pp. 57–72, 2009.

Pradeep Kumar, P., Broekhuizen, K., and Abbatt, J. P. D.: Organic acids as cloud condensation nuclei: Laboratory studies of highly soluble and insoluble species, Atmos. Chem. Phys., 3, 509–520, 2003.

Pringle, K. J., Tost, H., Pozzer, A., Pöschl, U., and Lelieveld, J.: Global distribution of the effective aerosol hygroscopicity parameter for CCN activation, Atmos. Chem. Phys., 10, 5241–5255, 2010.

Pruppacher, H. R. and Klett, J. D.: Microphysics of clouds and precipitation, Kluwer Academic Publishers, Dordrecht, 1997.

Qian, Y., Kaiser, D. P., Leung, L. R., and Xu, M.: More frequent cloud-free sky and less surface solar radiation in China from 1955 to 2000, Geophys. Res. Lett., 33, doi:10.1029/2005GL024586, 2006.

Raymond, T. M. and Pandis, S. N.: Formation of cloud droplets by multicomponent organic particles, J. Geophys. Res., 108, 2003.

Reade, L., Jennings, S. G., and McSweeney, G.: Cloud condensation nuclei measurements at Mace Head, Ireland, over the period 1994-2002, Atmos. Res., 82, 610–621, 2006.

Reid, J. S., Koppmann, R., Eck, T. F., and Eleuterio, D. P.: A review of biomass burning emissions part II: intensive physical properties of biomass burning particles, Atmos. Chem. Phys., 5, 799–825, 2005.

Reutter, P., Su, H., Trentmann, J., Simmel, M., Rose, D., Gunthe, S. S., Wernli, H., Andreae, M. O., and Pöschl, U.: Aerosol- and updraft-limited regimes of cloud droplet formation: influence of particle number, size and hygroscopicity on the activation of cloud condensation nuclei (CCN), Atmos. Chem. Phys., 9, 7067–7080, 2009.

Richter, A., Burrows, J. P., Nuss, H., Granier, C., and Niemeier, U.: Increase in tropospheric nitrogen dioxide over China observed from space, Nature, 437, 129–132, 2005.

Rissler, J., Vestin, A., Swietlicki, E., Fisch, G., Zhou, J., Artaxo, P., and Andreae, M. O.: Size distribution and hygroscopic properties of aerosol particles from dry-season biomass burning in Amazonia, Atmos. Chem. Phys., 6, 471–491, 2006.

Rissman, T. A., Varutbangkul, V., Surratt, J. D., Topping, D. O., McFiggans, G., Flagan, R. C., and Seinfeld, J. H.: Cloud condensation nucleus (CCN) behavior of organic aerosol particles generated by atomization of water and methanol solutions, Atmos. Chem. Phys., 7, 2949–2971, 2007.

Roberts, G., Artaxo, P., Zhou, J., Swietlicki, E., and Andreae, M. O.: Sensitivity of CCN spectra on chemical and physical properties of aerosol: A case study from the Amazon Basin, J. Geophys. Res., 107, 2002.

Roberts, G., Mauger, G., Hadley, O., and Ramanathan, V.: North American and Asian aerosols over the eastern Pacific Ocean and their role in regulating cloud condensation nuclei, J. Geophys. Res., 111, doi:10.1029/2005JD006661, 2006.

Roberts, G. C. and Nenes, A.: A Continuous-Flow Streamwise Thermal-Gradient CCN Chamber for Atmospheric Measurements, Aerosol Sci. Technol., 39, 206–221, 2005.

Roberts, G. C., Andreae, M. O., Zhou, J., and Artaxo, P.: Cloud condensation nuclei in the Amazon Basin: "Marine" conditions over a continent?, Geophys. Res. Lett., 28, 2807–2810, 2001.

Robinson, R. A. and Stokes, R. H.: Electrolyte Solutions, (revised), Butterworth, London, 1959.

Rose, D., Wehner, B., Ketzel, M., Engler, C., Voigtländer, J., Tuch, T., and Wiedensohler, A.: Atmospheric number size distributions of soot particles and estimation of emission factors, Atmos. Chem. Phys., 6, 1021–1031, 2006.

Rose, D., Frank, G. P., Dusek, U., Gunthe, S. S., Andreae, M. O., and Pöschl, U.: Interactive comment on "Calibration and measurement uncertainties of a continuous-flow cloud condensation nuclei counter (DMT–CCNC): CCN activation of ammonium sulfate and sodium chloride aerosol particles in theory and experiment" by D. Rose et al., Atmos. Chem. Phys. Discuss., 7, S4127–S4129, 2007.

Rose, D., Gunthe, S. S., Mikhailov, E., Frank, G. P., Dusek, U., Andreae, M. O., and Pöschl, U.: Calibration and measurement of a continuous-flow cloud condensation nuclei counter (DMT-CCNC): CCN activation of ammonium sulfate and sodium chloride aerosol particles in theory and experiment, Atmos. Chem. Phys., 8, 1153–1179, 2008.

Rose, D., Nowak, A., Achtert, P., Wiedensohler, A., Hu, M., Shao, M., Zhang, Y., Andreae, M. O., and Pöschl, U.: Cloud condensation nuclei in polluted air and biomass burning smoke near the mega-city Guangzhou, China - Part 1: Size-resolved measurements and implications for the modeling of aerosol particle hygroscopicity and CCN activity, Atmos. Chem. Phys., 10, 3365–3383, 2010a.

Rose, D., Nowak, A., Achtert, P., Wiedensohler, A., Hu, M., Shao, M., Zhang, Y., Andreae, M. O., and Pöschl, U.: Interactive comment on "Cloud condensation nuclei in polluted air and biomass burning smoke near the mega-city Guangzhou, China – Part 1: Size-resolved measurements and implications for the modeling of aerosol particle hygroscopicity and CCN activity" by D. Rose et al., Atmos. Chem. Phys. Discuss., 8, 2010b.

Rosenfeld, D., Dai, J., Yu, X., Yao, Z., Xu, X., Yang, X., and Du, C.: Inverse relations between amounts of air pollution and orographic precipitation, Science, 315, 1396–1398, 2007.

Rosenfeld, D., Lohmann, U., Raga, G. B., O'Dowd, C. D., Kulmala, M., Fuzzi, S., Reissell, A., and Andreae, M. O.: Flood or Drought: How Do Aerosols Affect Precipitation?, Science, 321, 1309–1313, 2008.

Scheibel, H. G. and Porstendörfer, J.: Generation of monodisperse Ag-and NaCl-aerosols with particle diameters between 2 and 300 nm, J. Aerosol Sci, 14, 113126, 1983.

Segal, Y. and Khain, A.: Dependence of droplet concentration on aerosol conditions in different cloud types: Application to droplet concentration parameterization of aerosol conditions, J. Geophys. Res., 111, doi:10.1029/2005JD006561, 2006.

Segal, Y., Khain, A., Pinsky, M., and Sterkin, A.: Sensitivity of raindrop formation in ascending cloud parcels to cloud condensation nuclei and thermodynamic conditions, Quart. J. Roy. Met. Soc., 130, 561–581, 2004.

Seinfeld, J. H. and Pandis, S. N.: Atmospheric Chemistry and Physics: From Air Pollution to Climate Change, John Wiley and Sons, Inc., New York, 2006.

Shantz, N. C., Chang, R. Y.-W., Slowik, J. G., Vlasenko, A., Abbatt, J. P. D., and Leaitch, W. R.: Slower CCN growth kinetics of anthropogenic aerosol compared to biogenic aerosol observed at a rural site, Atmos. Chem. Phys., 10, 299–312, 2010.

Shao, M., Tang, X., Zhang, Y., and Li, W.: City clusters in China: air and surface water pollution, Front. Ecol. Environ., 4, 353–361, 2006.

Shilling, J. E., King, S. M., Mochida, M., Worsnop, D. R., and Martin, S.: Mass Spectral Evidence that Small Changes in Composition Caused by Oxidative Aging Processes Alter Aerosol CCN Properties, J. Phys. Chem. A, 111, 3358–3368, 2007.

Smith, M. H. and O'Dowd, C. D.: Observations of accumulation mode aerosol composition and soot carbon concentrations by means of a high-temperature volatility technique, J. Geophys. Res, 101, 19 583–19 591, 1996.

Snider, J. R., Guibert, S., Brenguier, J. L., and Putaud, J. P.: Aerosol activation in marine stratocumulus clouds: 2. Köhler and parcel theory closure studies, J. Geophys. Res., 108, 2003.

Snider, J. R., Petters, M. D., Wechsler, P., and Liu, P. S. K.: Supersaturation in the Wyoming CCN instrument, J. Atmos. Oceanic Technol., 23, 1323–1339, 2006.

Snider, J. R., Wex, H., Rose, D., Kristensson, A., Stratmann, F., Hennig, T., Henning, S., Kiselev, A., Bilde, M., Burkhart, M., Dusek, U., Frank, G. P., Kiendler-Scharr, A., Mentel, T. F., Petters, M. D., and Pöschl, U.: Intercomparison of CCN and Hygroscopic Fraction Measurements from LExNo, J. Geophys. Res., 115, doi:10.1029/2009JD012618, 2010.

Stratmann, F., Bilde, M., Dusek, U., Frank, G. P., Hennig, T., Henning, S., Kiendler-Scharr, A., Kiselev, A., Kristensson, A., Lieberwirt, I., Mentel, T. F., Pöschl, U., Rose, D., Schneider, J., Snider, J., Tillmann, R., Walter, S., and H.Wex: Examination of Laboratory-Generated Coated Soot Particles: An Overview over the LExNo Campaign, J. Geophys. Res., 115, doi:10.1029/2009JD012628, 2010.

Streets, D. G., Tsai, N. Y., Akimoto, H., and Oka, K.: Sulfur dioxide emissions in Asia in the period 1985–1997, Atmos. Environ., 34, 4413–4424, 2000.

Streets, D. G., Yu, C., Wu, Y., Chin, M., Zhao, Z., Hayasaka, T., and Shi, G.: Aerosol trends over China, 1980–2000, Atmos. Res., 88, 174–182, 2008.

Takegawa, N., Miyakawa, T., Watanabe, M., Kondo, Y., Miyazaki, Y., Han, S., Zhao, Y., van Pinxteren, D., Brüggemann, E., Gnauk, T., Herrmann, H., Xiao, R., Deng, Z., Hu, M., Zhu, T., and Zhang, Y.: Performance of an Aerodyne Aerosol Mass Spectrometer (AMS) during Intensive Campaigns in China in the Summer of 2006, Aerosol Sci. Technol., 43, 189–204, doi: 10.1080/02786820802582251, 2009.

Tang, I. N.: Chemical and size effects of hygroscopic aerosols on light scattering coefficients, J. Geophys. Res., 101, 19 245–19 250, 1996.

Tang, I. N. and Munkelwitz, H. R.: Water activities, densities, and refractive indices of aqueous sulfates and sodium nitrate droplets of atmospheric importance, J. Geophys. Res., 99, 18 801–18 808, 1994.

Tsigaridis, K., Krol, M., Dentener, F. J., Balkanski, Y., Lathière, J., Metzger, S., Hauglustaine, D. A., and Kanakidou, M.: Change in global aerosol composition since preindustrial times, Atmos. Chem. Phys., 6, 5143–5162, 2006.

Turpin, B. J. and Lim, H.-J.: Species Contributions to PM2.5 Mass Concentrations: Revisiting Common Assumptions for Estimating Organic Mass, Aerosol Sci. Technol., 35, 602–610, doi: 10.1080/02786820119445, 2001.

Twomey, S.: Atmospheric Aerosols, Elsevier Scientific Pub., p. 320pp, 1977.

Wang, J., Lee, Y.-N., Daum, P. H., Jayne, J., and Alexander, M. L.: Effects of aerosol organics on cloud condensation nucleus (CCN) concentration and first indirect aerosol effect, Atmos. Chem. Phys., 8, 6325–6339, 2008.

Wang, X., Carmichael, G., Chen, D., Tang, Y., and Wang, T.: Impacts of different emission sources on air quality during March 2001 in the Pearl River Delta (PRD) region, Atmos. Environ., 39, 5227–5241, 2005.

Weast, R. C. and Astle, M. J.: CRC Handbook of Chemistry and Physics, 63rd, CRC Press Inc., Florida, 1982.

Wehner, B., Berghof, M., Cheng, Y. F., Achtert, P., Birmili, W., Nowak, A., Wiedensohler, A., Garland, R. M., Pöschl, U., Hu, M., and Zhu, T.: Mixing state of nonvolatile aerosol particle fractions and comparison with light absorption in the polluted Beijing region, J. Geophys. Res., 114, doi: 10.1029/2008JD010923, 2009.

Wendisch, M., Hellmuth, O., Ansmann, A., Heintzenberg, J., Engelmann, R., Althausen, D., Eichler, H., Müller, D., Hu, M., Zhang, Y., and Mao, J.: Radiative and dynamic effects of absorbing aerosol particles over the Pearl River Delta, China, Atmos. Environ., 42, 6405–6416, 2008.

Wex, H., Kiselev, A., Stratmann, F., Zoboki, J., and Brechtel, F.: Measured and modeled equilibrium sizes of NaCl and $(NH_4)_2SO_4$ particles at relative humidities up to 99.1 %, J. Geophys. Res., 110, doi:10.1029/2004JD005507, 2005.

Wex, H., Kiselev, A., Ziese, M., and Stratmann, F.: Calibration of LACIS as a CCN detector and its use in measuring activation and hygroscopic growth of atmospheric aerosol particles, Atmos. Chem. Phys., 6, 4519–4527, 2006.

Wex, H., Hennig, T., Salma, I., Ocskay, R., Kiselev, A., Henning, S., Massling, A., Wiedensohler, A., and Stratmann, F.: Hygroscopic growth and measured and modeled critical super-saturations of an atmospheric HULIS sample, J. Geophys. Res., 34, doi:10.1029/2006GL028260, 2007.

Wex, H., Stratmann, F., Hennig, T., Hartmann, S., Niedermeier, D., Nilsson, E., Ocskay, R., Rose, D., Salma, I., and Ziese, M.: Connecting hygroscopic growth at high humidities to cloud activation for different particle types, Environ. Res. Lett., 3, doi:10.1088/1748-9326/3/3/035004, 2008.

Wiedensohler, A.: An approximation of the bipolar charge distribution for particles in the submicron size range, J. Aerosol Sci., 19, 387–389, 1988.

Wiedensohler, A., Cheng, Y. F., Nowak, A., Wehner, B., Achtert, P., Berghof, M., Birmili, W., Wu, Z. J., Hu, M., Zhu, T., Takegawa, N., Kita, K., Kondo, Y., Lou, S. R., Hofzumahaus, A., Holland, F., Wahner, A., Gunthe, S. S., Rose, D., Su, H., and Pöschl, U.: Rapid aerosol particle growth and increase of cloud condensation nucleus activity by secondary aerosol formation and condensation: A case study for regional air pollution in northeastern China, J. Geophys. Res., 114, doi:10.1029/2008JD010884, 2009.

Willeke, K. and Baron, P. A.: Aerosol Measurement: Principles, Techniques, and Applications, John Wiley and Sons, Inc., New York, 2nd edn., 2001.

Xu, Q.: Abrupt change of the mid-summer climate in central east China by the influence of atmospheric pollution, Atmos. Environ., 35, 5029–5040, 2001.

Young, K. C. and Warren, A. J.: A reexamination of the derivation of the equilibrium supersaturation curve for soluble particles, J. Atmos. Sci., 49, 1138–1143, 1992.

Yum, S. S., Hudson, J. G., Song, K. Y., and Choi, B. C.: Springtime cloud condensation nuclei concentrations on the west coast of Korea, Geophys. Res. Lett., 32, L09 814, doi:10.1029/2005GL022 641, 2005.

Yum, S. S., Roberts, G., Kim, J. H., Song, K. Y., and Kim, D. Y.: Submicron aerosol size distributions and cloud condensation nuclei concentrations measured at Gosan, Korea, during the Atmospheric brown clouds East Asian Regional Experiment 2005, J. Geophys. Res., 112, D22S32, doi:10.1029/2006JD008 212, 2007.

Zhang, Q., Ma, X. C., Tie, X., Huang, M., and Zhao, C.: Vertical distributions of aerosols under different weather conditions: Analysis of in-situ aircraft measurements in Beijing, China, Atmos. Environ., 43, 5526–5535, doi:10.1016/j.atmosenv.2009.05.037, 2009.

Zhang, Y. H., Hu, M., Zhong, L. J., Wiedensohler, A., Liu, S. C., Andreae, M. O., Wang, W., and Fan, S. J.: Regional Integrated Experiments on Air Quality over Pearl River Delta 2004 (PRIDE-PRD2004): Overview, Atmos. Environ., 42, 6157–6173, doi:10.1016/j.atmosenv.2008.03.025, 2008.

Zhang, Y. L., Qin, B. Q., and Chen, W. M.: Analysis of 40 year records of solar radiation data in Shanghai, Nanjing and Hangzhou in Eastern China, Theo. Appl. Climat., 78, 217–227, 2004.

Zhao, C., Tie, X., and Lin, Y.: A possible positive feedback of reduction of precipitation and increase in aerosols over eastern central China, Geophys. Res. Lett., 33, L11 814, doi:10.1029/2006GL025 959, 2006.